UNIVERSIDADE DE LISBOA
FACULDADE DE CIÊNCIAS
DEPARTAMENTO DE FÍSICA

Compact object shadows and photon rings: a study of light intensity profiles for different accretion disk models

Luís Filipe Dias da Silva

Mestrado em Física
Especialização em Astrofísica e Cosmologia

Dissertação orientada por:
Dr. Francisco Sabélio Nobrega Lobo
Dr. Diego Rubiera-Garcia

2024

Acknowledgements

O trabalho desenvolvido nesta dissertação contou com o apoio de muitos, sem os quais a sua concretização não teria sido possível. Assim, gostaria de começar por expressar a mais profunda gratidão ao professor Francisco Lobo. Desde o apoio constante, à exploração de novas ideias, ao espírito motivacional, e entusiasmo incansáveis, é difícil resumir em tão pouco, o seu enorme contributo no meu percurso académico. Acima de tudo, obrigado por colocar sempre em primeiro lugar o bem-estar, saúde e felicidade. De igual modo agradeço ao Professor Diego Rubiera-Garcia, por me ter acolhido neste projeto tão fascinante, pelo seu encorajamento e conselhos inestimáveis, mas também priorizar o bem-estar e felicidade. É graças a vós que tive a minha primeira contribuição na área da Física, bem como as primeiras apresentações em contexto internacional. É graças a vós que tive uma experiência de tese excelente. Além dos meus orientadores, gostaria de estender os meus agradecimentos ao professor Gonzalo Olmo, colaborador do artigo científico no qual esta dissertação se baseou, por também me aceitar neste projeto.

De seguida, destaco aqueles cujas contribuições ajudaram à melhoria deste trabalho. Em particular, agradeço ao professor Manuel Rodrigues, ao professor Ednaldo Barros Junior, e aos colegas José Tarciso Junior e Henrique Vieira, por me terem convidado a fazer parte regular dos seus vários projetos, e com os quais tenho aprendido imenso sobre lentes gravitacionais, geometrias de espaço-tempo alternativas, entre outros. Agradeço ao professor Rui Agostinho, pelas várias dicas de programação em Mathematica que me levaram a explorar e aprender mais sobre esta poderosa ferramenta. Também estou grato ao colega de Mestrado Sandro Moreira, pelas conversas sobre programação, dados em listas, e memória de computadores, que levaram ao desenvolvimento de uma versão mais rápida do código de Mathematica (que humildemente apelidei de versão Ferrari). Igualmente, agradeço ao colega de Mestrado Gabriel Lourenço, pelas recomendações de literatura sobre expoentes de Lyapunov, ajudando-me a compreender melhor este conceito. Além destes, devo um grande agradecimento aos "Lobinhos", por diversas sugestões de melhoria do trabalho, apresentações, e pelas várias discussões estimulantes.

Relativamente ao meu percurso académico, gostaria de agradecer aos professores Nelson Nunes e o Pedro Machado, da FCUL, e ao professor Nelson Ramalho, o meu orientador de tese em Psicologia, no ISCTE, cuja postura é inspiradora pelo seu positivismo, serenidade e humanidade. Agradeço também aos vários colegas de faculdade que me honraram com a vossa presença, debates filosóficos e excelente disposição, com particular destaque para os membros dos "NIF" e do grupo a "Quinta".

Em nota mais pessoal, agradeço à minha mãe e ao meu pai, pelo vosso apoio incondicional e incentivo, pelos valores que me incutiram, e por todos os sacrifícios que fizeram por mim. Também expresso a minha gratidão à Eleonore Lefebure, por todo o seu apoio, compaixão e bondade desde que nos conhecemos. Ao meu melhor amigo, André Lino, que é como um irmão, envio um grande abraço e um obrigado por quase 30 anos de amizade. Por último, agradeço à Daniela Cordeiro, a minha namorada. Obrigado por aturares todas as noites a trabalhar até tarde e seres a minha parceira em Física. Mas, acima de tudo, obrigado por percorreres este percurso comigo, pelo teu companheirismo, ternura e a tua inspiração.

Resumo

Um buraco negro, quando iluminado por um disco de acreção, destaca-se pela sua deslumbrante aparência visual, composta por anéis de luz brilhantes em torno de uma silhueta escura. Tais fenómenos são causados pela deflexão de raios luminosos que atravessam a intensa curvatura do espaço-tempo na vizinhança destes corpos maciços. As imagens captadas recentemente pela colaboração *Event Horizon Telescope* (EHT), dos objetos supermaciços localizados no coração da galáxia M87 e da Via-Láctea (i.e. Sagitário A*), marcam o primeiro passo para estudar os fenómenos observacionais supracitados. Neste âmbito, um estudo realizado por Vagnozzi et al. restringiu o espaço de parâmetros de várias geometrias do espaço-tempo esfericamente simétricas, comparando o raio da sombra previsto pelas mesmas com o raio da sombra estimado para Sagitário A*. Contudo, uma vez que a sombra não é uma previsão genérica da teoria de Relatividade Geral, a abordagem anterior não permite destacar geometrias específicas para representar as observações realizadas, mas apenas avaliar a compatibilidade com as mesmas. Além deste aspeto, a inferência da sombra realizada pelo EHT encontra-se sujeita a uma série de pressupostos sobre as propriedades do disco de acreção. Em contraste, o anel de fotões é uma previsão genérica da teoria de Relatividade Geral, cuja dependência das propriedades de acreção decresce exponencialmente em função do número de meias órbitas das trajetórias de luz em torno de um buraco negro. Embora a sua emissão se sobreponha à emissão direta do disco de acreção, espera-se que futuras observações isolem o sinal interferométrico dos anéis de primeira e segunda ordem. Motivados por estes aspetos, o trabalho desenvolvido nesta dissertação combina os dois ingredientes acima, a sombra e o anel de fotões, para gerar as imagens de um conjunto de geometrias esfericamente simétricas iluminadas por um disco de acreção fino. Com esta abordagem estuda-se o primeiro e segundo anéis através de expoentes de Lyapunov de orbitas instáveis e a sua correlação com a extinção de luminosidade entre os mesmos, explorando assim a possibilidade de utilizar estes anéis como discriminadores observacionais de geometrias de buracos negros alternativas.

O primeiro capítulo inicia com o contexto histórico e teórico referente à noção de buraco negro e o estudo da sua aparência visual. Em particular, é feita uma revisão histórica que compreende a origem das ideias de deflexão de luz por um corpo maciço até ao desenvolvimento da teoria moderna de buracos negros, sob a alça da teoria de relatividade geral. Posteriormente, explora-se brevemente a investigação da aparência visual de um buraco negro, estudando os fenómenos visuais causados pela deflexão extrema das trajetórias de luz e a evolução deste domínio, desde as simulações às observações realizadas pelo EHT. Neste ponto, identifica-se os dois aspetos mais salientes das imagens de buracos negros: a sombra e o anel de fotões. Em seguida, descreve-se a motivação para o trabalho desenvolvido, enfatizando o papel destas assinaturas observacionais como testes da hipótese de Kerr e da Relatividade Geral, destacando atuais questões em aberto, e apresentando o objetivo principal deste trabalho.

No segundo capítulo exploram-se os fundamentos teóricos relacionados com as trajetórias de luz num espaço-tempo curvo. Especificamente, são discutidos os seguintes tópicos: 1) Geodésicas nulas em espaços-tempos esfericamente simétricos; 2) Geodésicas nulas efetivas em espaços-tempos esferica-

mente simétricos provenientes de teorias de eletrodinâmica não-linear; 3) Fotosferas e a curva crítica; 4) Sombra de um buraco negro; 5) Anel de fotões. Em relação ao primeiro ponto, apresenta-se a derivação da equação diferencial de movimento ao longo de uma geodésica nula, partindo do Lagrangiano de um espaço-tempo genérico. Esta equação é fundamental para a produção de imagens de buracos negros e outros objetos compactos com simetria esférica. O segundo ponto generaliza a abordagem anterior para soluções esfericamente simétricas das equações de campo de Einstein acopladas a Lagrangianos derivados de teorias de eletrodinâmica não-linear, estudado para o caso particular de configurações puramente magnéticas. Em tais circunstâncias os fotões movimentam-se ao longo de geodésicas circunscritas numa geometria do espaço-tempo efetiva, que surge em função de correções não-lineares à teoria eletrodinâmica de Maxwell. Posteriormente, abordam-se os conceitos de fotosfera e de curva crítica. Tais conceitos estabelecem a relação entre orbitas circulares instáveis de luz e o seu parâmetro de impacto (teórico) no plano de imagem do observador, e estão profundamente relacionados com a sombra do buraco negro e o anel de fotões. Relativamente à sombra de um buraco negro, discute-se a sua definição, propriedades, e o seu papel enquanto observável. Demonstra-se a relação entre o raio da sombra de um espaço-tempo genérico esfericamente simétrico e a curva crítica. Também se debate o conceito de depressão central de brilho e sua relação com a sombra, onde se conclui que estes coincidem apenas em condições de acreção esférica em torno de um buraco negro. Posteriormente, discutem-se as observações da sombra de Sagitário A*, realizadas pela colaboração EHT. Destaca-se a inferência do raio da sombra e os valores estimados para as dimensões da mesma. Por último, estuda-se o anel de fotões. Em particular, apresenta-se a categorização de trajetórias de luz em função do número de meias órbitas em torno de um corpo ultracompacto. De seguida, discutem-se as propriedades do anel de fotões, com foco na sua crescente dependência da geometria do espaço-tempo e independência das condições de acreção. Conclui-se o capítulo com a relação entre os expoentes de Lyapunov - um tipo de medida de instabilidade de órbitas - e a razão do fluxo luminoso entre dois anéis sucessivos.

No terceiro capítulo expõe-se a metodologia do trabalho realizado, correspondente à produção de imagens de geometrias esfericamente simétricas, e do estudo do primeiro e segundo anéis. Em primeiro lugar, apresentam-se os modelos semianalíticos que simulam o perfil de emissão da acreção em torno de um buraco negro. Tais modelos descrevem um disco de acreção axissimétrico e geometricamente fino, cuja emissão assume-se opticamente fina. Embora estes modelos consistam em aproximações simplificadas do ambiente extremamente dinâmico e energético de um disco de acreção, os seus perfis de emissão reproduzem assinaturas observacionais congruentes com as características mais proeminentes em simulações de discos de acreção relativísticas, com processos magneto-hidrodinâmicos. De seguida, descreve-se o processo de *ray-tracing* utilizado na geração de imagens de objetos ultracompactos. Neste ponto detalha-se a computação de geodésicas nulas, desde o plano de imagem do observador para o passado, de onde estas provêm, e o cálculo do expoente de Lyapunov associado ao primeiro e segundo anéis. Posteriormente, calcula-se o perfil de intensidade recebida no referencial do observador, integrando a equação de transferência radiativa ao longo das geodésicas nulas. Demonstra-se que, nas condições previamente estabelecidas, a intensidade observada é proporcional ao número de meias orbitas completas por uma trajetória de luz. A secção seguinte aborda as geometrias esfericamente simétricas selecionadas do estudo de Vagnozzi et al. Cada geometria é brevemente descrita, sendo apresentada a sua forma funcional. Em cada caso, restringe-se o espaço de parâmetros em função da compatibilidade do respetivo raio da sombra (de cada geometria) com o raio da sombra estimado pelo EHT. Constata-se que a maioria das geometrias satura o limite inferior da sombra, à exceção de duas que saturam o limite superior, e outras cujo tamanho da sombra não permite tal restrição.

No quarto capítulo, são apresentados e discutidos os resultados da aplicação da metodologia anterior, visando gerar imagens das geometrias alternativas consideradas e estudar os anéis de primeira e segunda ordem das mesmas. As imagens de cada geometria são geradas à luz de três perfis de acreção distintos. Primeiramente, analisa-se o caso da geometria de Schwarzschild. Verifica-se que o anel de fotões é uma assinatura observacional persistente, presente em todos os modelos. Constata-se que as variações entre modelos introduzem diferenças significativas na emissão direta, mas a emissão correspondente ao primeiro, e em particular ao segundo anel de fotões, é independente da escolha de perfil de emissão. Subsequentemente, são apresentados os dados referentes a algumas propriedades físicas das geometrias alternativas e à extinção de luminosidade observada entre o primeiro e segundo anéis, organizando as geometrias em ordem decrescente do seu expoente de Lyapunov. Verifica-se que não existem correlações significativas entre as propriedades físicas das geometrias e o expoente de Lyapunov teórico. Por outro lado, a extinção de luminosidade entre o primeiro e segundo anéis correlaciona-se significativamente com a previsão teórica mediada por este índice. Fixando um modelo de emissão, a extinção de luminosidade entre os anéis de primeira e segunda ordem permite distinguir entre as geometrias alternativas consideradas, mesmo quando estas possuem uma dimensão da sombra idêntica. Deste modo, o expoente de Lyapunov demonstra ser um bom indicador da geometria do espaço-tempo. Note-se que em todos os casos, existe um desvio entre a extinção de luminosidade estimada e a observada, que é menor para os modelos de acreção cuja emissão se estende até ao horizonte de eventos. Perante os resultados, conclui-se que embora os anéis de primeira e segunda ordem revelem informação útil sobre a geometria do espaço-tempo, ainda são necessários mais esforços testando modelos de acreção mais representativos e mais configurações de geometrias do espaço-tempo, para que estes se tornem testes fiáveis de relatividade geral e do regime de gravidade forte.

Palavras-chave: Buracos Negros, Sombras de Buracos Negros, Anéis de Fotões, Expoentes de Lyapunov

Abstract

A black hole surrounded by an optically thin accretion disk exhibits a distinctive visual appearance, characterized by a bright radiation ring surrounding a central brightness depression. The imaging by the Event Horizon Telescope (EHT) of the supermassive objects at the heart of the M87 and Milky Way (Sgr A*) galaxies, marked the first step into peering towards these features. Recently, Vagnozzi et al. constrained the parameter space of several spherically symmetric geometries by comparing their predicted shadow radius with the estimated radius of Sgr A*'s shadow. Using this result, we study some features of the first and second photon rings from a restricted pool of such geometries in thin accretion disk settings. The latter are described by calling upon three semi-analytic emission profiles introduced by Gralla, Lupsasca and Marrone. We characterize the first and second rings via Lyapunov exponents of unstable bound orbits and discuss its correlation with the luminosity extinction ratio between them. Our results reveal that, at a fixed emission profile, there are significant deviations in the visual appearance of the photon ring among different geometries. Additionally, the observed luminosity extinction ratio strongly correlates with the theoretical extinction ratio predicted by the Lyapunov exponent, with a small estimation error. We conclude by elaborating on the chances of using such photon rings as observational discriminators of alternative black hole geometries using very long baseline interferometry.

Keywords: Black Holes, Black Hole Shadows, Photon Ring, Lyapunov Exponent

Index

List of Figures

List of Tables

Preface

The official research presented in this document was conducted at the Instituto de Astrofísica e Ciências do Espacço (IA) and the Departamento de Física of Faculdade de Ciências da Universidade de Lisboa, with support from the research grants UIDB/04434/2020 and UIDP/04434/2020. The research was supervised by Professor Francisco S.N. Lobo, from the Instituto de Astrofísica e Ciências do Espaço (IA) and the Departamento de Física of Faculdade de Ciências da Universidade de Lisboa (FCUL), and co-supervised by Professor Diego Rubiera-Garcia, from the Instituto de Física de Partículas y del Cosmos (IPARCOS) and the Departamento de Física Teórica of Universidad Complutense de Madrid (UCM).

Part of the work included in this dissertation was published in Physical Review D under the title "Photon rings as tests for alternative spherically symmetric geometries with thin accretion disks" [1], done in collaboration with Professor Francisco S.N. Lobo, Professor Diego Rubiera-Garcia, and Professor Gonzalo J. Olmo, from the Instituto de Física Corpuscular (IFIC) and the Departamento de Física Teórica of Centro Mixto Universidad de Valencia (CSIC), as well as the Departamento de Física of the Universidade Federal do Ceará (UFC). In addition, the material in [1] was presented at national and international conferences in talk format, including:

- Luís F. Dias da Silva, "Photon rings as tests for alternative spherically symmetric geometries with thin accretion disks", Spanish and Portuguese Relativity Meeting (EREP 2023), 17^{th} of July, 2022, Bizkaia Aretoa, Universidad del País Vasco/Euskal Herriko Unibertsitatea, Bilbao, Spain;
- Luís F. Dias da Silva, "Photon rings as tests for alternative spherically symmetric geometries with thin accretion disks", XVI Black Holes Workshop, 20^{th} of December, 2023, Faculdade de Engenharia da Universidade do Porto, Porto, Portugal.

The following articles were produced during the course of my Master's dissertation; however, their content is not included here, as they are not related with the main topic developed in this work:

- E. L. Junior, J. T. S. Junior, F. S. Lobo, M. E. Rodrigues, L. F. D. da Silva, and H. A. Vieira, "Observations on the massive particle surface method", arXiv preprint arXiv:2401.01821, 2024 [2];
- E. L. Junior, J. T. S. Junior, F. S. Lobo, M. E. Rodrigues, D. Rubiera-Garcia, L. F. D. da Silva, and H. A. Vieira, "Gravitational lensing of a Schwarzschild-like black hole in Kalb-Ramond gravity", arXiv preprint arXiv:2405.03284, 2024 [3];
- E. L. Junior, J. T. S. Junior, F. S. Lobo, M. E. Rodrigues, D. Rubiera-Garcia, L. F. D. da Silva, and H. A. Vieira, "Spontaneous Lorentz symmetry-breaking constraints in Kalb-Ramond gravity", arXiv preprint arXiv:2405.03291, 2024 [4].

Chapter 1

Introduction

In this chapter, we review the context and motivation of the present work. The initial section explores the historical elements that culminated in the prediction of black holes. Afterwards, we discuss the study of their appearance, focusing on the main features of their optical appearance when illuminated by an accretion disk. This is followed by the motivation of the present research, where we briefly describe our approach on the use of photon rings as tests of the underlying space-time geometry. Lastly, we provide a structured outline of this dissertation.

1.1 A brief historical overview

1.1.1 From Dark Stars to Black holes

In the vast cosmic tapestry of the Universe, few enigmas are as captivating and perplexing as Black Holes - incredibly dense regions in the fabric of space-time in which the gravitational pull is so strong that not even light can escape from their grasp [5]. The notion that gravity influences the behaviour of light predates Einstein's General Theory of Relativity (GR) [6]. Its origin can be attributed to Sir Isaac Newton, who first hinted at it in his work Opticks, published in 1704: "Do not Bodies act upon Light at a distance, and by their action bend its Rays; and is not this action (*caeteris paribus*) strongest at the least distance?". Still, Newton never provided a formal discussion on this subject, leaving it instead for future generations.

By the late 18^{th} century, this problem was carried further by Reverend John Michell; a polymath whose contributions extended over numerous scientific fields [7]. Michell stands out for having introduced the concept of *dark stars* when he suggested that a sufficiently massive star would prevent any light emitted by it to escape its gravitational attraction, thus appearing invisible to a distant observer. Michell even argued that the presence of such objects could be inferred by observing the motions of any luminous bodies orbiting around them. These ideas bore a striking resemblance with black holes. Unlike their modern counterparts, however, dark stars were not limited to being extremely compact objects. They possessed a different structure and formation process, and the mechanism that causing them to be dark was very distinct from the modern relativistic view of black holes [8]. A few years later, Pierre-Simon Laplace also proposed the existence of Dark Stars, independently from Michell [7]. It was around this period, that the first works concerning the deflection of light passing near a massive object were developed, notably by H. Cavendish (1784), W. Herschel (1791), and J. Soldner (1801) [6, 9]. Although these works were framed within the context of Newtonian gravitation and the corpuscular theory of light, they foreshadowed the interplay between light and gravity.

1.1 A brief historical overview

The transition from Dark Stars to Black Holes reflects the evolution of our understanding of gravity. In this regard, there were several crucial advances in the fields of Physics and Mathematics, that took place throughout the 19^{th} century and also in the early 20^{th} century. On one hand, the corpuscular theory of light was abandoned in favour of the wave theory, and later developments in quantum theory, due to their ability to explain a broader range of optical phenomena and compatibility with experimental observations. As a consequence, the concept of Dark Stars fell into obscurity. This was also a period when the cracks in Newton's Theory of gravitation started to show, as astronomers struggled to connect its theoretical predictions with the observed excess precession of the perihelion of Mercury's orbit. On the other hand, the emergence of non-Euclidean interpretations in geometry shook the foundations of mathematics, by challenging more than 2000 years of Euclidean tradition with the introduction of concepts such as spatial curvature, and generalizing the application of geometry to higher dimensions. In a similar spirit, Albert Einstein's Special Theory of Relativity reshaped our understanding of the fundamental nature of the Universe, challenging the longstanding notion of absolute time and space, and predicting phenomena such as time dilation, length contraction, and the mass-energy equivalence. The stage was set for a revolution in the world of physics.

In 1915, Einstein presented a generalization of his own Special Relativity to non-inertial (i.e accelerating) reference frames: the General Theory of Relativity (GR) [10]. This theory completely revolutionised our understanding of gravity and replaced Newton's gravitation theory, where gravity is a fundamental force of nature, with an elegant geometric interpretation, where gravity arises as a consequence of the curvature of the (four-dimensional) space-time continuum, that is induced by the presence of mass and energy. Shortly after GR's inception, Karl Schwarzschild found the first exact solution of the Einstein field equations, which described a neutral, static and spherically symmetric vacuum [11]. Despite predicting the existence of black holes, it would take a few more decades of theoretical advances (e.g. [12–16]) in the fields of quantum physics, astrophysics, and atomic theory, before the Schwarzschild solution would be interpreted as such [8]. Furthermore, the discovery of highly energetic compact objects (i.e. quasars and compact X-ray sources) [17] helped further cement the idea and, by the mid-1960's, black holes had been acknowledged by the scientific community. In the ensuing years, the research into the theory of modern gravitational collapse, singularities, and other properties of black holes, flourished [5], leading to the emergence of the black hole physics discipline.

Before moving towards the appearance of black holes, we make a small digression to very briefly describe what a black hole is. Rather than being thought of as an object, a *black hole* (BH) is a region in space-time. It is the region of "no-escape" that is formed when a massive body shrinks below the gravitational radius, for which the corresponding escape velocity is that of the speed of light [5, 17]. The boundary of this region is known as the event horizon, representing the causal non-physical boundary beyond which an event cannot connect with an observer outside the BH (i.e. an external observer cannot see past the event horizon) [8]. At the centre of a BH lies a physical singularity, which is a particular region where the space-time curvature becomes infinite and the laws of GR break down (i.e. where the world lines of particles and light rays end) [18]. Since nothing can travel faster than the speed of light, any physical body or signal that enters that crosses the event horizon becomes disconnected from the Universe, unable to escape the BH and will plunge inevitably towards the singularity, where it is destroyed [5]. Consequently, black holes can be considered the ultimate, perfect absorbers. The absence of any type of electromagnetic or gravitational wave emission renders them impossible to detect directly. However, by virtue of their immensely powerful gravitational field, it is possible to infer the presence of a BH by looking for evidence of the gravitational influence it exerts on its environment.

1.1.2 The Optical Appearance of a Black Hole: Unveiling the Unseen

The earliest attempts at understanding the motion of light near a massive body can be traced back to the works of Hilbert (1917) [19], Hagihara (1931) [20], and Darwin (1959) [21]. Hilbert studied null geodesics in the Schwarzschild space-time and found the radius of circular orbits of light along with the corresponding impact parameter. Almost 15 years later, Hagihara performed an in-depth analysis of geodesic motion in the Schwarzschild space-time, resorting to Weierstrass elliptic functions to obtain the first exact analytic solutions of geodesic motion. Hilbert's results were re-visited and expanded upon by Darwin, in 1959, while examining the motion of particles within the gravitational field of a heavy particle. Still, neither of these works were focused on black holes *per se*, due to the fact that the Schwarzschild solution had yet to be interpreted as such.

In the 1960's, when the concept of BH gained widespread recognition, astrophysicists began to ponder about the appearance of these cosmic entities. This subject was first discussed by Bardeen (1973) [22], who analysed the gravitational lensing properties of neutral rotating black holes (i.e. Kerr Black Holes [23, 24]) by looking into timelike and null geodesics in the Kerr geometry. The author found that the apparent "shape" of a fast spinning BH had an asymmetric D-shaped outline, when observed edge-on (i.e. at a 90° angle between the observer's line-of sight and the BH's angular momentum axis) and illuminated by a background light source of an angular size larger than itself. In the same year, Cunningham and Bardeen [25] studied and traced the apparent position of a star orbiting the equatorial plane of an extreme Kerr BH. By computing the position of the brightest image of a point-like source, as a function of time, their work revealed the existence of a primary "direct" image track accompanied by a secondary "lensed" image track. By the year 1978, this effort was taken further by Palmer et al. [26] and Luminet [27], who independently pioneered the first visual representations of light bending near a Schwarzschild BH [28, 29]. The former simulated the effects of gravitational lensing from a Schwarzschild BH on a background star field, from the point-of-view of a camera orbiting the BH[1]. The latter modelled the appearance of a Schwarzschild BH surrounded by a rotating, geometrically thin accretion disk [27]. The resulting image, which is depicted in Figure 1.1, unveils a bright thin disk structure, complemented with distorted images of the disk region located behind the BH, and a central dark area containing a fine ring of light. In addition, it is also possible to observe an asymmetric brightness in the disk emission which is the Doppler effect caused by the accretion disk rotation. Remarkably, the image was completely hand drawn from numerical data modeled on a punch card computer.

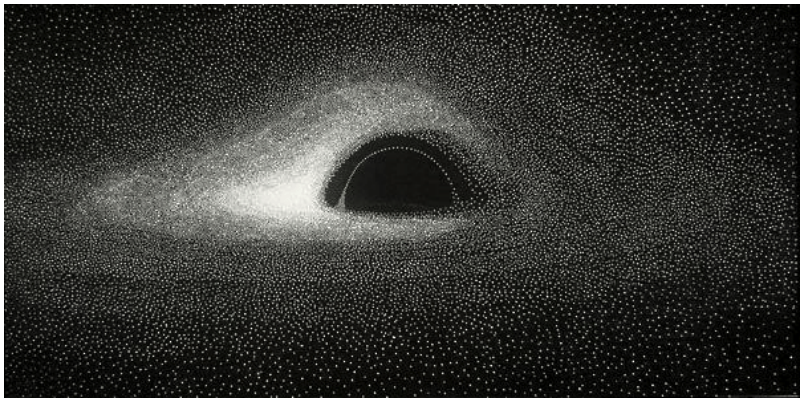

Figure 1.1: Visual representation of the image of a Schwarzschild BH surrounded by a rotating, geometrically thin accretion disk, seen by a distant observer [27].

[1]The reader is referred to the video in [30], which simulates a similar film clip.

1.1 A brief historical overview

Despite these seminal efforts, the progress in the field of imaging black holes remained slow until the possibility of observing them via Very Long Baseline Interferometry (VLBI) was first discussed in the literature [29]. Motivated by the growing evidence of an ultracompact dark mass associated with the radio source Sagittarius A* (Sgr A*), at the heart of the Milky Way galaxy, the work of Falcke, Melia & Agol (1999) [31] launched the prospects of imaging the "shadow" of Sgr A* with VLBI radio-astronomy. This represented a turning point in the history of BH imaging [29], as it propelled the research in this field and culminated in the observational efforts led by the Event Horizon Telescope (EHT) collaboration [32, 33]. The optical appearance of black holes has since been scrutinized in numerous accretion scenarios (e.g. [34–40]), leading authors on a quest to study the extreme light bending properties of black holes and the resulting unique observational features hinted by the work of Bardeen, Palmer et al., and Luminet (e.g. [41–53]). This has also prompted astrophysicists to go beyond the Kerr (and Schwarzschild) black holes, to examine the appearance of alternate space-time geometries including many different black hole space-times (e.g.[54–58]), as well as naked singularities (e.g. [59–61]), wormholes (e.g.[62–64]), and other exotic compact objects (e.g.[65–69]), exposing their observational signatures, and the similarities (or differences) between them. As for the EHT observations, the progress in VLBI development yielded the first images of the supermassive objects at the heart of the M87 [32] and Milky Way [33] galaxies (as seen in Figure 1.2), in one of the most remarkable achievements in observational astrophysics.

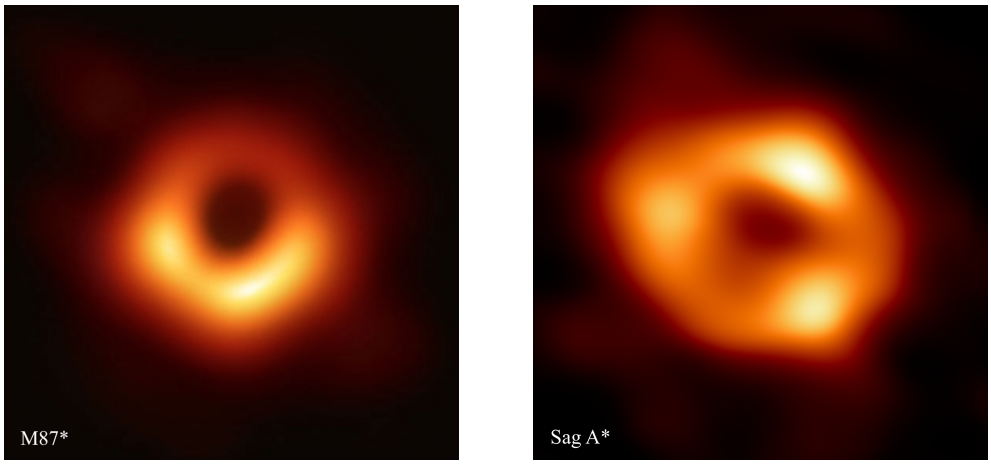

Figure 1.2: Images of the supermassive objects M87* [32] and Sgr A* [33] captured by the EHT collaboration.

These observations reveal the presence of a bright radiation ring enclosing a central brightness depression. These are consistent with the most salient features of images obtained via General Relativistic Magneto-Hydrodynamic (GRMHD) simulations of the accretion flow surrounding a Kerr black hole. While the next chapter expands on these features, we provide a synopsis in the following text. The first such feature comes from the presence of a region of bound unstable light orbits, allowing for strongly lensed trajectories that are able to orbit around a black hole [70]. For a Kerr BH surrounded by an optically thin accretion flow (i.e. transparent to its own radiation), such trajectories create a thin "photon ring", on top of the direct emission, whose features depend on the geometry of the accretion flow [71]: spherical infalling accretion flows cause the photon ring to converge to a theoretical curve in the image plane of the observer, while the central brightness depression entirely fills it (i.e. the shadow defined according to Falcke et al. [31]) ; geometrically thin accretion disks cause the photon ring to be decomposed into an infinite sequence of discrete subrings, while the size of the central brightness depression depends on the accretion disk's inner radius. In this regard, it is worth noting that GRMHD simulations tend to favour models of non-spherical accretion, supporting the latter instead [71].

1.2 Motivation

One of the core results of the theory of black holes within General Relativity (GR) is the universality of the Kerr hypothesis [23], which states that every BH in the Universe can be characterized by the Kerr solution and its two parameters: mass and angular momentum. This hypothesis rests firmly in uniqueness (i.e. no-hair) theorems [72–75], though the addition of matter fields allows "hairy" black holes to exist under certain circumstances [76, 77]. Since testing the validity of the Kerr hypothesis is extremely difficult (see however [78]), one typically performs instead null-tests (i.e. tests with electromagnetic or gravitational waves) on the compatibility of the Kerr BH and its alternatives with current observations [79]. Though the EHT observations marked an important first step towards peering at the ultracompact masses M87* and Sgr A*, the nature of such objects is still an open question, as several non-Kerr models remain compatible with the current observations [80, 81]. Nonetheless, these observations yield relevant clues into horizon scale visual phenomena that are crucial towards testing the black hole paradigm. With the advent of the EHT observations, the field of imaging compact objects illuminated by their accretion disk is entering a golden era, in which it represents a promising opportunity to both test the reliability of the Kerr solution and to explore the plausibility of any of its alternatives to describe observed images. Such an opportunity, however, can be undermined by the large uncertainties in the accretion disk modelling, together with its entanglement with the background geometry in the generation of these images, which renders the quest for reliable observational discriminators (of the underlying space-time geometry) an object of interest in the scientific community. This can be pursued via the aforementioned features - photon ring and the central brightness depression - since these carry a wealth of information on the underlying geometry [34, 82–84].

While the precise size of the outer edge of the central brightness depression cannot be directly determined by the EHT Collaboration (i.e. since it cannot measure luminosity contrasts below $\sim 10\%$ of the peak intensity), it has been recently reported that it can be inferred indirectly via a correlation between the observed diameter of the bright emission ring and the shadow's size itself, provided the theoretical and observational biases are accounted for [80]. Assuming the validity of this correlation and the assumptions upon which it holds, a collective effort was conducted by Vagnozzi et. al. (hereafter Vea) [81] to constrain the parameter space of a plethora of alternative spherically symmetric geometries, by assessing the compatibility of their theoretical shadow radius with the shadow radius of Sgr A*. The authors reported multiple spherically symmetric geometries to be compatible with the current estimates of Sgr A*'s shadow size, where for some models this also represented the first-ever parameter space constraints. While the shadow is known to be degenerate between different space-time geometries (and therefore the current observations cannot single out specific metrics to represent the current images), the gravitational lensing properties are a generic prediction of GR [85]. Notably, the theoretical properties of (higher-order) subrings have been shown to grow less dependent on the astrophysical properties of the disk and more on the background geometry, thus offering us a way out of the "contamination" enacted by the disk [51, 70, 82, 86]. Moreover, despite their exponentially-suppressed luminosity [27, 47], their sharp features die off slowly in the Fourier domain, producing strong interferometric signatures on longer baselines that are expected to be achievable with future VLBI projects [48, 70, 71, 82]. Given the fact that one expects significant deviations in the shape, diameter, width, and relative luminosity of the photon (sub)rings for alternative (non-Kerr) geometries, precise observations of the photon ring could be potentially used to constrain them [51].

The main objective of this work is to combine the two previously discussed ingredients and assess the usefulness of the photon ring as an observational discriminator of alternative black hole geometries.

To achieve this, we take a restricted pool of the alternative spherically symmetric geometries considered by Vea, and generate their images (when pushed to the limit of their parameter space constraints) illuminated by an equatorial orbital infinitesimally-thin accretion disk, at a face-on orientation (i.e. 0° angle between the observer's line-of sight and the BH's angular momentum axis). In doing so, we neglect the contribution of spin and benchmark any results against the Schwarzschild geometry. This is done for a few reasons. First, the generation of black hole images is significantly simpler in spherically symmetric space-times, comparatively to axially symmetric space-times (i.e. rotating black holes) where, for example, one has to take into account non-equatorial light rays [87]. In addition, recent estimates on the spin of Sgr A* seem to support a low spin regime, though it is worth noting that presently there is no consensus on the spin and inclination angle of Sgr A* [81]. While it is true that rotating space-times are more consistent with a realistic astrophysical scenario, at low inclination angles the contribution of spin towards the size and shape of the shadow remains small, even for fast spinning black holes [88]. Regarding the accretion disk, the assumption of an infinitesimally thin geometry is motivated in order to enhance the opportunity to clearly visualize the photon rings. To model its emission, we employ the semi-analytic accretion profiles introduced by Gralla, Lupsasca and Marrone (hereafter GLM models) in [82]. While these models are manifestly simpler than the more realistic representations achieved with GRMHD simulations, they have the advantage of being able to mimic the latter's most prominent features with significantly less computational power [82, 89]. We then proceed to study the photon ring structure in each alternative geometry by computing the Lyapunov exponent of nearly-bound orbits - a measure of the instability scale between bound orbits that is sensitive to deviations from Kerr-ness and that predicts the relative luminosities between two subrings [70, 90, 91]. To what extent the actual luminosity suppression deviates from the theoretical Lyapunov prediction, for different choices of accretion profile, is a question of great interest in connecting theoretical properties with actual observables, and something that has not yet been explored. Thus, from the generated images, we shall seek the presence of any correlation between the observed relative intensities and the theoretically predicted ones, restricting our analysis to subrings that offer a reasonable enough compromise between having a sufficient independence from the astrophysical properties of the emission and being prospective VLBI targets.

1.3 Outline

This dissertation is organized as follows. Chapter 2 concerns the theoretical framework of this work. In this regard, the null geodesic equation of motion is derived in a static and spherically symmetric space-time, and this formalism is extended to the null geodesic motion in (magnetically charged) space-times threaded by non-linear corrections to Maxwell's electrodynamics. The discussion proceeds to the concepts of photon spheres and the critical curve, followed by the shadow and photon ring heuristics. The latter two are particularly important, as the majority of this work (and most of the current literature) is dominated by the "shadow" and "photon ring" terminology, which have been defined and/or interpreted in various ways. In chapter 3, the methodological approach is described in detail. Here, the discussion is centered around the image generation procedure and ingredients, including the accretion disk simulation with semi-analytic models, the null geodesic ray-tracing, and the alternative geometries that are tested. The discussion of the obtained physical results and generated images are provided in chapter 4. Here, the Schwarzschild black hole is considered first, setting the benchmark for the main results, which are discussed in light of the aforementioned semi-analytic models. Chapter 5, concludes this work with further thoughts and prospects, exposing the main findings of our work and elaborating on some of the limitations in our approach, as well as potential future research opportunities.

Chapter 2

Theoretical Framework

In this chapter, we delve into the theoretical underpinnings of light propagation in the framework of General Relativity, reviewing the concepts that are essential to the characterization of black hole images in a top-down approach. Our discussion starts with the trajectories of massless particles in a curved space-time, which occur along curved paths designated as null geodesics. The derivation of the null geodesic motion equation under a spherically symmetric space-time is presented. We follow this by upgrading the null geodesic formalism to incorporate the cases in which the matter source is a magnetic monopole originating in models with non-linear electrodynamics. In the third section, the focus is on bound photon orbits, the notion of photon sphere and the critical curve. This is followed by an overview of the concept of black hole shadow. We also elaborate on the EHT calibrated measurement of the size of the shadow of Sgr A*. This chapter ends with a section devoted to the concept of photon ring, its role as an observational discriminator, and its relation with Lyapunov exponents.

2.1 Null geodesics in Static and Spherically Symmetric space-times

In GR, where gravity is described in terms of the space-time curvature around massive objects, the concept of geodesic is vital to understanding particle motion. Essentially, it generalizes the concept of straight line in non-Euclidean (i.e. curved) spaces: a geodesic corresponds to the curve that minimizes the length between two points in a curved space of n-dimensions, similarly to how a straight line minimizes the length between two points in any flat space [92]. In the context of GR and modified gravity theories, a geodesic describes the trajectory of a free falling particle within a curved space-time geometry (i.e. unaffected by external forces) [93]. Null geodesics are a particular class of geodesics belonging to massless particles. These are the geodesics that are used to study the trajectories of light (photons) in space-time, according to the principles of GR. Thus, they play a crucial role in understanding the appearance of a black hole to a distant observer. In what follows, we derive the equation of motion of photons in a generic spherically symmetric space-time (SSS) driving the generation of BH images in our work. We shall refrain from discussing the mathematical formalism in full depth, as it does not suit the purpose of this dissertation. There are several works that explore the formalism in excellent detail, to which the reader is referred to (e.g. [92–95]). The prescription we present is inspired by the work of Misner, Thorne and Wheeler (1973) [93], Chandrasekhar (1998) [94], as well as the recent review by Perlick (2022) [87]. With the purpose of simplifying our calculations and formulae, we adopt a geometrodynamic unit system [96] throughout this work, setting the speed of light c and the gravitational constant G to $c = G = 1$. A consequence of this approach is that the physical quantities related with mass will have a dimension of length instead.

2.1.1 The Lagrangian of a static SSS

The motion of photons travelling along null geodesics may be determined analytically for static and spherically symmetric space-times, such as the Schwarzschild space-time. These may be deduced from a Lagrangian

$$\mathcal{L}(x,\dot{x}) = \frac{1}{2} g_{\mu\nu}\dot{x}^{\mu}\dot{x}^{\nu}, \tag{2.1}$$

that admits a space-time with a line element of the form

$$ds^2 = g_{\mu\nu}dx^{\mu}dx^{\nu}. \tag{2.2}$$

Here, $\dot{x}^{\mu} = dx^{\mu}/d\lambda$ denotes the components of the four-velocity[1], $g_{\mu\nu}$ is a metric tensor which encodes the space-time curvature, ds^2 corresponds to an invariant quantity that is the square of an infinitesimal length interval - the line element ds, and dx^{μ} indicates an infinitesimal four-coordinate displacement. We shall take advantage of the previous definitions and its connection with the Euler-Lagrange (E-L) equations to derive the equation of motion of photons along null geodesics. Given the symmetry of the problem, the generic line element is conveniently expressed in a spherical space-time coordinate system, such that the components of a position four-vector $x^{\mu} = (x^0, x^1, x^2, x^3)$ are the time (t), radial (r), polar (θ) and azimuthal (ϕ) coordinates, respectively. Thus, we begin our considerations from a generic static and spherically symmetric line element

$$ds^2 = -A(r)dt^2 + B(r)dr^2 + C(r)d\Omega^2, \tag{2.3}$$

with $A(r)$, $B(r)$ and $C(r)$ corresponding to the generic functions that describe the underlying space-time, and $d\Omega^2 = d\theta^2 + \sin^2\theta d\phi^2$ representing here the infinitesimal area of a unit two-sphere (i.e. the surface of a three dimensional sphere). The generic functions depend explicitly on the radial coordinate as any dependence on the polar and azimuthal coordinates would be incompatible with the spherical symmetry. Furthermore, there is no dependence on the time coordinate as the system is static. The role of the $C(r)$ function merits further discussion. Its square root represents the areal radius of a two-sphere [97]. When $C(r) = r^2$, the generic line element is expressed in Schwarzschild curvature coordinates [98]. In this case, the radius of the two-sphere coincides with the radial coordinate r. However, in models with a non-trivial $C(r)$ function (i.e. $C(r) \neq r^2$), the hypersurface radius does not coincide with the radial coordinate, but rather with a function of it. Such modifications can alter the location of the "centre" of a given space-time and allow the radial coordinate to take on negative values, which can in turn change the physical interpretation of r and the $A(r)$ and $B(r)$ functions [98]. For example, a non-trivial $C(r)$ may allow a distinct property of the space-time region to be represented such as a quantum volume [99], a different part of the Universe or an alternate Universe [100]. Regardless, it can be shown that any static SSS with a non-trivial $C(r)$ function may be re-written into an equivalent space-time with a trivial $C(r)$ function via a suitable coordinate change [92, 101, 102]. Returning to the derivation, equation (2.3) allows us to retrieve the associated metric tensor $g_{\mu\nu}$, which encodes the space-time curvature

$$g_{\mu\nu} = \begin{pmatrix} -A(r) & 0 & 0 & 0 \\ 0 & B(r) & 0 & 0 \\ 0 & 0 & C(r) & 0 \\ 0 & 0 & 0 & C(r)\sin^2\theta \end{pmatrix}. \tag{2.4}$$

[1] λ is an affine parameter providing a suitable way to describe motion along a geodesic without referring to the particular coordinates that describe the space-time.

From here, by inserting equation (2.4) into (2.1), the Lagrangian for a SSS is obtained as

$$\mathcal{L}(x,\dot{x}) = \frac{1}{2}\Big(-A(r)\dot{t}^2 + B(r)\dot{r}^2 + C(r)(\dot{\theta}^2 + \sin^2\theta\dot{\phi}^2)\Big). \tag{2.5}$$

2.1.2 Streamlining the Problem: Conservation and Symmetry

The following steps aim to simplify the problem at hand, through leveraging the symmetry inherent to the system and its associated conserved quantities. This is achieved by:

- considering the motion of massless particles along null geodesics, which in particular obey the relation $g_{\mu\nu}\dot{x}^\mu\dot{x}^\nu = 0$;
- focusing on equatorial plane geodesics, $\theta = \pi/2$, using the freedom granted by the spherical symmetry of the system;
- computing the constants of motion of the system, the energy and the angular momentum, via the Euler-Lagrange (E-L) equations.

The first step pertains the relation $g_{\mu\nu}\dot{x}^\mu\dot{x}^\nu = 0$, which is valid for null geodesics. Its physical meaning is revealed when a suitable affine parameter choice is taken in equation (2.2), such that the four-velocity components are compatible with the four-momentum ($\dot{x}^\mu = p^\mu$, with $p = (E,\mathbf{p})$). Through this approach, the aforementioned relation conveys the energy-momentum relation for massless particles in a curved space-time, which is conserved along a geodesic. Since the Lagrangian (2.1) is proportional to $g_{\mu\nu}\dot{x}^\mu\dot{x}^\nu$, we utilise the $g_{\mu\nu}\dot{x}^\mu\dot{x}^\nu = 0$ property to express equation (2.5) in the following manner

$$-A(r)\dot{t}^2 + B(r)\dot{r}^2 + C(r)(\dot{\theta}^2 + \sin^2\theta\dot{\phi}^2) = 0, \tag{2.6}$$

which will prove useful when re-arranging the terms in our equation of motion. Secondly, we can focus on equatorial plane geodesics (i.e. $\theta = \pi/2$) without loss of generality since the geodesic behaviour is independent of the polar angle (θ). When choosing such geodesics the system's Lagrangian (2.6) is further simplified to

$$-A(r)\dot{t}^2 + B(r)\dot{r}^2 + C(r)\dot{\phi}^2 = 0, \tag{2.7}$$

due to $\dot{\theta}^2 = 0$ and $\sin^2\theta = 1$. Lastly, we address the system's conserved physical quantities: the energy (E) and the azimuthal component of the angular momentum (L). The former is a constant of motion because the Lagrangian (2.5) has no explicit time dependence. Likewise, the Lagrangian (2.5) does not explicitly depend on the azimuthal coordinate, meaning the second quantity is conserved along the azimuthal component. Under such conditions, the aforementioned constants of motion can be calculated from the temporal and azimuthal components of the E-L equations

$$\frac{d}{d\lambda}\left(\frac{\partial\mathcal{L}}{\partial\dot{t}}\right) - \frac{\partial\mathcal{L}}{\partial t} = 0, \quad \frac{d}{d\lambda}\left(\frac{\partial\mathcal{L}}{\partial\dot{\phi}}\right) - \frac{\partial\mathcal{L}}{\partial\phi} = 0, \tag{2.8}$$

respectively. Performing this operation with respect to equation (2.7), we obtain the conserved quantities

$$E = A(r)\dot{t}, \quad L = C(r)\dot{\phi}. \tag{2.9}$$

2.1.3 Towards the equation of motion along a null geodesic

Omitting the generic functions' explicit dependence of r from here on, we combine the steps outlined in the previous subsection to transform equation (2.5) into a one-dimensional equation of motion; a differential equation that is a function of $\dot{r}^2$. Starting from equation (2.7), where the Lagrangian is already restricted to null geodesics and photons are assumed to be propagating along the equatorial plane, its terms are rearranged as

$$B\dot{r}^2 = A\dot{t}^2 - C\dot{\phi}^2. \tag{2.10}$$

The terms on the right-hand side (RHS) of the previous equation are multiplied and divided by their respective generic function, in a way that enables the introduction of the conserved quantities E and L

$$B\dot{r}^2 = \left(\frac{E^2}{A} - \frac{L^2}{C}\right). \tag{2.11}$$

Next, we isolate an L^2 factor and the generic function $A(r)$ from the equation's RHS, obtaining

$$AB\dot{r}^2 = L^2\left(\frac{E^2}{L^2} - \frac{A}{C}\right). \tag{2.12}$$

We then proceed by re-writing the previous expression into the following form:

$$AB\dot{r}^2 = \frac{1}{b^2} - V_{eff}(r), \tag{2.13}$$

where the first term in the RHS is recognized as the geodesic trajectory impact parameter $b \equiv L/E$, and the second term is associated to a radial effective potential [93] that reads as

$$V_{eff}(r) \equiv \frac{A(r)}{C(r)}. \tag{2.14}$$

We highlight that a factor L^2 was absorbed onto the left hand side (LHS) of our equation through a convenient affine parameter definition, between equation (2.12) and (2.13). This is permissible because if a null path is a geodesic for some affine parameter λ, it is so for any linear transformations of λ [92] (i.e. null geodesics are not restricted to a specific affine parameter). Throughout the literature one may find slightly varied versions of equation (2.13) (e.g. [41, 87, 93, 94, 103]), depending on how authors organise the terms in the equation and/or how they choose to define the effective potential (i.e. besides any alternate notations for the generic functions). Regardless, this expression and any of its renditions describe the behaviour of massless particles along null geodesics, in a SSS space-time. In this particular fashion, it can be understood as a one-dimensional equation of photon motion through an effective potential that is determined by the underlying space-time curvature. The photon motion depends on the ratio between the photon angular momentum L and their energy E. The latter ratio determines the impact parameter b in an observer's image plane, after a photon's trajectory is deflected by the effective potential. In other words, the impact parameter depends on the photon trajectory in a given space-time geometry. The effective potential depends instead on the underlying space-time geometry. It determines the turning point in a photon's trajectory for a fixed impact parameter. As we will discuss in section 2.5, photon trajectories can be sorted according to the number of half-orbits completed around a BH. This quantification scheme offers a practical means of discriminating between the observable features in the observer's image plane. For this purpose, it is therefore convenient to establish a relation between a

photon's deflection angle and its radial motion. This is achieved by, reintroducing the L^2 factor that was absorbed into the affine parameter definition into equation (2.13)

$$AB\dot{r}^2 = L^2\left(\frac{1}{b^2} - V_{eff}(r)\right), \tag{2.15}$$

and using the angular momentum conservation in (2.9), which contains the azimuthal velocity $\dot{\phi}$,

$$\frac{AB}{C^2}\frac{\dot{r}^2}{\dot{\phi}^2} = \frac{1}{b^2}\left(1 - b^2 V_{eff}(r)\right), \tag{2.16}$$

to solve the equation of motion with respect to $(dr/d\phi)^2$

$$\left(\frac{dr}{d\phi}\right)^2 = \frac{C^2}{b^2}\left(\frac{1 - b^2 V_{eff}(r)}{AB}\right). \tag{2.17}$$

We note that in the transition from (2.16) to (2.17), the following relation was used [87]:

$$\frac{\dot{r}^2}{\dot{\phi}^2} = \left(\frac{dr}{d\lambda}\frac{d\lambda}{d\phi}\right)^2 = \left(\frac{dr}{d\phi}\right)^2, \tag{2.18}$$

Finally, by applying the inverse square root to both sides of the bottom expression in equation (2.17), we finally reach the desired relation between the angle turned by every photon upon deflection by a black hole

$$\frac{d\phi}{dr} = \pm\frac{b}{C(r)}\sqrt{\frac{A(r)B(r)}{1 - b^2 V_{eff}(r)}}. \tag{2.19}$$

This equation is the main tool we shall employ in the ray-tracing behind the generation of black hole images (see discussion in chapter 3). To apply it to a given SSS, one must simply replace the generic functions $A(r)$, $B(r)$ and $C(r)$.

2.2 Effective null geodesics in SSS from Non-Linear Electrodynamics

In certain theoretical frameworks, such as non-linear electrodynamics (NED), electromagnetic fields exhibit non-trivial behavior near black holes. At such extreme space-time curvature conditions, the interaction between photons and these non-linear effects can significantly affect the propagation of light rays, influencing the optical appearance of a BH. Thus, the formalism for null geodesics needs to be upgraded when the matter fields threading the geometry belong to non-linear electrodynamics (NED): generalizations of Maxwell electrodynamics via non-linear higher order corrections in the field invariants. The first NED model was developed 90 years ago [104], as an attempt to construct a classical theory rid of the singularities associated with charged point-like particles. Despite falling in popularity in favour of quantum electrodynamics (QED), NED models have been long employed in the literature due to their connection with multiple research fields and domains such as String theory, effective approaches to Quantum Electrodynamics (QED), Cosmology, non-linear Optics, or Condensed Matter physics (e.g. [105–111]). Their application also extends to the realm of Black Hole physics, where such models have been effectively utilised as a tool to remove the central curvature singularity (e.g. [112–119]) and enhance the thermodynamical features of charged BHs [120–122]. Furthermore, they are very flexible in supporting many solutions of interest, even allowing the inclusion of scalar fields [119, 123, 124]. The growing relevance in the field of BHs precipitated the research onto the propagation of light in the con-

text of NEDs, by Novello et al. [125, 126]. Their pioneering work demonstrated that photons propagate along null geodesics of an effective space-time geometry, that is induced by the non-linear electrodynamic effects. This phenomenon can be understood as photons travelling through a dispersive medium [127, 128]. Since three (out of the sixteen) geometries considered in this work have been shown to be supported by specific NED models, exploring the repercussions of non-linear corrections in the vicinity of a black hole region becomes vital. Thus, we are driven to generalize the equations of geodesic motion in NED-supported geometries for the purpose of casting images of the corresponding objects.

In what follows, we derive the equation of motion for photons travelling along the null geodesics of an effective spherically symmetric geometry, in a similar spirit to the previous section. Towards this end, we shall follow the prescription by [125, 126] to procure the metric tensor required for the Lagrangian of an effective SSS space-time. With regards to NED, the following discussion will remain within the elements that are relevant to the derivation presented here and aligned with the NED supported geometries that are included in this work, which are all purely magnetic configurations. For a more detailed discussion on this matter the reader is referred to the lectures of Plebański [129], dedicated to the theoretical and mathematical framework of NED; Zwiebach's (2009) [130] chapter on NED and Born-Infeld theory; and the recent review by Sorokin (2022) [131] exposing the general properties of NED and some models inspired by it as well as over-viewing some of its applications, particularly in the context of Gravitation and Cosmology.

2.2.1 The Lagrangian of a SSS coupled to NED

NED theories are a class of field theories whose general structure is described by a Lagrangian density that is a functional form of two independent field invariants

$$\mathcal{L} = \mathcal{L}(F, G). \tag{2.20}$$

F and G are the two possible invariant quantities that can be constructed in a four-dimensional Minkowski (i.e. flat) space-time [132], from the electromagnetic tensor $F_{\mu\nu} = \partial_\mu A_\nu - \partial_\nu A_\mu$ and its Hodge dual $\overset{\star}{F}{}^{\mu\nu} = \frac{1}{2}\varepsilon^{\mu\nu\alpha\beta}F_{\alpha\beta}$, built from the Levi-Civita tensor (ε). We define them here as

$$\begin{aligned} F &= \frac{1}{4}F_{\mu\nu}F^{\mu\nu} = \frac{1}{2}(\mathbf{E}^2 - \mathbf{B}^2), \\ G &= \frac{1}{4}F_{\mu\nu}\overset{\star}{F}{}^{\mu\nu} = \mathbf{E}\cdot\mathbf{B}, \end{aligned} \tag{2.21}$$

both of which depend on the electric $\mathbf{E}$ and magnetic $\mathbf{B}$ field components. While the construction of analytical BH solutions with dyonic charges is highly complex, such solutions are easier to derive for purely electric or purely magnetically charged configurations [116], where the only non-vanishing field invariant is the electromagnetic field strength F (as implied by equations (2.21)). This reduces the Lagrangian functional form to an explicit dependence on F, as $\mathcal{L}(F)$. Such a scenario is of interest to us, since the NED supported space-times considered in this work concern purely magnetically charged black hole solutions. According to Novello et al. [125, 126], in geometries incorporating such NEDs, the paths of null particles are described by $g^{(e)}_{\mu\nu}\dot{x}^\mu\dot{x}^\nu = 0$, which is related to the inverse background geometry via[2]

$$g^{\mu\nu}_{(e)} = \mathcal{L}_F g^{\mu\nu} - \mathcal{L}_{FF}F^\mu{}_\alpha F^{\alpha\nu}\ , \tag{2.22}$$

[2] A factor of 4 appears in the self-interaction term in equation (14) from Novello et al. [125]. This difference stems from their prior definition of the field invariants F and G, from which the $1/4$ factor seen in equations (2.21) is absent.

where the subscript $_F$ is used to represent a derivative with respect to the field invariant F and the notation (e) is used to identify the effective space-time. Equation (2.22) can be re-written into a more convenient form by lowering an index via $F^{\mu}{}_{\alpha} = g^{\mu\nu}F_{\nu\alpha}$ and taking advantage of the field tensor's anti-symmetry $F_{\nu\alpha} = -F_{\alpha\nu}$, to obtain

$$g^{\mu\nu}_{(e)} = \mathcal{L}_F g^{\mu\nu} + \mathcal{L}_{FF} g^{\mu\beta} F_{\alpha\beta} F^{\alpha\nu} \ . \tag{2.23}$$

By the definition of inverse metric tensor $g^{\mu\sigma}g_{\sigma\nu} = \delta^{\mu}_{\nu}$ we obtain the effective metric tensor $g^{(e)}_{\mu\nu}$

$$g^{(e)}_{\mu\nu} = \frac{g_{\mu\nu}}{\mathcal{L}_F + \mathcal{L}_{FF} F_{\alpha\beta} F^{\alpha\beta}} \ . \tag{2.24}$$

It is this definition that is replaced into the Lagrangian density and invariant line element given by equations (2.1) and (2.2), respectively. Doing so allows us to replicate the derivation performed in section 2.1 for an effective geometry. Observing the above equation, it is possible to see that the Lagrangian $\mathcal{L}(F)$ and its partial derivatives play an important role in determining the metric tensor's components. When the Lagrangian density coupling to the matter fields behaves as $\mathcal{L}(F) \to F$, the linear Maxwell Electrodynamics are recovered. In such a case, the derivatives with respect to the field strength are $\mathcal{L}_F = 1$ and $\mathcal{L}_{FF} = 0$, which causes the effective metric tensor to reduce to the background metric tensor, as expected. To compute the effective metric tensor's components, let the ansatz for purely magnetic configurations be given by $A_{\mu} = q_m \cos\theta \delta^{\phi}_{\mu}$, wherein q_m corresponds to the magnetic charge. Substituting this definition into the field tensor $F_{\mu\nu}$ yields two non-vanishing components of the field strength F

$$F_{\phi\theta} = q_m \sin\theta = -F_{\theta\phi}. \tag{2.25}$$

Consequently, the NED field equations (2.21) return a single solution for the invariant F, as given by

$$F = \frac{1}{4}F_{\mu\nu}F^{\mu\nu} = \frac{1}{2}F_{\theta\phi}F^{\theta\phi} = \frac{q_m^2}{2r^4}. \tag{2.26}$$

Here we have capitalized on the invariance of a volume element $d^4x\sqrt{-g}$ under a coordinate change, which is $1 = r^2\sin\theta$, between Cartesian and Spherical coordinates. We are now in possession of all the ingredients required to determine the components of the effective metric tensor (2.24). Considering a background metric given by (2.4) and the results from equation (2.26), the effective metric tensor appears as

$$g^{(e)}_{\mu\nu} = \begin{pmatrix} -\frac{A(r)}{h(r)} & 0 & 0 & 0 \\ 0 & \frac{B(r)}{h(r)} & 0 & 0 \\ 0 & 0 & \frac{C(r)}{H(r)} & 0 \\ 0 & 0 & 0 & \frac{C(r)}{H(r)}\sin^2\theta \end{pmatrix}, \tag{2.27}$$

where we define two functions, $H(r) = \mathcal{L}_F + 2F\mathcal{L}_{FF}$ and $h(r) = \mathcal{L}_F$, to encode the deviations between the effective and background metrics. The corresponding line element is obtained by plugging the effective metric tensor (2.27) into equation (2.2)

$$ds^2_{(e)} = -\frac{A(r)}{h(r)}dt^2 + \frac{B(r)}{h(r)}dr^2 + \frac{C(r)}{H(r)}d\Omega^2 \ , \tag{2.28}$$

describing the line element of an effective, magnetically charged and spherically symmetric geometry.

Similarly, by introducing the tensor (2.27) into equation (2.1), the Lagrangian for an effective SSS takes the form

$$\mathcal{L}(x,\dot{x}) = \frac{1}{2}\Big(-\frac{A(r)}{h(r)}\dot{t}^2 + \frac{B(r)}{h(r)}\dot{r}^2 + \frac{C(r)}{H(r)}(\dot{\theta}^2 + \sin^2\theta\dot{\phi}^2)\Big). \tag{2.29}$$

2.2.2 Towards the equation of motion along an effective null geodesic

Henceforth, equation (2.29) is transformed into a one-dimensional equation of motion according to the steps outlined in subsection 2.1.2. The explicit dependence of r will be omitted from some of the equations that follow. We begin by invoking the relation $g^{(e)}_{\mu\nu}\dot{x}^\mu\dot{x}^\nu = 0$, to which null particles travelling in an effective geometry obey, as well as assuming the null particle motion to take place along the equatorial plane $\theta = \pi/2$, without loss of generality. From these considerations, equation (2.29) is replaced by

$$H(-A\dot{t}^2 + B\dot{r}^2) + hC\dot{\phi}^2 = 0\,, \tag{2.30}$$

where we also multiplied both sides of the above equation by the functions $H(r)$ and $h(r)$. Subsequently, we introduce the energy and momentum conservation relations, as calculated for the Lagrangian (2.30) according to the E-L equations (2.8). The resulting energy (E) and azimuthal component of the angular momentum (L) read as

$$E = HA\dot{t}, \quad L = hC\dot{\phi}, \tag{2.31}$$

allowing the Lagrangian to be expressed as

$$BH\dot{r}^2 = \left(\frac{E^2}{AH} - \frac{L^2}{Ch}\right)\,. \tag{2.32}$$

Next, we isolate an L^2 factor, as well as the functions $A(r)$ and $H(r)$, from the RHS of the equation. In the process we revoke the angular momentum conservation in (2.31), leading to

$$AB\frac{\dot{r}^2}{\dot{\phi}^2} = \frac{C^2h^2}{H^2}\left(\frac{1}{b^2} - V^{(e)}_{eff}(r)\right)\,, \tag{2.33}$$

where in the RHS we have defined once more the geodesic trajectory impact parameter $b \equiv L/E$ and the radially dependent potential $V^{(e)}_{eff}(r)$ as

$$V^{(e)}_{eff}(r) \equiv \frac{A(r)}{C(r)}\frac{H(r)}{h(r)}\,. \tag{2.34}$$

Thus, we have arrived at the equation of motion of null particles travelling in a magnetically charged effective geometry. Like its counterpart for background geodesics, one may find slightly distinct versions of equation (2.33) in BH literature due to differences in notation and how the terms are organized (e.g. [133–135]). Comparing equation (2.33) with equation (2.13), the contribution of the functions $H(r)$ and $h(r)$ stands out. Specifically, the effective potential that depended on the background geometry now reflects the properties of the effective geometry; a consequence of the nonlinear effects introduced by these functions. However, in spite of their presence, both the impact parameter and effective potential remain qualitatively the same. The former retains its dependence on the photon trajectory, dictated by the ratio between the conserved angular momentum and the photon energy. In contrast, the latter depends solely on the space-time geometry.

With the aim of studying photon trajectories, relating the photon's deflection angle with its radial motion, we take equation (2.33) and apply the relation (2.18) to finally reach

$$\frac{d\phi}{dr} = \pm\frac{b}{C(r)}\frac{H(r)}{h(r)}\sqrt{\frac{A(r)B(r)}{1-b^2V^e_{eff}(r)}}\,. \tag{2.35}$$

This equation forms the backbone of our ray-tracing algorithm, that is used to simulate the appearance of the NED supported BH geometries included in our analysis. Unlike equation (2.19), using it requires knowledge of the NED Lagrangian $\mathcal{L}(F)$ and computation of its derivatives, in addition to the generic functions describing the background geometry.

2.3 Photon spheres and the Critical Curve

Having derived the null geodesic equations of motion, we now seek to characterize the optical appearance of a black hole according to the different types of light trajectories. One remarkable consequence of the extreme space-time curvature near black holes is the deflection of such trajectories into unstable bound orbits [136]. These correspond to circular null geodesics (i.e. closed photon trajectories) that are highly susceptible to small radial perturbations [41]. In a SSS, the inherent symmetry of the system confines these geodesics to planes that intersect the central point of the space-time [137]. The region comprising unstable circular orbits forms a spherical surface, that is dubbed as *photon sphere*[3] [41, 138] (also referred as *light-ring*: e.g. [49, 139, 140]). Although it is a theoretical construct, the photon sphere is physically relevant for the characterization of black hole images because it sets the boundary between the geodesics that are captured by a BH and intersect the event horizon, from those that escape towards infinity. Thus, its presence has profound implications in the optical appearance of a black hole, giving rise to relativistic images [138] that, under specific illumination settings, manifest as observable signatures which can be used to estimate the properties of the underlying space-time geometry [51, 70, 81, 86, 89, 141]. Naturally this has sparked the scientific community's interest in this concept and numerous approaches have been developed for its study, ranging between geometric and topological methods [41, 136, 142–146].

In what follows, we present the most common approach to studying circular photon orbits, which involves the effective potential of photons propagating in a black hole space-time [93]. Equations (2.13) and (2.14) (equations (2.33) and (2.34) in the case of effective geometries) provide insights into the existence and location of photon spheres, as well as the (in)stability and impact parameter of its circular orbits, in SSS. Since the orbits in an unstable photon sphere are circular, they are characterized by constant radial motion (i.e. $\dot{r} = 0$ or $d\phi/dr \to \infty$). Moreover, circular orbits are located at critical points (i.e. peaks) of the effective potential, with (un)stable bound orbits corresponding to critical minima (maxima). Mathematically, unstable circular orbits are found as solutions of the following equations

$$V'_{eff}(r_{ps}) = 0\,, \qquad V''_{eff}(r_{ps}) < 0\,, \qquad b_c^2 = V_{eff}^{-1}(r_{ps})\,, \tag{2.36}$$

where the prime indicates a derivative with respect to the radial coordinate, r_{ps} is the photon sphere radius, and b_c identifies the critical impact parameter associated with the circular lightlike geodesics. The first equation in (2.36) is the condition for the existence of photon spheres. Substituting the effective potential (2.14) into it and computing the derivative leads to the so-called photon sphere equation, in a

[3] In the case of an axially symmetric space-time, this region is known as a *photon shell*, made of unstable spherical orbits [137].

spherically symmetric geometry [41],

$$C'(r_{ps})A(r_{ps}) - C(r_{ps})A'(r_{ps}) = 0\ . \tag{2.37}$$

Depending on the shape of the effective potential, this equation may be satisfied for several radius values r or have no real solutions, signifying the presence of multiple photon spheres or the absence of a photon sphere, respectively. In the former case, one must distinguish between unstable photon spheres from stable photon spheres[4]; a condition that is mathematically expressed by the second derivative of the effective potential, the middle equation in (2.36), when evaluated at r_{ps}. The third equation in (2.36) relates the light rays in the photon sphere with the impact parameter in the observer's screen. The photon sphere is mapped into a circular *critical curve* in the image plane of an observer [47], located at the critical impact parameter b_c. The critical impact parameter acts as an accessibility condition for the light trajectories [93], splitting the light rays issued from the observer's screen backwards towards the black hole into two well-distinguished regions: light rays with an impact parameter $b > b_c$ cannot make it past the potential barrier and their trajectory approaches a minimum turning point at some $r > r_{ps}$ before escaping towards the infinity; light rays for which $b < b_c$ are able to overcome the potential barrier and their trajectory eventually intersects the event horizon. Those that have an impact parameter $b \gtrsim b_c$ spiral asymptotically towards the photon sphere and may linger there indefinitely, turning the black hole an arbitrarily large number of times before being released to asymptotic infinity. Thus, the critical curve is defined as the boundary in an observer's sky that separates the scattered orbits from the captured ones.

Together the equations in (2.36) encode the information on the unstable photon sphere(s) and critical curve(s) in a SSS. They reveal that the location of the photon sphere, the impact parameter of the critical curve, and even the instability of the light orbits, are deeply entwined with the properties of the space-time geometry, as described by the generic functions. Furthermore, by replacing the potential in equations (2.36), with its NED equivalent (i.e. equation (2.34)), the aforementioned reasoning still applies. It follows immediately that the non-linear contributions that lead to an effective geometry influence the location and stability of circular orbits in the space-time, and consequently, the photon sphere and critical curve associated with them. On a side note, the radial effective potential also provides an alternate means of computing the horizon radius r_H (i.e. or radii in models where more than one event horizon is present) for a given spherically symmetric geometry, by solving $V_{eff}(r_H) = 0$. As an application example of equations (2.36), consider the Schwarzschild space time [11], for which the generic functions read as

$$A(r) = B^{-1}(r) = \left(1 - \frac{2M}{r}\right)\ , \qquad C(r) = r^2\ . \tag{2.38}$$

Substituting the above expressions in the definition of effective potential (2.14) and into (2.36) reveals the presence of a single photon sphere at $r_{ps} = 3M$, with a critical impact parameter $b_c = 3\sqrt{3}M \sim 5.196M$, a result that has been well established in BH literature [19, 21]. Thus, the photon sphere and the critical curve are essential theoretical concepts of black hole images that are extremely useful in distinguishing between different light trajectories. In particular, the critical curve plays an important role in the definition of the concept of black hole shadow and the photon ring, which we examine in the following sections.

[4] Regions in which circular light trajectories remain stable under radial perturbations, also known as *anti-photon spheres* [147, 148].

2.4 Black Hole Shadow

Having been introduced almost 25 years ago, the term black hole shadow has become a staple in BH literature. To quote the Event Horizon Telescope collaboration's 2019 press release: "The shadow of a black hole is the closest we can come to an image of the black hole itself, a completely dark object from which light cannot escape." [149]. However, despite its prevalence, the usage of the term is still under debate due to ambiguity over the predictions on its size, shape, and sensitivity to astrophysical emission assumptions [47, 71, 83, 86, 150]. Seeing as the BH shadow is a key ingredient in the work we present here, it is therefore in our interest to establish a clear understanding of the terminology surrounding this concept. In this regard, we aim to provide a brief overview of the state of the art surrounding BH shadows, covering topics such as the shadow radius of a static and spherically symmetric geometry, and the EHT calibrated measurement of Sgr A* shadow. After all, studying shadows offers a unique pathway towards uncovering properties of the shadow caster, the surface they are cast upon, and even the light emitting source, when these aspects are difficult to resolve otherwise. For example, in ancient times, careful observation of shadows has led to some of the most ingenious insights, such as tracking the passage of time and seasons, inferring the round shape of the Earth and even calculating its circumference. In the case of BHs, shadows owe their appeal to being one of the very few ways to directly studying them, providing a testbed to the theory of General Relativity and its many alternatives.

So what exactly is the black hole shadow? To initiate our discussion, we first address a broader query: what is a "shadow"? By definition, the *shadow* (noun) refers to: "1. the dark figure cast upon a surface by a body intercepting the rays from a source of light; 2. partial darkness or obscurity within a part of space from which rays from a source of light are cut off by an interposed opaque body" [151]. The preceding statements offer a comprehensive understanding of shadows, that not only includes the more traditional notion of a dark projection that is projected over a surface (e.g. a shadow of an object or a person, cast on the ground), but also the phenomenon of a dark silhouette that is seen relative to a bright backdrop (e.g. the silhouette of a boat against the sunset). The concept of black hole shadow is an extension of these notions, in particular the latter, to the realm of GR and gravitational light ray deflection. Essentially, it can be effectively understood as the dark silhouette of a BH when observed against an illuminated background [87]. The term black hole shadow was first coined by Falcke et al. [31], who used it to describe the region in an observer's image plane corresponding to the interior of the critical curve. In their original theoretical construction, the authors referred to the shadow as the dark region created in an observer's sky by a black hole surrounded by optically thin emission. To better visualize this concept, we recall the definition of critical curve presented in the previous section. By tracing the null geodesics from an observer to a BH, it is possible to split the null geodesics between scattered trajectories and captured trajectories. We illustrate this behaviour in Figure 2.1, for a Schwarzschild BH.

Let us now consider the idealized scenario in which a BH and an observer are confined in a spherical uniform emitter (i.e. no light sources between a BH and an observer, but light is evenly distributed everywhere else in the Universe). In this case, we expect that photons arrive at the observer if they came from a light source at the infinity (e.g. the gold trajectories in the Figure), but not if the corresponding geodesics emerge from the BH event horizon (e.g. the black trajectories in the Figure). This manifests as a dark two-dimensional projection in the observer's sky - the black hole shadow - surrounded by light. Physically, this can be interpreted as the unstable photon sphere acting as the obstacle to the lightlike trajectories, causing the shadow to be projected. This draws attention to the common misconception that the black hole shadow is an image of the event horizon, when instead it is a gravitationally enhanced image of the photon sphere [83]. The edge of the shadow coincides with the critical curve.

2.4 Black Hole Shadow

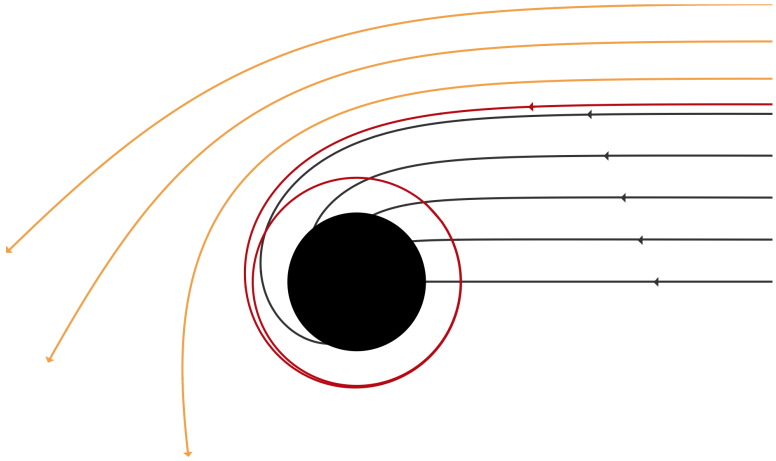

Figure 2.1: Examples of backwards traced photon trajectories, from an observer's image plane (on the right side) to a Schwarzschild black hole (black circle): scattered orbits (gold); captured orbits (black); unstable bound orbits (red).

An important criterion for the existence of a shadow is that any spherically symmetric and asymptotically flat space-time, that is endowed with an unstable photon sphere, will cast a shadow [87, 136]. Since every spherically symmetric BH geometry contains an unstable photon sphere [41], a shadow inevitably occurs for them. However, this criterion carries a more profound implication. It precludes the shadow from being a unique feature of BHs. In this regard, there are several alternative geometries that are known to possess unstable photon spheres and are therefore able to project a shadow, such as wormholes, naked singularities, and exotic compact objects (ECOs) (e.g. Gravastars) [58, 62, 66, 69, 152, 153]. Note that the lack of a photon sphere does not entail an absence of a shadow. Indeed, it has been shown that specific horizonless configurations are able to cast them, due to having distinct space-time topologies allowing a critical impact parameter to occur in the image plane[154–156]. In summary, while the aforementioned criterion is a sufficient condition for the existence of a shadow, it is not a necessary one.

Because photon spheres are an inherent property of the geodesics and the underlying geometry, the shadow bears a fingerprint of its caster [136]. The shape of the shadow depends on the geometry spin and observer's inclination angle, and even on the integrability of geodesic equations [157]. For a static (spherically symmetric) BH, for which the critical curve is a circumference, the projected shadow appears as a dark circle in the observer's sky, whereas for spinning (axially symmetric) BH, where the critical curve depends on the BH spin and the observer's inclination angle, the shadow accordingly adopts an asymmetrical D-shape [22, 31, 94]. Moreover, under specific circumstances (e.g. chaotic photon motion, super-spin) the shadow boundary diverges from the previous two, into more exotic shapes [158–160]. The size of the shadow's edge is also determined by the presence of medium that acts upon the photon trajectories [87]. The latter may take place, for example, when a plasma is permeating through a background geometry [44, 45] or when an effective geometry is induced by non-linear corrections to Maxwell electrodynamics [161, 162]. Collectively, these aspects deem the shadow a highly appealing target of observation. Its unique signature and sensitivity to the space-time geometry motivated the observational efforts to capture images of black hole shadows, that culminated in the groundbreaking images released by the Event Horizon Telescope collaboration in 2019 [32] and 2022 [33].

2.4.1 The shadow radius of a SSS

Analytical calculations of the edge of the shadow are plenty throughout literature [5], having been obtained for asymptotically flat SSS (e.g. [103, 163, 164]), axially symmetric space-times (e.g. [22, 34, 165]), non-asymptotically flat space-times SSS (e.g. [46]), or for SSS filled with a non-magnetized cold plasma (e.g. [44]). Such methods are not restricted by the underlying space-time. Rather, their application is contingent on the null geodesic equation being completely integrable [87, 136]. Failing to meet this condition, one must resort to numerical approaches to compute the shadow's boundary.

In what follows we present the Lagrangian approach towards deriving the formula of the shadow radius r_{sh}, of an asymptotically flat, static and spherically symmetric geometry, with the aim of demonstrating the equivalency between this quantity and the critical impact parameter. We begin our considerations from a static observer located at some distance r_O from a black hole of mass M, with its line of sight along the radial coordinate axis. Suppose the BH space-time is described by static and spherically symmetric line element, as given by equation (2.3). A null geodesic traced from the observer to the BH forms an inclination angle α with respect to the observer's line of sight (as illustrated in Figure 2.2).

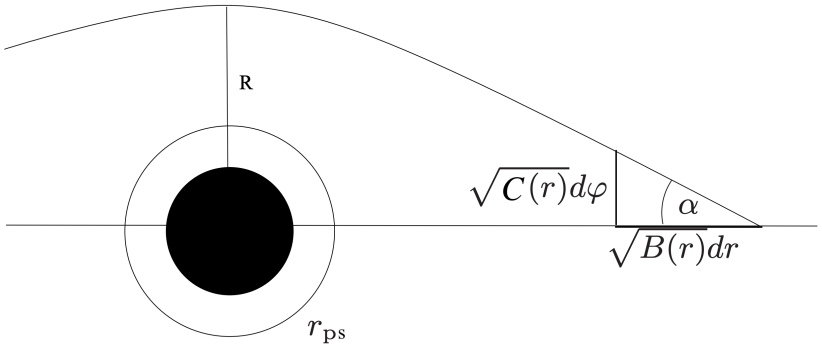

Figure 2.2: The angle α between a light ray and an observer's line of sight, along the radial axis, for an observer located at some distance from a spherically symmetric black hole (represented by the black circle). The radial and azimuthal components of the light ray are given by $\sqrt{B(r)}dr$ and $\sqrt{C(r)}d\phi$, respectively. R denotes the turning point of the light ray and r_{ps} marks the radius of the photon sphere.

We assume that light propagates along such geodesics without being influenced by matter. In a curved space-time, an angle must be assessed according to the metric of a curved 3-space [163], $ds^2 = B(r)dr^2 + C(r)d\Omega^2$. It follows that the angle α may be expressed as [87, 163]

$$\cot\alpha = \frac{\sqrt{B(r)}}{\sqrt{C(r)}}\frac{dr}{d\phi}. \tag{2.39}$$

Squaring both sides of the above equation and inserting equation (2.17) on the RHS, returns

$$\cot^2\alpha = \frac{1}{b^2}\frac{C(r)}{A(r)}\left(1 - b^2\frac{A(r)}{C(r)}\right) = \frac{C(r)}{A(r)}\frac{1}{b^2} - 1\,, \tag{2.40}$$

where we make use of the trigonometric relation $1 + \cot^2\alpha = \csc^2\alpha$ to simplify the result to

$$\sin^2\alpha = b^2\frac{A(r)}{C(r)}\,, \tag{2.41}$$

[5] The reader to the work of Perlick & Tsupko (2022) [87] and references therein, for a comprehensive review on analytical calculations of BH shadows.

which is valid at any point of a given null geodesic. With this in mind, we shift the focus to null geodesics that asymptotically approach the critical curve. By the definition of black hole shadow, the edge of the BH shadow coincides with the critical curve. Consequently, by considering light rays such that $b \to b_c$, the angle α conveys the shadow's angular radius α_{sh}, and we may write

$$\sin^2 \alpha_{sh} = b_c^2 \frac{A(r_O)}{C(r_O)} \,, \tag{2.42}$$

relative to an observer at r_O. Applying the square root to both sides of the equation and keeping the positive branch, one obtains

$$\sin \alpha_{sh} = b_c \sqrt{\frac{A(r_O)}{C(r_O)}} \,. \tag{2.43}$$

We are interested on the angular size of the BH shadow for a distant observer (i.e. $r \gg M$). This is the quantity that can be measured in an observer's sky. At such large distances, the shadow's angular size becomes significantly small. Under these assumptions, the small angle approximation (i.e. $\sin\alpha = \alpha + \mathcal{O}(\alpha^3)$) may be applied to simplify the previous equation into

$$\alpha_{sh} = b_c \sqrt{\frac{A(r_O)}{C(r_O)}} \,. \tag{2.44}$$

As it stands, the previous equation describes the angular shadow radius for a SSS. The angular radius is a dimensionless quantity, whereas the critical impact parameter has a dimension of length. We may obtain the linear shadow radius r_{sh} via the formula $\alpha = r_{sh}/r_O$ [166], which is valid for small angles, and have both sides of the equation according to the same dimensions. In doing so, equation (2.44) may be re-written as

$$\frac{r_{sh}}{r_O} = b_c \sqrt{\frac{A(r_O)}{C(r_O)}} \,, \tag{2.45}$$

which resolves to

$$r_{sh} = b_c \sqrt{A(r_O)} \,, \tag{2.46}$$

when the generic function $C(r)$ for the background space-time is of the form $C(r) = r^2$. Taking into consideration space-time geometries that are asymptotically flat (i.e. $A(r) \to 1$, $B(r) \to 1$, and $C(r)/r^2 \to 1$ at $r \to \infty$), we obtain the equivalency between the shadow radius and the critical impact parameter

$$r_{sh} \equiv b_c = \frac{r_{ps}}{\sqrt{A(r_{ps})}} \,, \tag{2.47}$$

where we also resort to the critical impact parameter equation in (2.36). This final expression describes the shadow radius for any general static and spherically symmetric geometry that is asymptotically flat[6]. It highlights the link between the shadow, the photon sphere, and the critical impact parameter. It can also be seen that the space-time geometry itself plays an important part in determining the shadow radius. A comparison of equations (2.47) and (2.46) reveals that the equivalency between the shadow radius and the critical impact parameter is broken when the space-time geometry is not asymptotically flat. Notably, when geometries are not asymptotically flat (i.e. $A(r) \to \infty$, $B(r) \to \infty$, and $C(r)/r^2 \to \infty$ at $r \to \infty$) the observer's radial position (2.46) may provide a non-negligible contribution to the shadow radius.

[6] A similar expression is obtained for the shadow radius of an asymptotically flat, NED supported SSS. The main difference will be the presence of the a factor $\sqrt{h(r_{ps})/H(r_{ps})}$, containing the non-linear contributions in the $H(r)$ and $h(r)$ functions.

An alternative method to deal with such shortcomings is to consider a comoving observer relative to a black hole [46]. As an example, we compute the shadow radius according to equation (2.47) for the Schwarzschild geometry (2.38). This yields $r_{sh} = 3\sqrt{3}M$, coinciding with the critical impact parameter computed in section 2.3, and a much larger value than the Schwarzschild event horizon $r_h = 2M$.

2.4.2 The Central Brightness Depression and the nature of the shadow

At this point in our discussion, we take the opportunity to establish the definition of shadow that is adopted throughout this thesis. Namely, the term shadow is used to refer to the region in the observer's image plane that is delimited by the critical curve. Note that we purposefully avoid identifying the shadow with the dark region in an observer's sky. As it turns out, the latter is incompatible with the interior of the critical curve in non-spherical emission scenarios. This discrepancy has motivated the recent literature debate involving the application of the term shadow [47, 71, 83, 150].

The notion of black hole shadow and its relation to the dark region in the observer's image plane was disputed by Gralla, Holz, & Wald (2019) [47]. In their work, the authors presented examples of a Schwarzschild BH framed in a number of toy emission scenarios, where the size of the dark region did not coincide with that of the critical curve. This included: a BH backlit by an infinite planar screen of uniform brightness, in which the dark region extended beyond the critical curve; a BH surrounded by an optically and geometrically thin accretion disk, viewed from a face-on orientation (i.e. the observer's line of sight is perpendicularly aligned with the BH's equatorial plane), where the size and appearance of the dark region depended on the accretion disk's emission profile. The latter scenario has been found to occur not only in infinitesimally thin disk equatorial flows, but also as long as there are gaps in the emission region [47, 83]. On the other hand, when the accretion flow near a BH is characterized by a spherical structure and optically thin emission, this ambiguity is resolved, as the dark region in the image plane coincides with the interior of the critical curve [38, 83], in agreement with Falcke's original view [31]. Altogether, these results have raised concerns about the concept of black hole shadow, when interpreted as the region of decreased brightness in the observer's sky, and launched a debate on whether or not it should be regarded as a generic prediction of GR that is a model-independent phenomenon. In practise, however, neither of the previous idealized accretion models is able to capture the complex and turbulent structure of the hot plasma accreting around black holes [89].

The term *central brightness depression* (CBD) emerged amidst the debate, to describe the central decrease in brightness that is characteristic of BHs surrounded by optically thin accretion disks [83]. This is a feature whose shape is sensitive to astrophysical assumptions of the accretion flow, in addition to properties of the background geometry [34, 89]. In particular, for the size of the CBD appears larger or smaller than the critical curve depending on the location of the accretion disk's inner radius. This concept's definition is consistent with previous findings on the appearance of BHs surrounded by thin accretion disks [27, 34, 47]. More importantly, the distinction set by this concept is instrumental towards understanding the "true" nature of the black hole shadow. Whereas the CBD encompasses any "darkness" that is seen beyond the critical curve, the shadow does not. Let us shift our attention to the origin of such darkness. Inside the critical curve, all the null geodesics intersect the event horizon. Immediately, it follows that any darkness that is seen by an external observer stems from an extremely lensed image of the event horizon. Outside the critical curve, all the null geodesics are scattered to infinity. If there are gaps in the emission causing a darkness to appear outside the critical curve, then this darkness is still filled with emission from lensed images of distant sources in the entire Universe [83]. In essence, the nature of the shadow pertains the darkness that is seen inside the critical curve which is fundamentally

different from any darkness that is seen outside it. Therefore, for the sake of our analysis we shall reserve the word shadow for the region completely filling the critical curve and associated to Falcke's view and the EHT bounds described in the next section, and use CBD to identify the dark region that is seen when the accretion disk is infinitesimally thin.

2.4.3 The EHT shadow boundary constraints

The precise size of the outer edge of the CBD cannot be directly determined by the EHT collaboration, given the instrumental lack of photon sensitivity below a $\sim 10\%$ threshold of the peak luminosity [80, 167], implying the shadow's angular radius is not actually observable. Nonetheless, the collaboration copes with this limitation by appealing to the inner radius of the bright ring of radiation created by the direct emission, reporting that it can be used as a proxy for the shadow's angular radius (and therefore the shadow radius), provided the systematic uncertainties in relating these features are accounted for. A measurement of the inner radius of the emission ring is achievable as long as the following conditions are satisfied [31, 80, 168]:

- A sufficiently bright and strongly lensed supply of photons exists near the horizon;
- The source is geometrically thick and optically thin at the observing wavelengths/frequencies.

At the operating wavelength of 1.3 mm, of the EHT collaboration's VLBI network, the hot accretion flow at Sgr A* meets these criteria [169]. In addition to the previous conditions, a calibration factor α_c connecting the diameter of the (measured) bright radiation ring $\hat{d}_m$ with that of the corresponding shadow d_{sh} is required, relating the two as $\hat{d}_m = \alpha_c d_{sh}$. This is done in order to quantify the offset between these two features and assess the reliability of the shadow size inference via the diameter of the bright ring, by taking into account various observational and theoretical biases (e.g. formal measurements, model-fitting approaches, theoretical model assumptions) [80]. Such inference is made possible with the aid of the mass-to-distance ratio M/D of Sgr A*, a quantity that has been obtained through detailed tracking of the orbital dynamics of individual stars, located in the central stellar cluster in the innermost region of the galactic center (known as S-stars), [170–172] (see [80] and references therein), that allows the estimation of the central body's angular size $\theta_g = M/D$ [80]. In particular, the $S0-2$ star has been independently tracked with two sets of instruments − the Keck Observatory and the Very Large Telescope Interferometer (VLTI) − whose combined (and uncorrelated) data allow to quantify the fractional deviation δ between the inferred shadow diameter and the predicted shadow diameter of a Schwarzschild black hole, $d_{sh,Sch} = 6\sqrt{3}M$ (of angular size $\theta_{sh,Sch} = d_{sh,Sch}/D = 6\sqrt{3}\ \theta_g$) as [80, 81]

$$\delta \equiv \frac{\hat{d}_m}{\alpha_c\ d_{sh,Sch}} - 1 = \frac{d_{sh}}{d_{sh,Sch}} - 1 \approx -0.060 \pm 0.065\ . \tag{2.48}$$

In turn, this constraint can be transformed into the uncertainty in the shadow's radius as

$$r_{sh} = r_{sh,Sch}(\delta + 1)\ . \tag{2.49}$$

Thus, by considering the Schwarzschild BH shadow radius, $r_{sh,Sch} = 3\sqrt{3}M$, the shadow radius of Sgr A* is constrained between [81]

$$4.55 \lesssim r_{sh}/M \lesssim 5.22\ , \tag{2.50}$$

at 1σ deviation and

$$4.21 \lesssim r_{sh}/M \lesssim 5.56\ , \tag{2.51}$$

at 2σ deviation, assuming a normal distribution for the uncertainty. As one can see from these inferred constraints, the lower bounds on the shadow radius are more generous than the upper bounds. Subsequently, the constraints offered by this inference are less restrictive towards alternative spherically symmetric geometries that reduce the size of the shadow, which is the majority of the models considered in this dissertation, as we shall discuss in section 3.3. Assuming the validity of this correlation, Vea utilized the above shadow radius bounds to test the parameter space of several spherically symmetric geometries, by assessing the compatibility of their parameter dependent shadow radius.

In light of the work presented here, there are some caveats related with the use of the previous inference that must be addressed. According to the EHT collaboration [80], the inference of the shadow size of Sgr A* must be subjected to a calibration factor, which quantifies the degree to which the diameter of the peak brightness of the emission ring tracks the diameter of the shadow. The latter will differ from the true ring diameter d_m due to theoretical $\alpha_1 \equiv d_m/d_{sh}$ sources of uncertainty, and from the measured ring diameter due to measurement $\alpha_2 \equiv \hat{d}_m/d_m$ sources of uncertainty. The calibration factor multiplicatively accounts for both types of uncertainties as $\alpha_c = \alpha_1 \times \alpha_2$.

We are particularly interested in the theoretical biases contained in the α_1 ratio, arising from the assumptions made about the background space-time geometry and its properties, and the accretion flow surrounding it. To quantify this factor, the EHT collaboration simulate BH images employing three types of tests to explore a wide range of effects connected with the latter assumptions [80]. The collaboration presumes the space-time around Sgr A* is described by Kerr-Schwarzschild conditions as the default case for two of the tests, and only considers two alternative metrics for the third category of tests [169]. By extrapolating the validity of the inferred shadow size of Sgr A* (and the bounds imposed by equation (2.51)) to any alternative geometries beyond those considered by the EHT, such as the ones considered in this work and/or those in Vea, the analysis implicitly assumes the EHT's supposition of the Schwarzschild geometry for the connection provided by the fractional deviation δ. Should such geometries significantly modify the theoretical calibration factor, and by extension the fractional deviation, the domain of validity of their parameter space could be extended beyond the previous shadow bounds. One could mitigate this bias by conducting the same tests as the EHT collaboration, for each of the alternative geometries considered here. However, such an endeavour far exceeds the scope of the present work.

Overall, the EHT's observational efforts have launched the era of black hole observations, bringing us closer to understanding the supermassive bodies located at the centre of the M87 and Milky Way galaxies. The results from these observations have spurred numerous literature works on black holes and accretion disks, pertaining fundamental tests of GR and alternative theories of gravity, accretion flow physics, and more (e.g. [162, 173–177]). In particular, the shadow size bounds of Sgr A* have been employed by Vea to constrain the parameter space of a diverse selection of spherically symmetric geometries, motivated by fundamental or phenomenological considerations. Such tests rely on the validity of the previously discussed inference and the assumptions upon which it holds. Furthermore, because the shadow can be degenerate with respect to different space-time geometries [69, 85], these constraints cannot single out specific metrics to represent the current images. Conversely, where the shadow can be a degenerate feature, the gravitational lensing remains a generic one [85]. This has driven theoretical research onto another unique visual signature of black holes - the photon ring - whose properties present a promising, model independent alternative, to test GR at future higher resolution VLBI campaigns.

2.5 Photon Ring

In addition to a CBD, the visual appearance of black holes surrounded by optically thin emission is characterized by a ring-like feature of increased brightness, caused by the gravitational lensing of light passing near the photon sphere [47]. This feature, known as the photon ring, has garnered attention in recent years, in connection to the EHT observations of the central supermassive objects of M87 and the Milky Way and the concerns on the shadow's reliability as a generic prediction of GR. Owing to its sensitivity to the underlying space-time and to favorable prospects for observation with future VLBI projects, researchers have raised the possibility of using the photon ring as an observational discriminator of space-time geometry [52, 70, 71, 82, 178, 179]. Thus, by exploring the concept of photon ring, we aim to deepen our understanding of black hole astrophysics and pave the way for the analysis presented in the coming chapters. Towards this end, we start by setting the conceptual definition of photon ring, that is adopted for this work, shedding light on its nature and characteristics. In this regard, we revisit the appearance of black holes under the assumption of optically thin emission, discussing their main image features at two extreme geometry scenarios of accretion (i.e. spherical vs. thin disk accretion). This is followed by the classification of light trajectories based on the number of half-orbits turned around a black hole, while on their way to meet an observer's image plane. Next, we address the main properties of the photon ring and its observational significance, covering the dependence on the space-time geometry and on the accretion model's astrophysical assumptions. We conclude this section by presenting the derivation of the formula for the theoretical Lyapunov exponent − a quantity that measures the instability scale of nearly bound orbits − and by elaborating on its connection with relevant observable features of the photon ring.

Black hole space-times are unique in that an external observer will receive multiple images from the same light source: the direct image and an infinite number of distorted, demagnified, and even inverted, image copies [70]. Such a phenomenon is caused by the presence of multiple null geodesics connecting the source to the observer, some of which are able to orbit a BH several times. The latter come from the presence of a region of bound unstable orbits in the effective potentials seen by photons, allowing for strongly lensed trajectories that orbit the black hole n (half-)times [70]. In turn, the positions of these lensed images occupy a well-defined region in the observer's sky, converging near the critical curve [47]. For a BH that is seen against a starry background, the region near the outside of the critical curve (i.e. the shadow edge) contains an infinite set of lensed images of the entire Universe [70, 82]. If one considers an astrophysical setting of a BH surrounded by optically thin emission instead, the region near the critical curve presents a thin photon ring of enhanced brightness, whose appearance interpolates between two extreme scenarios [71]. On one end, the photon ring converges to a critical curve in the image plane of the observer, while the CBD entirely fills it (i.e. coinciding with the BH shadow) [31]. This arises, in particular, in accretion disks which have a spherically symmetric, infalling matter flows [83]. On the opposite end, the photon ring is decomposed into an infinite sequence of rings, superimposed on the direct emission around the CBD [47]. The latter scenario occurs not only in infinitesimally thin-disk equatorial, orbiting flows , but also as long as there are gaps in the emission region [47, 71]. In essence, the critical curve defines both the shadow and the photon ring, while the details of the surrounding emission affect the appearance of these features to an external observer. To formally define the photon ring, we proceed by characterizing the null geodesics in a BH space-time.

2.5.1 Photon Ring and the number of half-orbits

Throughout literature, researchers have proposed various frameworks to distinguish the directly observed features, from others that are seen due to extreme gravitational lensing (e.g. [47, 63, 70, 89, 138, 180]). One of the earliest classification schemes, based on the light bending angle, was proposed by Virbhadra and Ellis (2000) [138], with the terms *relativistic images* and *relativistic Einstein rings* being used to describe light trajectories with a bending angle $\alpha > 3\pi/2$ and $\alpha > 2\pi$, respectively. More recently, Gralla, Holz & Wald (2019) [47] adopted the terms *lensing ring* and *photon ring* in a framework that quantifies the photon trajectories by the fractional number of polar orbits completed around a black hole, which can be intuitively related to the number of times they cross its equatorial plane. For the sake of our work, we adopt the classification introduced by Johnson et al. 2020 [70], where null geodesics are organized according to the number of half-orbits they complete around a BH, prior to reaching an observer's screen. More precisely, null geodesics are categorized as follows:

- $(n = 0)$: *direct image* − corresponding to light rays that fail to complete a half-orbit around a BH;
- $(n \geq 1)$: *photon ring* − corresponding to light rays complete a half-orbit, or more, around a BH.

The photon ring can be divided into subrings, such that the n^{th} ring corresponds to light rays that complete n half-orbits. As an example, the backwards ray-traced equatorial plane null geodesics in a Schwarzschild space-time are illustrated in the left panel of Figure 2.3. In the right panel, we display the simulated appearance of a Schwarzschild BH surrounded by an optically thin accretion disk, as seen from a face-on orientation. The generation of such images is detailed throughout chapter 3. We note that equivalent images of the Kerr space-time, seen at different inclination angles, can be found in the following works: face-on [71, 179, 181]; edge-on [52]. Another illustrative example can be found in Figure 1 of [53].

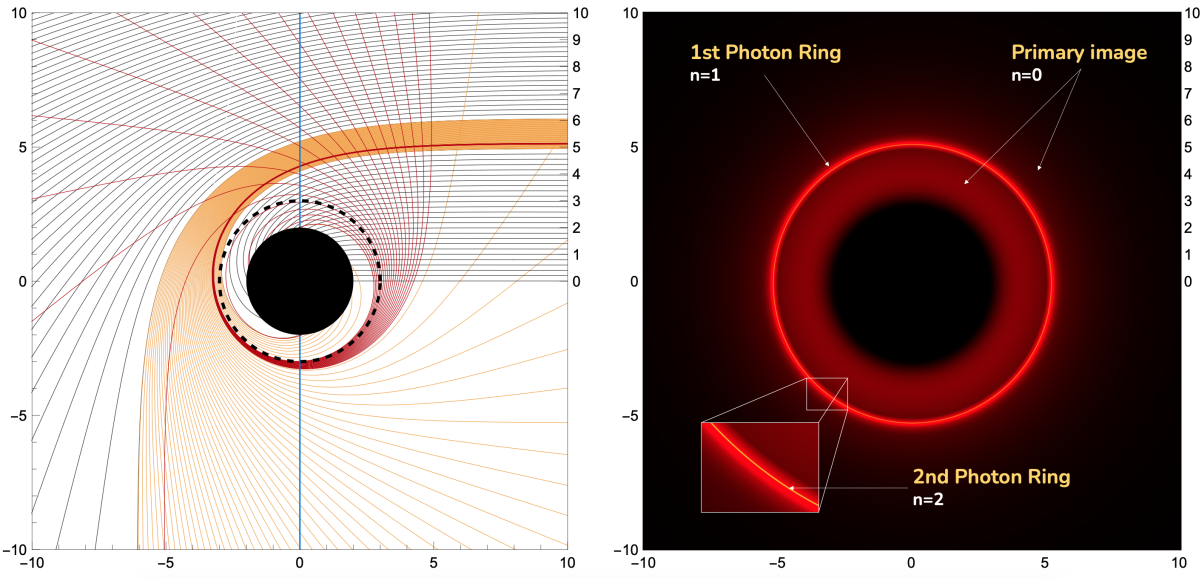

Figure 2.3: Left panel: Null geodesics in the Schwarzschild space-time as a function of impact parameter b, in distance units of BH mass M, for an inclination $i = 0^{\circ}$ (i.e. face-on). The left and bottom axis display the distance in units of M. The values in the right axis denote the impact parameter in the observer's sky, in units of M. The black circle represents the Schwarzschild BH event horizon at $r = 2M$. The dashed black circumference represents the photon sphere radius located at $r = 3M$. The vertical blue line depicts the BH equatorial plane. The photon trajectories are colored as follows: Black - direct image ($n = 0$); Gold - 1^{st} photon ring ($n = 1$); Red - 2^{nd} photon ring ($n = 2$). The spacing in impact parameter is $1/5$, $1/50$, and $1/500$, respectively. Right panel: Simulated visual appearance of a Schwarzschild BH surrounded by a thin accretion disk, as seen by an observer located at $r = 1000M$, at a face-on orientation. The accretion disk is modelled by the GLM2 semi-analytic profile (3.4), described in chapter 3.

As we shall discuss later in this section, this framework choice allows us to relate the number of half-orbits with the Lyapunov exponent of nearly bound orbits. For now, let us examine both panels of Figure 2.3 to better understand the photon ring. By inspection of the left panel, one can see that the impact parameter (i.e. the right side of the panel) of the geodesics corresponding to the $n = 1$ and $n = 2$ rings are confined to a specific range of values, all converging towards the critical impact parameter $b_c = 3\sqrt{3}M$. The effect is more pronounced for the $n = 2$ ring, and will be increasingly so for any higher order rings, where minute deviations from the critical impact parameter can lead to very distinct trajectories. This highlights how the location of the photon ring is sensitive to the gravitational lensing properties of the underlying geometry, particularly for higher order rings.

Suppose a BH is surrounded by an optically and geometrically thin equatorial accretion disk, extending all the way to the BH's event horizon. In addition, consider an observer looking at the BH at a face-on orientation. For this scenario, the direct image of the disk covers the largest area in the observer's sky. Inside the critical curve, emission is still visible due to the outwards emitted photons in the $2M < r < 3M$ region. Due to the proximity to the BH, this emission is significantly gravitationally redshifted, manifesting as gradual decrease in brightness [89]. This phenomenon occurs due to the gravitational time dilation, affecting the frequency of photons as they travel away from the BH. At the image centre, a CBD appears with a smaller size than the critical curve, but larger than the BH event horizon; a phenomenon caused by the geodesics that do not intersect the equatorial plane, leading to a lensed apparent image of the event horizon (i.e. dubbed as *inner shadow* [89]). Focusing on the photon ring, the region in the observer's sky occupied by the $n = 1$ ring projects a distorted and demagnified image of the backside of the accretion disk, that overlaps with the direct image of the front side of the disk. This appears as a brighter, thinner ring. As one approaches the critical curve, additional images of the front (back) sides of the disk are seen, for rings with an even (odd) number of half-orbits. The $n = 2$ ring appears in the previous Figure as significantly thinner and brighter ring. For a BH surrounded by a uniform spherically symmetric inflow, the individual contributions of each (sub)ring become indiscernible [38, 83], but they are still present, as a brightness increase is still perceived by an external observer.

Thus, we take the *photon ring* to be defined as the infinite collection of densely packed rings, that are a projection of photon trajectories that complete more than a half-orbit around a black hole, while on their way to an observer [48, 70, 71, 182]. We note that the definition provided here encompasses both the *lensing ring* and *photon ring*, as described by Gralla et al. (2019) [47]. While this change in terminology has only slight implications for the photon ring's position, its significance is relevant when discussing, for example, the individual contribution to the total brightness of the image [87].

2.5.2 The nature of the Photon Ring

The null geodesics and the gravitational lensing responsible for the photon ring are an intrinsic property of the underlying space-time curvature. However, the lensed images it shows belong to an emission source located somewhere outside the BH. Hence, they are strongly connected with the optical, geometrical, and emission properties of the light source. For an accretion disk these can be the geometrical thickness, radius, emission profile, absorption, and other features astrophysical flow (e.g. magnetization, turbulence) [47]. As higher-order rings are considered, these dependencies fade-out, being overcome by the strong gravitational lensing [51, 86]. For example, even if there is no emission located near the event horizon, or the photon sphere, the photon ring would still show images arising from lensing of emission elsewhere [47]. Having presented how we categorize light trajectories, we now seek to explore the nature of the photon ring, focusing some of its key properties.

The light trajectories that comprise the photon ring can orbit repeatedly through the emission region near a BH. Not only are the paths of these trajectories increasingly bent, the more they approach the photon sphere, but also their length is increased, proportionately to the number of half-orbits [47, 83]. This last aspect is fundamentally linked with the enhanced brightness of the photon ring. According to the principles of radiative transfer, for a purely optically thin emission (i.e. neglecting absorption features) the brightness increases with the optical path length [183]. It follows that, due to the increased path length, every light trajectory will have its luminosity boosted by picking additional photons from the emission region, on its winding around the BH [27, 83]. This brightness can grow arbitrarily large for trajectories that orbit $n \to \infty$ times around a BH. However, this behaviour is exponentially suppressed [27, 47], and therefore higher order rings provide a marginal boost to the total luminosity, comparatively to the first and second photon rings.

In addition to the brightness increase, several other properties of the photon rings are subject to the aforementioned exponential decay, including the location, impact parameter, demagnification, and even the flux ratio between two successive rings [50, 53]. It turns out that the higher the ring order, the stronger the dependence on the gravitational lensing properties (i.e. smaller the dependence on the emission properties), such that in the limit $n \to \infty$ the photon ring is a generic feature of the underlying geometry, regardless of the emission properties [70, 86, 182]. This is happens because, as each lensed image is exponentially distorted and demagnified, the details of the emission are exponentially harder to resolve. Thus, the photon ring offers a way out of the "contamination" enacted by the disk.

When factoring in non-spherical emission region, the shape of the photon ring is also influenced by the observer's inclination angle and BH rotation [48, 50, 52, 82]. For a non-rotating BH, seen at a face-on angle, the shape of the photon ring is circular. As the observer's inclination angle changes towards an edge-on orientation, this shape becomes gradually deformed, remaining symmetrical along the equatorial plane axis, though effect is significantly more pronounced for the $n = 1$ ring. Higher-order rings occupy exponentially narrower lensing bands (that asymptote towards the circular critical curve), where this deformation is much less noticeable. The symmetry in this deformation is broken when a rotating BH geometry is considered, growing closer (farther) to the BH as the space-time rotates away from (towards the) an external observer; an effect that occurs due the gravitational frame dragging imposed by the BH spin. The latter, in combination with the Doppler effect, causes in an asymmetrical brightness as well.

The existence of an unstable photon sphere is crucial for the photon ring, as much as it is for the BH shadow. As mentioned in section 2.4, every spherically symmetric BH geometry contains an unstable photon sphere. Under optically thin emission conditions, the visual appearance of a spherically symmetric BH will always include have a photon ring. The existence of non-Schwarzschild geometries possessing unstable photon spheres implies the photon ring is not an exclusive feature of black holes. Furthermore, some configurations without event horizons (i.e. wormholes, naked singularities) may produce multiple photon rings. Such an effect is present due to light rays that travel above (but near) the critical curve, and are reflected back to an observer due to the presence of additional local maxima in the effective potential seen by photons or an infinite potential slope [148, 153, 184]. As gravitational lensing properties differ according to the underlying geometry, the location and (in)stability of the photon sphere, and by extension, the photon ring morphology (i.e. location, width, luminosity), is sensitive to deviations from Kerr(Schwarzschild)-ness.

2.5.3 Lyapunov exponents

As discussed in section 2.3, the motion of photons is dictated by the shape of the effective potential (2.14) and (2.34), with bound orbits being located at critical points of the potential. The curvature at these points is indicative of the bound orbit (in)stability which, for unstable orbits, can be understood through the lens of the Lyapunov exponents [140]. The latter are theoretical quantities which encode the instability scale of nearly bound orbits [52, 70, 90, 185], by tracking the separation between two neighbouring orbits [185]. In the context of BH images, they are central towards the characterization of photon spheres, being linked with observable quantities (e.g. photon ring relative widths, relative luminosities, demagnification), and therefore sensitive to the space-time geometry [48, 51, 70, 186, 187].

Thus, the characterization of the photon ring starts with unstable nearly bound orbits which hover very close to the photon sphere. In what follows, we present the derivation of the theoretical Lyapunov exponent γ of nearly bound equatorial plane orbits, for a generic static and spherically symmetric space-time. Afterwards, we examine the relation between this exponent and the relative flux between successive photon rings. We begin by studying the effect of a small radial perturbation δr near the photon sphere, $r = r_{ps} + \delta r$, with $\delta r \ll r_{ps}$ [188]. In order to apply this perturbation to our geodesic equation of motion, we perform a Taylor series expansion of the effective potential $V_{eff}(r)$ about r_{ps}, up to the second order

$$V_{eff}(r) \simeq V_{eff}(r_{ps}) + V'_{eff}(r_{ps})\delta r + \frac{1}{2!}V''_{eff}(r_{ps})(\delta r)^2 \,, \tag{2.52}$$

which can be simplified with (2.36) to

$$V_{eff}(r) \simeq \frac{1}{b_c^2} + \frac{1}{2!}V''_{eff}(r_{ps})(\delta r)^2 \,, \tag{2.53}$$

where the double prime $''$ denotes the second derivative with respect to the radial coordinate r. Continuing the derivation, a small perturbation near the photon sphere radius is applied to the geodesic equation of motion (2.13), factoring in the previous result to write

$$AB\left(\frac{d\delta r}{d\lambda}\right)^2 = L^2\left(-\frac{1}{2}V''_{eff}(r_{ps})(\delta r)^2\right). \tag{2.54}$$

Here, we have once again re-introduced an L^2 factor (previously absorbed into the affine parameter). During this transition, the term in the equation of motion (2.13) containing the impact parameter cancels out with its reciprocate from equation (2.53), as $b^{-2} \sim b_c^{-2}$ close to the photon sphere. Using the angular momentum conservation (2.9), the perturbed equation of motion is re-written as

$$\left(\frac{d\delta r}{d\phi}\right)^2 = -\frac{1}{2}\frac{C^2}{AB}V''_{eff}(r_{ps})(\delta r)^2. \tag{2.55}$$

For a moment, let us focus on effective potential. Computing its second derivative with respect to r and substituting (2.14) returns

$$V''_{eff}(r_{ps}) = -2\frac{A'C'}{C^2} + 2\frac{A(C')^2}{C^3} + \frac{A''}{C} - \frac{AC''}{C^2}, \tag{2.56}$$

where the argument of the generic functions (evaluated at $r = r_{ps}$) has been omitted. This expression

may be simplified through equation (2.37), by substituting $A'(r_{ps})$, to obtain

$$V''_{eff}(r_{ps}) = \frac{1}{C^2}(A''C - AC''), \tag{2.57}$$

leading to equation (2.55) in the form

$$\left(\frac{d\delta r}{d\phi}\right)^2 = \left(\frac{1}{2}\frac{AC'' - A''C}{AB}\right)(\delta r)^2 \, . \tag{2.58}$$

We proceed by squaring both sides of the above expression, which results in the following equation of motion

$$\pi\frac{d\delta r}{d\phi} = \gamma\,\delta r \, , \tag{2.59}$$

where

$$\gamma = \pi\left(\frac{1}{2}\frac{AC'' - A''C}{AB}\right)^{\frac{1}{2}} \, , \tag{2.60}$$

denotes the Lyapunov exponent γ[7]. Note that only the positive branch of the square was kept, as the instability scale is quantified by a positive Lyapunov exponent [185] (i.e. a negative Lyapunov exponent characterizes a decreasingly small deviation from a bound orbit). Additionally, a factor of π was multiplied on both sides of the differential equation, enabling the relation between the Lyapunov exponent and the number of half orbits n. Equation (2.59) can be interpreted as an equation of motion in the proximity of the photon sphere [189]. Such an equation admits exponential solutions [70]

$$\delta r_n = e^{\gamma n}\delta r_0 \, , \tag{2.61}$$

describing the exponential growth in separation after n half-orbits δr_n, by an exponential factor γn, where δr_0 is an initial perturbation.

Equation (2.60) illustrates how the Lyapunov exponent γ is determined by the properties of the spacetime geometry. Specifically, this quantity depends on the local curvature (i.e. at the photon sphere radius) [90, 188, 189]. For the Schwarzschild BH, for example, substituting the appropriate generic functions in equation (2.60) yields a Lyapunov exponent of $\gamma = \pi$, which is in agreement with previous literature [27, 47].Conversely, equation (2.61) exposes the contribution of γ in the growth of an initial small perturbation. Notably, smaller (larger) values of γ translate into lesser (greater) separation per half-orbit following an initial perturbation. Such behavior depends on the photon sphere instability, which is related to the curvature of the effective potential at critical maxima: the wider (narrower) curvature of the peak reflects a smaller (larger) value of γ.

The Lyapunov exponent governs the demagnification and the relative intensity flux (i.e. which we will also refer as "luminosity extinction ratio") among successive images of the disk [52, 70]. For this work, we are interested in the latter, which, neglecting any source variations on the typical timescale of a photon orbit around a BH, is expressed as [70]

$$\frac{I_{n+1}}{I_n} \sim e^{-\gamma} \qquad \text{for} \qquad n \gg 1 \, . \tag{2.62}$$

The previous equation conveys the theoretical ratio between the $n+1$ and n rings' net contribution

[7] Once more, a similar expression is obtained for the Lyapunov exponent of an asymptotically flat, NED supported SSS, by replacing $A \to A/h$, $B \to B/h$ and $C \to C/H$, where the key difference originates in the non-linear contributions of the $H(r)$ and $h(r)$ functions.

to the total observed luminosity, which decays exponentially. We recall that with each half-orbit the brightness increases. However, because the width becomes exponentially smaller, the total contribution to brightness is equivalently smaller. For example, for a Schwarzschild BH, this quantity is a factor of $e^{-\pi} \approx 4\%$, indicating the net contribution to the total luminosity by each subring is approximately only 4% greater than the previous one.

It turns out that such a number is an universal quantifier of a given geometry in the limit $n \to \infty$, in which it loses its entire dependence on the accretion disk modelling [51, 86]. The exponential suppression of the subrings renders the observations of $n \to \infty$ unfeasible [86], but despite this, their sharp features fade slowly in the Fourier domain and, as a consequence, they tend to dominate the interferometric signal in very high frequencies [52, 70, 71, 82]. The most promising targets in this sense are the $n = 1$ and $n = 2$ ring [86]. While their detection hinges on observational capabilities that surpass those currently available, either because they require observations at higher frequencies or longer baselines, these are expected to be achievable with the next generation EHT (ngEHT) observations and through space-based interferometry. In this regard, the observational prospects have been recently reviewed in the literature (e.g. [52, 70, 71, 82, 179]). In particular, one expects significant deviations in the shape, diameter, width, and relative luminosity of the n = 2 ring (and of the n = 1 one to a lesser extent) for alternative (non-Kerr) geometries [51, 86, 179], so precise observations of this ring could be potentially used to constrain them.

As will be discussed in the next chapter, we shall approximate the Lyapunov exponent by the inverse I_1/I_2 extinction ratio, taking advantage of the fact that the sequence of subrings quickly approximates the critical curve (i.e. the latter corresponding to the limit $n \to \infty$), and compare it to the theoretically predicted value for a number of alternative, spherically symmetric geometries. We choose to focus the $n = 2$ ring as it offers a good compromise between having a sufficiently weak dependence on the assumptions of the accretion disk and being a prospective observation candidate with future VLBI campaigns. In this regard, we note that equation (2.62) is a theoretical expectancy based on the assumption that every photon trajectory will cross emission regions with similar properties [70]. This is true at larger values of n, since the photons will travel through essentially the same orbits. At lower values of n, the deviations from the unstable bound orbits become sufficient that photons are no longer expected to encounter the same matter distribution in the accretion disk near a BH, which can introduce differences in the actual luminosities of the lower order subrings. Nonetheless, one would still expect deviations between the actual intensity fluxes and the corresponding theoretical prediction to be captured by the choice of disk model.

Chapter 3

Methodology

This chapter presents the methodology that is used in this work to study the appearance of several BH space-times, when surrounded by an equatorial, infinitesimally thin accretion disk. It begins by detailing how the accretion disk emission is simulated, presenting the semi-analytic models proposed by Gralla-Lupsasca-Marrone and elaborating on their advantages and limitations. The following section describes the ray-tracing technique that drives our simulations and the steps required to produce the images of spherically symmetric black holes surrounded by an optically and geometrically thin accretion disk. We conclude by presenting the 16 alternate spherically symmetric space-times that are examined in this work, providing a brief overview of each geometry and reporting the parameter space constraints for which their corresponding shadow radius remains compatible with Sgr A*'s shadow size, as inferred by the EHT collaboration.

3.1 The GLM emission profiles

Proper modelling of the accretion flow is a mandatory step towards simulating the near-horizon appearance of an accreting BH. This can be achieved via semi-analytic models or through time-dependant General Relativistic MagnetoHydroDynamics (GRMHD) simulations (note: see [169] and references therein). The latter are typically preferred over the former, for their ability to reproduce the highly dynamic and energetic environment that is expected from the accretion flow around a BH. Unfortunately, the astrophysical properties of the hot plasma comprising the accretion disk around a supermassive compact object have yet to be fully understood. GRMHD simulations still require several prior assumptions concerning the particles' velocities and temperature, the opacity and geometrical shape of the disk, its magnetic properties, its spin orientation, the tilt in reference to the BH equatorial plane, as well as the BH's mass, distance, and spin [169]. Moreover, these simulations are incredibly taxing on computer systems, requiring substantial amounts of time and processing power to fully conduct. On the other hand, semi-analytic models are capable of approximating the most influential features of the accretion disk that contribute to the BH image, encapsulating the main outputs of GRMHD simulations into a more simplified model [82]. Indeed, we recognize that such models lack the detailed representation that GRMHD models can achieve, and in this way do not represent the astrophysical conditions around accreting black holes as accurately. Nonetheless, their use has proved fruitful in the study of photon rings and their properties (e.g. [47, 52, 71, 179]. In the context of BH imaging, resorting to semi-analytic models provides a more straightforward alternative to GRMHD simulations, by eliminating the need to simulate complex accretion flow astrophysics and simplifying the analytical and numerical treatment of the photon ring features of the image, allowing a more efficient comparison of different BH geometries [82].

3.1 The GLM emission profiles

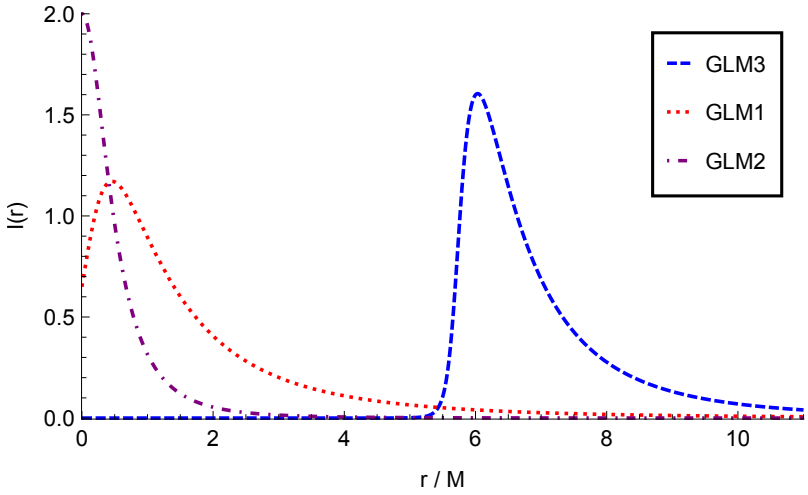

Figure 3.1: The GLM intensity profiles described by Equation (3.1). The GLM3 (blue, dashed line), GLM1 (red, dotted line), and GLM2 (purple, dot-dashed line) profiles correspond to the γ, μ and σ parameter choices indicated in (3.2), (3.3) and (3.4), respectively. The radius is expressed in units of BH mass M.

For these reasons, we focus on the Gralla-Lupsasca-Marrone (GLM) models [82], which are based on the Standard Unbound (SU) Johnson distribution. There are radially dependent emission profiles that are framed as

$$I(r;\gamma,\mu,\sigma) = \frac{\exp\left(-\frac{1}{2}(\gamma+\operatorname{arcsinh}(\frac{r-\mu}{\sigma})^2\right)}{\sqrt{(r-\mu)^2+\sigma^2}}, \tag{3.1}$$

where γ, μ and σ are three freely-adjustable parameters which modify the features of the disk's intensity: γ alters the skewness of the distribution (i.e. controlling the rate of growth of the disk's intensity, from asymptotic infinity to the peak); μ dislocates the distribution's peak horizontally (i.e. controlling the radial location disk's emission); σ modifies the distribution's kurtosis (i.e. controlling the emission profile's dilation). By exploring a range of parameters of such emission profiles one can mimic the results of certain scenarios for the accretion flow within GRMHD simulations [52, 71, 179]. For the sake of this work we shall suitably adapt to the non-rotating case the three original models included in [82], which correspond to the following choices:

$$\text{GLM3} \quad : \quad \gamma = -2\,, \quad \mu = \frac{17M}{3}\,, \quad \sigma = \frac{M}{4}\,, \tag{3.2}$$

$$\text{GLM1} \quad : \quad \gamma = -\frac{3}{2}\,, \quad \mu = 0\,, \quad \sigma = \frac{M}{2}\,, \tag{3.3}$$

$$\text{GLM2} \quad : \quad \gamma = 0\,, \quad \mu = 0\,, \quad \sigma = \frac{M}{2}\,. \tag{3.4}$$

These profiles are taken as semi-analytic models consistent with a stationary, axisymmetric, absorption free (i.e. optically thin), geometrically thin disk. Observing Figure 3.1, we see each of the three emission profiles described by the above-mentioned parameter choices: GLM3 has a peak brightness located close the corresponding innermost stable circular orbit (ISCO) of a Schwarzschild BH (i.e. $r \gtrsim 6M$), while the emission in GLM1/GLM2 extends all the way to $r = 0$, with distinct shapes. The latter two models are more suited to describe the overflow of the plasma in orbit around M87* and Sgr A*. Note that the BH horizon will appear well before the peak brightness in these two profiles. As such, they represent two cases of emission down to the event horizon, with differing outwards brightness

decays. In such instances, the inner edge of the direct emission of the disk in such cases will be much smaller than the one of the $n = 1$ and $n = 2$ rings. Consequently, the latter's emission will appear stacked on top of the direct emission of the disk, complicating their direct visualization. Hence the choice of the GLM3 emission profile, since the inner edge of the direct emission is truncated at a larger distance than the corresponding edge of the photon rings, allowing us to disentangle the contribution of each image feature.

3.2 Ray-tracing black hole images

The visual appearance of a BH can be simulated via backwards ray-tracing of the photon trajectories, from the observer back into their point of emission. Essentially, this is achieved in two main steps: (1) computing the trajectories of photons by solving the equations of motion of null geodesics for a given space-time geometry; (2) integrating the radiative transfer equation along the computed photon trajectories. This procedure has been employed in past literature to great extent (e.g. [47, 58, 64, 66, 135, 148, 190–192]) to study the images of black holes in various astrophysical settings.

In order to perform our own simulations and generate images of spherically symmetric space-times surrounded by a thin accretion disk we use our own the Geodesic RAys and Visualization of IntensiTY profiles (GRAVITYp) ray-tracing code. This code is designed to ray-trace null geodesics in spherical coordinates, with increased precision around the critical curve. The latter adaptation follows from the higher sensitivity of photon trajectories to small deviations in the impact parameter near the critical curve. Since we are interested in studying properties of the photon rings, this code is a suitable and efficient tool for use in our work. In addition, its application in previous works (e.g. [58, 63, 148]), particularly in [67] where its outputs were validated against another ray-tracing code (i.e. GYOTO), vouch for its reliability.

3.2.1 Computing null geodesics

We first input the metric associated with a chosen spherically symmetric space-time. By using equations (2.36), one obtains the horizon radius, photon sphere radius and critical curve radius, respectively. The horizon radius is taken as the ray-tracing endpoint. The geodesics are computed for a chosen observer radial distance and chosen impact parameter range. In our case, all images were produced for a distant observer ($r = 1000M$). The mass parameter M may be specified but we opted to obtain all the relevant quantities in units of M (i.e. by setting $M = 1$ in all simulations). This choice not only generalizes the problem to be independent of the BH mass, but also aids the computation, restricting it to values of smaller orders of magnitude than the ones BH masses are associated with. The studied impact parameter space lies at $0 \leq b/M \leq 10$ in the observer's sky, since we are interested in near-horizon phenomena.

By solving equation (2.19) (or (2.35) for geometries threaded by NED models) numerically, we obtain the null geodesics for any choice of spherically symmetric space time. An example of the photon trajectories embedded in a Schwarzschild space-time is provided in Figure 2.3. Since we're interested in studying BH space-times surrounded by an equatorial infinitesimally thin accretion disk, we also track the radial coordinate at which geodesics intersect the equatorial plane of the BH (i.e. represented by the vertical blue line in Figure 2.3) along with the corresponding impact parameter. The output of this operation is a list of impact parameter values and the radial coordinates that correspond to a photon crossing the equatorial plane of a BH up to three times, which gives the transfer function between r and b, as depicted in Figure 3.2. This step, which permits the distinction between photon trajectories corresponding to the direct image, the 1^{st}, and the 2^{nd} photon rings, is essential for computing the observed intensity.

3.2 Ray-tracing black hole images

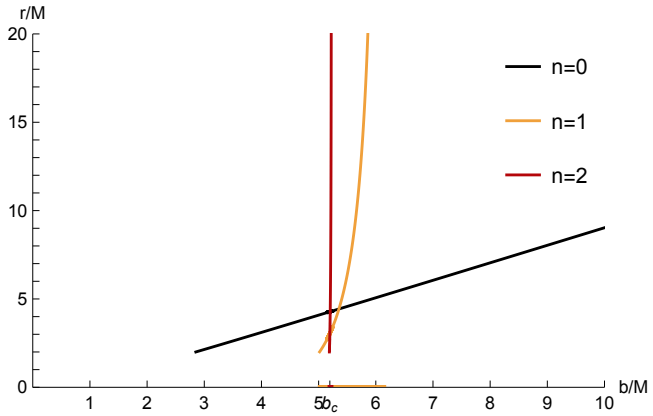

Figure 3.2: Transfer functions $r_n(b), n \in \{0,1,2\}$ for the null geodesics in a Schwarzschild space-time that complete 0, 1, and 2 half-orbits around the BH (see corresponding discussion in section 2.5). Both the radial coordinate and the impact parameter are represented in units of BH mass M. The photon trajectories are colored as follows: Black - direct image ($n = 0$); Gold - 1^{st} photon ring ($n = 1$); Red - 2^{nd} photon ring ($n = 2$). The gold and red lines over the horizontal axis indicate the range of impact parameter values where photon rings may appear, depending on the model of equatorial and infinitesimally thin emission.

Figures 2.3 and 3.2 hint at what is seen in an observer's sky. Notably, they highlight how the photon rings will only appear inside a specific impact parameter range of values. Whether they actually fill this entire range or not depends on the emission model that is considered. For example, focusing on the GLM3 model, we can use these figures to understand the emission from the different photon rings is disentangled from the direct emission. By tracing the geodesics which intersect the BH equatorial plane at the radii $r \gtrsim 6M$ (i.e. the radius at which the accretion disk profile is truncated), it is possible to see that only specific sets of geodesics intersect the equatorial plane. Despite this, the impact parameter for these trajectories will not overlap, as it will vary according to the number of orbits completed around the BH. Figure 3.2 also reveals this behaviour, where one can see that for $r \gtrsim 6M$ the corresponding impact parameter of each transfer function is distinct. Note that such figure represents the geodesics around a Schwarzschild BH but the reasoning applicable to every alternate geometry.

Tracking the radial coordinate when nearly bound geodesics intersect with the equatorial plane allows the theoretical Lyapunov exponent γ to be computed. Starting from equation (2.61), we apply the natural logarithm to both sides of the equation and isolate γ. This allows γ to be approximated by the number of half-orbits of a nearly bound geodesic via [70]

$$\gamma \approx \frac{1}{n} \ln \left| \frac{\delta r_n}{\delta r_0} \right| . \tag{3.5}$$

Next, we take the aforementioned radial coordinates as the deviation from the critical curve after n half-orbits r_n, computing the theoretical γ as

$$\gamma = \ln \left| \frac{r_n - r_{ps}}{r_{n+1} - r_{ps}} \right| . \tag{3.6}$$

Note that, by considering the separation between two subsequent photon rings, a photon trajectory completes one half-orbit, leading to the disappearance of the $1/n$ factor. We compute γ between the $n = 1$ and $n = 2$ photon rings, for a geodesic of impact parameter $b = b_c + 1 \times 10^{-15}$. For a Schwarzschild BH, this yields a value of $\gamma \approx 3.151$. Such value which deviates from the exact value $\gamma = \pi$ (for $n \to \infty$) by an error of $\sim 0.3\%$, far below other observational uncertainties in this problem. Combining this equation with (2.62) we obtain the theoretically predicted extinction rate between the $n = 1$ and $n = 2$ rings.

3.2.2 Computing the observed intensity

To produce an image of BH we seek the intensity in the observer's frame. This is obtained by integration of the radiative transfer equation along the path of a photon, from its point of emission to the point when it reaches the observer. The problem of radiative transfer is complex and requires accounting for various properties of the emission and particle dynamics inherent to GRMHD simulations. However, using the semi-analytical approach, this step becomes much simpler.

As mentioned section 3.1, we assume that the compact geometries are surrounded by an infinitesimally thin accretion disk. To model this emission, we begin by considering the radiative transfer along a photon trajectory. We neglect any scattering between the photons and the hot plasma of the accretion disk and assume that there are no light sources between the accretion flow and the observer. In this scenario, the Lorentz-invariant form of the radiative transfer (Boltzmann) equation is expressed as [83, 183]:

$$\frac{d}{d\lambda}\left(\frac{I_\nu}{\nu^3}\right) = \frac{j_\nu}{\nu^2} - (\nu\alpha_\nu)\left(\frac{I_\nu}{\nu^3}\right), \tag{3.7}$$

where λ denotes the affine parameter used to parameterize the photon trajectory along a space-time interval, and I_ν, j_ν and α_ν correspond, respectively, to the specific intensity, emissivity and absorption at a given frequency. In order to observe photon rings, the disk emission must be transparent to its own radiation (i.e. optically thin). Since accretion disks possess complex emission profiles that are not expected to be optically thin at all frequencies, we assume (for simplicity's sake) an emission coefficient $j_\nu \sim \nu^2$, so that the Lorentz-invariant emission coefficient j_ν/ν^2 becomes frequency independent, as well as an optically thin emission (i.e. $\alpha_\nu = 0$). Plugging these conditions into equation (3.7), implies that I_ν/ν^3 is conserved along a ray of light. Under the previous assumptions, the radiative transfer towards an observer is governed by two factors [64]:

1. the radiation will suffer gravitational redshift as it moves away from the BH;
2. the photon ring trajectories will contribute with additional brightness as they intersect the accretion disk multiple times.

In the absence of absorption, and of a source between the observer and the emitter, the effect of the gravitational redshift can be computed according to Liouville's theorem [93, 193], which demands the conservation of the flux between the photon trajectory

$$\frac{I_{\nu_o}}{\nu_o^3} = \frac{I_{\nu_e}}{\nu_e^3}, \tag{3.8}$$

where ν_o and ν_e refer to the frequency in the observer's and emitter's frames, respectively. We can re-arrange the terms in the equation (3.8) and employ the redshift factor definition $g = \nu_o/\nu_e$ [194] to obtain

$$I_{\nu_o} = g^3 I_{\nu_e}, \tag{3.9}$$

which lays the foundation that allows us to obtain the intensity I_{ob} that is seen in the observer's screen. We start by integrating the specific observed intensity I_{ν_o} over all frequencies, and use equation (3.9) together with a change the integration variable via $d\nu_o = g d\nu_e$, which returns

$$I_{ob} = \int d\nu_o I_{\nu_o} = \int d\nu_e g^4 I_{\nu_e}. \tag{3.10}$$

Recalling our previous assumptions, we establish an equivalence between the emission in the disk's reference frame and the radial intensity profiles $I(r)$ presented in section 3.1, such that when integrating the specific emitted intensity over all frequencies we have $I_{em} = \int d\nu_e I_{\nu_e} = I(r)$. Applying this to equation (3.10) we get

$$I_{ob} = \int d\nu_o I_{\nu_o} = \int d\nu_e g^4 I_{\nu_e} = g^4 I(r), \tag{3.11}$$

indicating that the integrated intensity scales with g^4. For spherically symmetric space-times, we relate the redshift factor with the $A(r)$ metric function through $g = \sqrt{A(r)/A(r_\infty)}$ [5, 93]. Inserting this into equation (3.11) yields

$$I_{ob} = \left(\frac{A(r)}{A(r_\infty)}\right)^2 I(r). \tag{3.12}$$

In the case of an asymptotically-flat space-time[1] (i.e. $A(r_\infty) \to 1$) Equation (3.12) is simplified into

$$I_{ob} = A^2(r) I(r). \tag{3.13}$$

Finally, it is necessary to account the additional contribution to the intensity that takes place due to photons intersecting the accretion disk n times. For an infinitesimally thin disk, this is represented by a sum of each individual contribution

$$I_{ob}(r) = \sum_{n=0}^{2} A^2(r) I(r)\big|_{r=r_n} \ , \tag{3.14}$$

which is the equation that is used in our simulations to produce images of spherically symmetric space-times surrounded by accretion disks as described by the GLM models. Here, r_n represents the radial coordinate of the n^{th} intersection with the accretion disk plane, outside the horizon. It is through these equations that we calculate the observed extinction rate $I_{\frac{n=1}{n=2}}$, between the 1^{st} and 2^{nd} sub-rings, which appears in Table 4.1. Note that when dealing with spherically symmetric space-times supporting effective geodesics, we multiply factor of $H^2(r)$ to equation (3.14). In doing so, we are neglecting absorption and other potential transport effects emerging from the non-linearities in the electromagnetic Lagrangian.

3.3 Choice of spherically symmetric space-times

In this work we consider a total of 16 alternative spherically symmetric space-times that are selected from Vea [81], spanning a wide range of gravity theories and fundamental physics scenarios. In doing so, we follow a theory theory-agnostic approach, disregarding any potential drawbacks in the theories and approaches leading to the selected geometries (e.g. violation of energy conditions, instabilities that render the space-time geometries non-viable). We take this stance since, for the sake of this work, we are only interested in comparing their cast images. However, there is one aspect related to a particular class of the considered space-times that we make an effort to include in our discussion: the photon trajectories within NED supported space-times. Since in such circumstances, photons travel through effective geodesics rather than the background geometry, the resulting image in the observer's sky is distinct from the image that result from considering only the background geometry. To what extent such image is different depends on how strongly the effective geometry deviates from the background one. Thus, we shall not forego the fact that three of the geometries considered here have been identified to be

[1] Note that equation (3.12) indicates that the observed intensity is distance dependent in non-asymptotically flat space-times, and the contribution of the term $A(r_\infty)$ must be taken into account if $A(r)|_{r=r_o} \neq 1$.

derived from reasonable enough NED theories, and will proceed with their analysis under the scope of effective geometries.

In our approach, we probe each model's parameter space as far as possible, where the corresponding BH shadow remains compatible with Sgr A*'s shadow bounds. This yields the parameter value which that is utilized for the posterior generation of BH images. We note that, for the sake of this work and to enhance any potential differences in their cast images, we shall take as our reference value the 2σ bound, presented in equation (2.51), to constrain the parameter space of each geometry. In this regard, we aim to obtain more precise to each geometry's viable parameter space to more finely match the shadow's size limits, refining those already obtained by Vagnozzi et al. [81]. This is done because, at such large deviations from the Schwarzschild's prediction, the features of the photon rings become more sensitive to small modifications in the model's parameters. Note that this approach is not sufficient to constrain all of the considered models [81]. In some instances, the model's parameter space allowing an event horizon is smaller than the constraints imposed by the EHT bounds. In other words, the parameter space is limited by the geometry itself, rather than the EHT bounds (e.g. Bardeen BH). Alternatively, there are cases where no limits are imposed to parameter space within the EHT bounds (e.g. Simpson-Visser black bounce). Furthermore, there are cases in which we find the EHT constraints to a model's parameter space are not as strong as those from other sources (i.e. Sen BH). In summary, not all geometries are constrained in the same fashion.

In the following subsection, we briefly present each of the chosen space-times. Please note that this subsection is not meant to fully describe each geometry, as such a feat could merit a whole chapter for each case. Instead, it is meant to briefly describe the type of geometry they represent, the functional form which is used in our generation of BH images, and the associated parameter constrain obtained via shadow size compatibility with the EHT observations. In testing the following alternative geometries, we restrict our analysis to a single free parameter (excluding to the mass M), specifying when other parameters are fixed. Additionally, we note that the generic functions of most geometries obey $A(r) = B^{-1}(r)$ and $C(r) = r^2$, unless otherwise stated. To compare the alternative space-times considered in this work, we begin our considerations from the canonical spherically symmetric BH - the Schwarzschild black hole. This BH represents a non-rotating, asymptotically flat, neutrally charged space-time, containing a single free parameter in the mass M. This geometry predicts the existence of an event horizon located at $r_h = 2M$, a photon sphere located at $r_{ps} = 3M$, and a critical impact parameter at $b_c = 3\sqrt{3}M$. The latter is compatible with the EHT's inferred shadow radius for Sgr A* within 1σ [80]. In this way, this space-time geometry is taken as the benchmark against which every other metric is tested.

3.3.1 Geometries and parameter constraints

1. Reissner-Nordström (RN) BH.

Our choice of alternative geometries begins with the simplest charged solution of the Einstein field equations, which follows as a natural extension of the Schwarzschild BH by incorporating an electrical charge term[2]. Its functional form is written as [195, 196]

$$A(r) = 1 - \frac{2M}{r} + \frac{q_e^2}{r^2}\,, \tag{3.15}$$

where q_e denotes the electrical charge. Through this modification, the Reissner-Nordström BH describes

[2] A magnetically charged solution, as well as a dyonic RN solution, have been identified in BH literature but are left out of this work. The reason we choose the original RN metric lies in its historical relevance, being the first charged and second spherically symmetric solution of Einstein's field equations.

a non-rotating, asymptotically flat, electrically charged vacuum which, according to BH uniqueness theorems, is the only space-time geometry to do so [197]. The inclusion of the q_e term has a profound effect in the space-time geometry. Its value not only determines the locations of r_h, r_{ps} and b_c, but also dictates if an event horizon is present in the first place. Notably, to describe a BH, q_e must verify the condition $0 \leq q_e^2 \leq M^2$. Should this value be exceeded, this space-time represents a naked singularity instead. To remain compatible with the EHT observations, the charge parameter must be contained within the previous range. Taking the 2σ bounds as a reference (i.e. see equation (2.51)), we find that the lower bound for the shadow size is saturated when $q_e = 0.939M$. This value is slightly lower than the previous constraint by Vea, of $q_e = 0.95M$.

2. Euler-Heisenberg (EH) NED BH

This next geometry is the first example of a NED supported geometry that we include in our work. This particular example emerges within the context of the Euler-Heisenberg NED theory, when coupling GR to Euler-Heisenberg NED via the following Lagrangian [198]

$$\mathcal{L}(F,G) = F + \mu\left(4F^2 + 7G^2\right), \tag{3.16}$$

where, F and G are defined through (2.21), and μ is a coupling constant that appears in the Euler-Heisenberg theory's non-linear correction terms [131, 198]. Focusing on purely magnetic configurations, the corresponding spherically symmetric background geometry is characterized by the function[114]

$$A(r) = 1 - \frac{2M}{r} + \frac{q_m^2}{r^2} - \frac{2\mu q_m^4}{5r^6}, \tag{3.17}$$

which describes a static, magnetically charged BH, supported by a magnetic monopole q_m, and can be viewed as a magnetically charged RN BH when $\mu \to 0$. However, unlike the RN BH, there are no theoretical restrictions to the value of q_m in describing a BH, when $\mu \neq 0$ [81]. In order to constrain q_m via the shadow radius, Vea fix the coupling constant to $\mu = 0.3$, on grounds of this value to approximately correspond to the largest coupling in which the EH theory's perturbative approach remains relevant. This choice is also motivated by the 2σ bounds being insufficient to properly constrain the value of μ, since the shadow radius depends much less on the coupling constant, comparatively to q_m. In addition, we restrict our analysis to the $q_m \leq M$ domain, since the overcharged scenario is non-physical. Utilizing the effective geodesic method described in section 2.2, we find that we are able to push the value of q_m up to $q_m = 0.88M$, a slightly less restrictive constraint than the one reported by Vea, of $q_m \lesssim 0.8M$.

3. Bardeen's regular BH.

Belonging to the class of regular black holes (i.e. also dubbed non-singular black holes, are characterized by the absence of the curvature singularity occurring at $r = 0$ [116]), this alternative geometry is one of the first of its kind to have been proposed [199]. Bardeen suggested replacing the central curvature singularity with a de Sitter vacuum core (i.e. positive space-time curvature), accomplishing this via a magnetically charged solution [200]. The resulting geometry is defined in terms of the following metric function [199]

$$A(r) = 1 - \frac{2Mr^2}{(r^2 + q_m^2)^{3/2}}, \tag{3.18}$$

where q_m represents the magnetic charge. Similarly to the RN metric, the presence of an event horizon is restricted to $q_m \leq \sqrt{16/27}M \approx 0.77M$. The Bardeen BH has also re-interpreted as a BH possessing a

non-linear magnetic monopole structure, within the framework of NED coupled-gravity [201]. However, the metric function derived this way does not lead to functions H and h which smoothly recover the Schwarzschild background geodesics in the $q_m \to 0$ limit. Hence we opt for focusing on the original Bardeen metric and proceed with the generation of BH images considering background geodesics. In this regard, Vagnozzi et al. report that all values within this range are compatible with 2σ shadow's radius; a finding which we also replicate.

4. Hayward's regular BH.

Hayward's proposal [202] consists of a regular, neutral, spherically symmetric BH, within the framework of quantum gravity theory. This geometry is obtained by replacing the central curvature singularity of Schwarzschild/RN black holes by a de Sitter core with an effective cosmological constant $\Lambda = 3l^2$, with Hubble length l, that is used to smooth the central curvature irregularity. The modification yields a regular BH defined by the metric function

$$A(r) = 1 - \frac{2Mr^2}{r^3 + 2l^2M}, \tag{3.19}$$

for which the Hubble length parameter is bound to $l \leq \sqrt{16/27}M$ to describe a BH. This model is yet another instance of a space-time geometry that can also be obtained as a solution of the Einstein field equations coupled with NED ([203]), but whose effective geometry does not smoothly recover the Schwarzschild geodesics in the $l \to 0$ limit. Thus, we simulate the appearance of the Hayward BH considering background geodesics. In doing so, we find that like Bardeen's model, Hayward's BH shadow radius remains compatible with the 2σ bounds at every value of l, so we again push the parameter l until nearly saturating the critical bound to describe a BH - the same parameter constrain obtained by Vea.

5. Frolov regular BH.

The BH geometry presented by Frolov is built on similar premises as the Hayward BH, while aiming to resolve a property of the latter that poses challenges for a self-consistent description of an evaporating BH case [204]. This endeavour led Frolov to introduce a novel BH space-time. One that generalizes Hayward's model with the inclusion of a charge parameter (i.e. here interpreted as an electrical charge q_e) with the metric function [204]

$$A(r) = 1 - \frac{(2Mr - q_e^2)r^2}{r^4 + (2Mr + q_e^2)l^2}, \tag{3.20}$$

which describes a charged, regular, spherically symmetric BH with an effective cosmological constant. By inspection of this metric function, we observe that underlying space-time in the $q_e \to 0$ limit corresponds to the Hayward geometry, whereas the $l \to 0$ limit recovers the RN space-time geometry. Like the RN and Hayward space-times, its parameters q_e and l are confined between $0 < q_e \leq 1$ and $0 < l \leq \sqrt{16/27}M$, respectively. Whether this space-time represents a BH or a naked singularity depends on the interplay between the two. In Vea [81], they propose to fix $l = 0.3$, which results in a constraint $q_e \lesssim 0.9M$. However, at the parameter values saturating this bound Frolov's solution does not describe a BH, but instead a horizonless geometry by a small margin; for instance, a value of $q_e = 0.875M$ describes a BH instead, but only a slightly larger shadow radius. Though we keep the value of $l = 0.3$ in order to keep consistent with Vea's choice, we opt for considering Frolov black holes with $q_e = 0.875$.

6. Bronnikov's regular NED BH.

The following space-time is another example of a regular, magnetically charged, spherically symmetric space-time, that is supported by a NED theory. Notably, this model is derived from Bronnikov's NED [113], when coupled GR to the following Lagrangian

$$\mathcal{L}(F) = 4F\cosh^{-2}\left[a(2F)^{1/4}\right] , \tag{3.21}$$

where the constant a is related to the magnetic charge via the relation $a = q_m^{3/2}/(2M)$, to remove the central singularity. The corresponding background metric function is given by [113]

$$A(r) = 1 - \frac{2M}{r}\left(1 - \tanh\left[\frac{q_m^2}{2Mr}\right]\right) , \tag{3.22}$$

with q_m denoting the magnetic charge parameter. Observing the previous expression, it is possible to re-obtain the Schwarzschild geometry for values of $q_m = 0$, as well as the RN geometry when performing a Taylor series expansion around small values of q_m. The corresponding effective geometry correctly reproduces this asymptotic behaviour. Thus, we resort to the effective geometry to compute the shadow radius and find the 2σ lower bound is saturated at $q_m = 0.905M$; a much tighter range than the constraint $q_m \lesssim M$, reported in Vea.

7. The Ghosh-Culetu-Simpson-Visser (GCSV) NED regular BH.

Continuing with regular space-times, the Ghosh-Culetu-Simpson-Visser model is unique among the other regular geometries listed here, in that its core is asymptotically Minkowsi rather than being asymptotically de Sitter [205]. The GCSV geometry may be obtained through a GR coupling with a NED field, provided by the Lagrangian density [206]

$$\mathcal{L}(F) = F\exp\left[-\frac{q_m}{2M}(2q_m^2F)^{1/4}\right] , \tag{3.23}$$

with a magnetic monopole charge q_m. The resulting background geometry is characterized by a negative exponential term and its functional form is given by [205, 207, 208]

$$A(r) = 1 - \frac{2M}{r}\exp\left[\frac{-q_m^2}{2Mr}\right] , \tag{3.24}$$

with $q_m \lesssim 1.21M$[3] to describe a BH space-time [148]. This metric also simplifies to the Schwarzschild geometry by setting $q_m = 0$, and admits a RN-like 2^{nd} order approximation, at the limit of $q_m \to 0$. In Vea, it is reported that q_m can be pushed up to $|q_m| \lesssim M$ using the background geodesics. However, we find that the associated effective functions, H and h, turn out to be well behaved and obtain our own constraint under effective geodesics. In this regard, we report that the magnetic charge value saturating the lower shadow bound is $q_m = 0.88M$.

8. The Ghosh-Kumar (GK) BH.

This next geometry consists of a simple modification of the Schwarzschild geometry and it is derived from the action of GR minimally coupled to a suitable NED Lagrangian density [209]. It represents

[3] This value is computed by taking $l = \frac{q_m^2}{2M}$, from the provided reference.

a magnetically charged, regular, spherically symmetric vacuum that is supported by a self-gravitating magnetic monopole q_m, via the function

$$A(r) = 1 - \frac{2M}{\sqrt{r^2 + q_m^2}} \,, \tag{3.25}$$

which is reduces to the Schwarzschild metric at the $q_m \to 0$ limit. The presence of an event horizon is contingent on $0 \leq q_m \leq 2M$. We also note that, this is another instance of an alternative geometry that can be generated within a NED framework (i.e. see corresponding discussion for the Bardeen and Hayward alternative geometries) where the corresponding effective geodesics do not recover the Schwarzschild space-time in the limit $q_m \to 0$. This way, we opt for considering the usual background geodesics as in Vea, and find their upper bound of $q_m \lesssim 1.6M$ may be relaxed up to $q_m = 1.63M$, towards the generation of our images.

9. Kazakov-Solodukhin (KS) regular BH.

The Kazakov-Solodukhin space-time is yet another regular BH and it is the first string inspired model we include in our work. It arises when considering the deformation of the Schwarzschild solution due to spherically symmetric quantum excitations of the metric and the matter fields, governed by 2-Dimensional dilaton[4]-gravity action [211]. Its functional form is given by

$$A(r) = -\frac{2M}{r} + \frac{\sqrt{r^2 - l^2}}{r} \,, \tag{3.26}$$

where, l represents the scale over which the central Schwarzschild singularity is smoothed over, due to quantum corrections. Thus, in order to avoid the central singularity, the model requires that $l > 0$. In this way, the KS geometry describes a neutral, quantum-deformed, spherically symmetric space-time, that is regular near its core. It is possible to observe that, despite its unusual shape for a metric function, it reduces to the Schwarzschild metric at large distances (i.e. when $r \gg l$) and remains asymptotically flat when $r \to \infty$, as required by our inclusion criteria. Vea report that 2σ observations require that $l \lesssim M$, but we find the shadow bound becomes saturated at a tighter constraint of $l = 0.942M$.

10. Einstein-Maxwell-Dilation (EMD) BH.

Continuing with string inspired models, Einstein-Maxwell-Dilaton gravity BH solutions have been derived within the subject of the low energy effective field theory describing string theory, when an additional scalar (dilaton) field is included within GR coupled to a Maxwell field [212]. The particular BH geometry presented here is the electrically charged, spherically symmetric configuration, whose metric function reads

$$A(r) = 1 - \frac{2M}{r}\left(\sqrt{1 + \left(\frac{q_e^2}{2Mr}\right)^2} - \frac{q_e^2}{2Mr}\right) \,, \tag{3.27}$$

where q_e is an effective charge related with the dilaton scalar charge. Studying the presence of horizons in this space-time reveals that $0 \leq q_e \leq \sqrt{2}M$, for the existence real horizons. According to Vea, the EHT's 2σ shadow bounds limit $q_e \lesssim M$, but we find a slightly more refined constraint with $q_e = 0.995M$.

[4]The dilaton is a neutral scalar field that appears in string theory. Its value controls the gravitational interaction strength [210].

3.3 Choice of spherically symmetric space-times

11. Sen non-rotating BH.

Originally derived as rotating solution within the low energy limit of an effective field string theory [213], the Kerr-Sen BH space-time describes an asymptotically flat, charged, rotating BH space-time. In addition to the inclusion of a dilaton scalar field, Sen's model also takes into account the presence of an anti-symmetric third order tensor field [214] in the GR Lagrangian, along with the Maxwell field tensor. Here we present the non-rotating counterpart of the Kerr-Sen BH, whose metric function is written as

$$A(r) = 1 - \frac{2M}{r + q_m^2/M} \,, \tag{3.28}$$

where q_m is an effective charge associated with the dilaton field. Akin to the EMD BH, the effective charge parameter lies between $0 \leq q_m \leq \sqrt{2}M$, in order for this space-time to possess real horizons. In Vea, the 2σ shadow bound constrain the effective charge to $q_m \lesssim 0.75M$, noting that X-ray reflection spectroscopy has yielded a slightly stronger constraint of $q_m \lesssim 0.6M$ [215]. We opt for considering the latter bound during our generation of BH images.

12. Simpson-Visser (SV) black bounce BH.

Our first example of a non-trivial $C(r)$ function is provided by the so-called black bounce, which denotes a metric originally introduced by Simpson and Visser [100], and whose philosophy is to replace the radial coordinate of the Schwarzschild geometry by a radial function implementing the bounce, the latter interpreted as the throat of a wormhole (WH) (i.e. a space-time geometry that connects two distant regions of the same universe, or two separate universes [216]) with radius a. In order to do it so, Simpson and Visser follow the prescription of Ellis [97] from the radial coordinate shift, in such a way that the metric functions read as

$$A(r) = 1 - \frac{2M}{\sqrt{r^2 + a^2}} \,; \qquad C(r) = r^2 + a^2 \,. \tag{3.29}$$

These functions describe a static and neutral vacuum which, depending on the value of a, interpolates between a Schwarzschild BH ($a = 0$), a regular BH ($0 < a < 2M$), a WH with an extremal null throat ($a = 2M$), or a traversable WH ($a > 2M$). With this metric function, SV black bounce is close in spirit to previously presented the GK space-time. Despite having identical metric functions, the nature of the parameter characterizing each geometry as well as the presence of a non-trivial $C(r)$ function in this case, result in a fundamentally different space-time structure. Though a seemingly affects the presence and location of a horizon and photon sphere, when plugging these metric functions into Equations (2.36), they have identical properties to those in a Schwarzschild space-time (2.38), as revealed by coordinate change $R \to r^2 + a^2$. Moreover, plugging the above metric functions into equation (2.47), reveals that the shadow size is independent of the parameter a. Because of the way it is built, this model has the same critical impact parameter (i.e. shadow radius) as its seed metric - the Schwarzschild BH - for every value $0 < a < 3M$[5], so it is not constrained by the EHT results at all. We recall the discussion in [85] concerning this very same shadow degeneracy. In light of this, we take the value chosen by Vea, $a = 0.5$, which is approximately close the most stringent constraint of $a \lesssim 0.49M$ obtained through X-ray reflection spectroscopy [217]. In doing so, we remain within the sub-class of these configurations that have an horizon (corresponding to $0 < a \leq 2M$), in alignment with our criteria. Finally, we note that this is yet another case of a geometry that has been found as a solution of GR coupled to suitable NLED source, along with an minimally coupled scalar field [218]. However, such solution is excluded from our analysis on similar grounds to the Bardeen, Hayward, and GK models.

[5] A photon sphere is absent from this geometry for $a \geq 3M$.

13. Loop Quantum Gravity (LQG) BH.

In addition to string inspired models, we also include a BH geometry found within the realm of Loop Quantum Gravity - one of the leading approaches towards reconciling GR with quantum mechanics. Specifically, we include a regular metric that is a spherically symmetric LQG-corrected Schwarzschild metric, taking the following form [99]

$$A(r) = \frac{(r-r_+)(r-r_-)(r+r_\star)^2}{r^4+a_0^2}\ ; \qquad C(r) = r^2 + \frac{a_0^2}{r^2}\ , \tag{3.30}$$

with the definitions $r_+ = 2M(1+P)^2, r_- = 2MP^2/(1+P)^2, r_\star = \sqrt{r_+ r_-}$, and two parameters of the theory [99, 219]: P which is associated with the space-time geometry quantization; a_0 setting the minimum quantization scale. In spite of the unique shape of the metric function, it returns to the Schwarzschild geometry when $P = a_0 = 0$. Since there are two free parameters in this geometry (note: excluding the mass M), we take the same approach as Vea and set $a_0 = 0$. Such a choice does not significantly impact the generation of BH images, since the order of magnitude of this parameter is extremely small[6] P[99], and negligible against the values of P that affect the BH shadow size [220]. Taking this in consideration, Vagnozzi et. al report the constraint $P \lesssim 0.08M$ for compatibility with 2σ shadow bound. We find we are able to saturate the same shadow bound at a more refined constraint of $P = 0.082M$.

14. Conformal scalar model (ConfSca) BH.

The conformal scalar model emerges as a solution to the Einstein-Maxwell action conformally coupled to a constant scalar field [221]. The neutrally charged and spherically symmetric geometry is described by

$$A(r) = 1 - \frac{2M}{r} - \frac{s}{r^2}\ , \tag{3.31}$$

where s represents a scalar hair parameter. Such a case is an example of a family of configurations which resemble the RN space-time but instead of possessing a quadratic charge term, the correction term is raised to the power of one. So we can take it as a benchmark for this kind of metrics. We also purposefully present the metric function with a negative sign in the $1/r^2$ term [7], which is the sign convention where positive values of s correspond to the regime we aim to study [222]; the so-called "mutated RN" geometry. With this sign change in mind, Vea report an upper limit of $s \lesssim 0.4M$, whereas we find its value can be pushed up to $s = 0.45M$ for compatibility with the 2σ shadow bound.

15. Dark matter (DM)-surrounded BH.

To complement the alternative geometries so far, we include a BH surrounded by an external matter field. Specifically, we address the scenario of a BH surrounded by a cold dark matter (DM) fluid. In such a case, the Schwarzschild solution is corrected via an additional term, as given by [223]

$$A(r) = 1 - \frac{2M}{r} + \frac{k}{r}\log\left(\frac{r}{|k|}\right)\ , \tag{3.32}$$

where k is an integration constant related to the quantity of DM surrounding the BH space-time. Thus,

[6] $a_0 \sim l_P^2$, where l_P is the Planck length.

[7] In this way, the metric is identical to the RN space-time for negative values of s, describing a RN BH when $s > -M^2$. Note that this is the opposite to the sign convention used by Vea, where instead positive values of s represent a RN BH.

the above function describes a neutral, static and spherically symmetric vacuum, externally surrounded by DM. In addition to meeting our criteria for the alternative geometries to be included, this scenario bears relevance in light of the existing observational evidence supporting the presence of DM in most galaxies [224]. Vea report an upper limit for $k \lesssim 0.15M$ but we find the bound on the shadow's size to be saturated at a lower value, $k = 0.128M$.

16. Janis-Newman-Winicour (JNW) naked singularity.

To complete our alternate geometry sample, we include a naked singularity - the Janis-Newmann-Winicour solution. This is done for the sake of comparison with BH images (i.e. since it can mimic the appearance of a BH despite the absence of an event horizon), the historic relevance of such geometries and their connection with the weak cosmic censorship hypothesis [225]. The JNW solution is a neutrally charged naked singularity supported by a massless scalar field, via the metric function [226]

$$A(r) = \left[1 - \frac{2M}{r(1-\nu)}\right]^{1-\nu} \quad ; \qquad C(r) = r^2 \left[1 - \frac{2M}{r(1-\nu)}\right]^{\nu} , \tag{3.33}$$

where ν is a parameter related to the scalar charge of the field supporting it, limited between $0 \leq \nu < 1$. In particular, between $0 \leq \nu \leq 0.5$, this geometry contains a photon sphere and is thus capable of casting a shadow. However, unlike BH space-times, the horizonless nature of this space-time means that light rays above the maximum of the potential will find no obstacle to reach the center of this space-time, thus posing a different scenario for the shadow than that of BH space-times. For this space-time, Vea report the constraint $\nu \lesssim 0.45M$, though we find we can push this value up to $\nu = 0.4835M$.

We compile our own parameter constraints into Table 3.1, along with the associated critical impact parameter, and the constraints obtained by Vea. As we can see in the Table, most of our constraints

Table 3.1: Parameter constraints, in units of mass M, of the 16 alternative spherically symmetric geometries considered in this work (see abbreviations in the main text): Vea - parameter values constraints reported by Vagnozzi et al. [81]; Parameter - parameter values constraints obtained by comparing the critical impact parameter with the 2σ bounds for the shadow size of Sgr A* . A precision of three significant digits was used for the latter.

Space-time	$Vea(M)$	$Parameter(M)$	Space-time	$Vea(M)$	$Parameter(M)$
RN	0.95	0.939	KS	1	0.942
EH (e)	0.8	0.880	EMD	1	0.995
Bardeen	$\sqrt{16/27}$	$\sqrt{16/27}$	Sen	0.6	0.600
Hayward	$\sqrt{16/27}$	$\sqrt{16/27}$	SV	0.5	0.500
Frolov	0.90	0.875	LQG	0.08	0.082
Bronnikov (e)	1	0.905	ConfSca	0.4	0.450
GCSV (e)	1	0.880	DM	0.15	0.128
GK	1.6	1.63	JNW NS	0.45	0.484

come close to the ones reported by Vea. In general, we find that the small discrepancies between the results may be attributed to the additional precision we placed on our own constraints, whenever the constraints are exclusively due to the shadow bounds. We highlight the notable exceptions in the Frovlov BH, for which we chose to remain within the parameter space representing a BH geometry, and the GCSV BH, for which Vea did not consider effective geodesics and provided the parameter constraint for the background geometry instead. We also depict the effective potential for this set of sixteen spherically symmetric geometries (plus Schwarzschild) in the panels of figure 3.3. From this Figure it is possible to

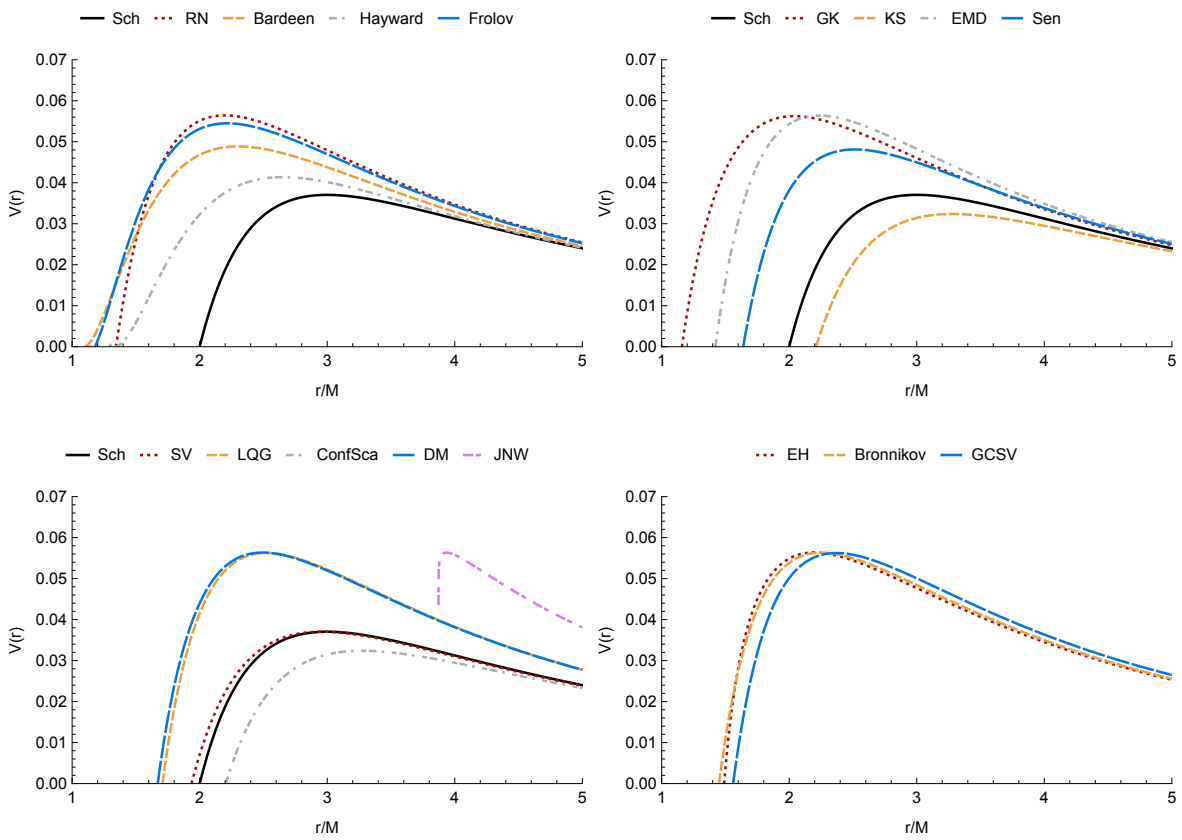

Figure 3.3: The effective potential curves for 16 alternative geometries with the parameter values that saturate the 2σ shadow bounds of Sgr A*. Top row and bottom left panel: Geometries with background geodesics are compared against the Schwarzschild BH. Bottom right panel: Geometries with effective geodesics. For every space-time geometry, we only represent the effective potential curve beyond the external event horizon.

see that, at parameter value constraints we are working with, the effective potentials significantly deviate from the Schwarzschild effective potential (indicated by the black line). Despite the shadow bound being saturated in most cases, the effective potential curves are different for each case, with distinct locations of maximum peak, event horizons (i.e. where the potential curves intersect the horizontal axis), and the curve shapes, hinting at the unique structure of their corresponding space-time. The fact that the JNW geometry lacks horizons is also evidenced in this Figure. Its effective potential qualitatively deviates from the others, being undefined for certain values of r. We note that some of the potential curves extend inwards, possessing critical minima and additional event horizons. However, such behaviour plays no role in simulating the appearance of a BH, since this region is covered by an external event horizon (i.e. the outermost r_H). Hence, we only display the effective potential curve beyond the external event horizon as only this region is relevant for the generation of images. This would not be so in those cases in which the EHT bound is not saturated, where pushing the parameter space any further would result in the disappearance of the event horizon. In these instances, the internal structure of the space-time (i.e. shape of the potential) is relevant in the generation of images, resulting in a multi-ring structure provided that it has additional minima/maxima or an infinite slope at the center [148]; however such features will be absent from our images.

3.4 Discarded models

In the previous section, we have presented the 16 alternative geometries selected out of the 41 models constrained by Vea, leaving out a fair number of models for which parameter space constraints have been obtained. In what follows, we review the reasons that have led to the exclusion of the remaining models. We identify any excluded models by their name and respective subsection identifier in Vea.

First and foremost, we do not consider non-asymptotically flat space-times (i.e. when $A(r_\infty) \to \infty$) where the asymptotic mass [227, 228] of the space-time cannot be directly interpreted as the local mass M. In such cases, the relation between the critical impact parameter and the shadow radius derived in equation (2.47) does not stand [87]. Computing the shadow and the observed intensity in the observer's screen requires accounting for the radial coordinate of the observer, as seen in equations (2.46) and (3.12), respectively; though there are other techniques to addressing this (e.g. considering a co-moving obeserver in the expanding universe model - the Kottler BH [46]). Overall, the asymptotic flatness, or lack thereof, prevents the generation and comparison of BH images on equal footing. This criterion leaves out models such as the Clifton-Barrow f(R) gravity [R], Kottler BH [AE], Rindler gravity [AH], and the BH with topological defect [AJ]. Secondly, we do not factor in any space-times that can be rewritten (e.g. via a redefinition of constants) in a usual RN-like form. This is due to being able to convert the same constraints placed upon the RN solution into constraints on each theory's parameters, leading to identical photon rings features. This option excludes cases like the Conformal scalar model [Q] for $s < 0$[8], Horndeski *case* 1 [S.1], Modified Gravity [T], Brane-world black holes [U], or the second non-commutative gravity model [AM.B]. We also exclude any models which: a) have too tight constraints on their parameter space to significantly alter the $n = 1$ and $n = 2$ ring properties like models in Einstein-Aether gravity [Z], 4D Gauss-Bonnet gravity [AA], Asymptotically safe gravity [AB], Rastall gravity [AC], Electromagnetic-Weyl coupling [AF], and the first non-commutative gravity model [AM.A]; b) are directly ruled by the current shadow observations, like the Morris-Thorne Wormhole [J], and the null naked singularity [O]. Finally, we exclude space-times described by glued solutions, containing potential discontinuities, such as the Joshi-Malafarina-Narayan naked singularity [M] and the Naked Singularity surrounded by a thin shell matter layer [N], or others demanding excessive computational times .

[8] For $s > 0$ using Vea's sign convention.

Chapter 4

Results and Physical Discussion

The main results of the approach described in chapter 3 are presented ahead, together with a comment on their physical meaning and connection with existing literature, whenever applicable. The first section presents the application of the previous methodology to the Schwarzschild BH. In the second section, the theoretical Lyapunov exponent associated to each of the sixteen alternative geometries is used to explore correlations between itself and the quantities that are relevant for the production of BH images (e.g. the critical impact parameter). In the following sections, the observed extinction ratio between the $n = 1$ (first) and $n = 2$ (second) rings is compared against its theoretical counterpart, as predicted by the Lyapunov index. The discussion is done separately for each GLM emission profile described in section 3, focusing the GLM3 model in the second section and both GLM1 and GLM2 models in the third section.

4.1 Schwarzschild Black Hole Images

In figure 4.1, we illustrate the optical appearance of the Schwarzschild BH illuminated by a thin accretion disk modeled with the GLM emission profiles (2.38). The panels on the left side column depict the intensity profile as it is seen in the observer's frame of reference, with normalized intensity fluxes. The panels on the right side depict appearance of a Schwarzschild BH of mass M in the observer's sky, when seen from a face-on orientation. Each row corresponds to the GLM models 3.2, 3.3, and 3.4, respectively. The images presented here are consistent with those of previous studies in the field (e.g. [47, 66]), thus validating our approach in the generation of BH images. Focusing on the left column panels, we now discuss the location of the emission peaks corresponding to the $n = 1$ and $n = 2$ subrings. For the GLM3 model, these peaks are separated from the direct ($n = 0$) emission, in agreement with our initial expectations. Indeed, this facilitates their visualization in the corresponding BH image on the right column, where it can be seen that the first and second rings are increasingly thinner. Moreover, these lensed features are still present despite the absence of emission near the BH photon sphere and horizon. The observed intensity profiles for GLM1 and GLM2 models are presented in the middle and bottom rows. Recalling that, in these models, the emission profile extends all the way to the horizon, it is possible to discern a decay in emission that ends before the event horizon is reached. Inside this region, one sees a CBD that is larger than the event horizon, concealing the latter from an external observer. As previously mentioned, this optical phenomenon is caused by gravitational redshift that is stronger for photons that are emitted closer to the BH event horizon. In such cases, it is also possible to observe that the $n = 1$ and $n = 2$ emission overlaps with the direct emission. This is evidenced by the increasingly thinner peaks in these model's observed intensity panels, which manifests as an increase in brightness near the theoretical critical critical curve, in the corresponding BH images. Comparing the

4.1 Schwarzschild Black Hole Images

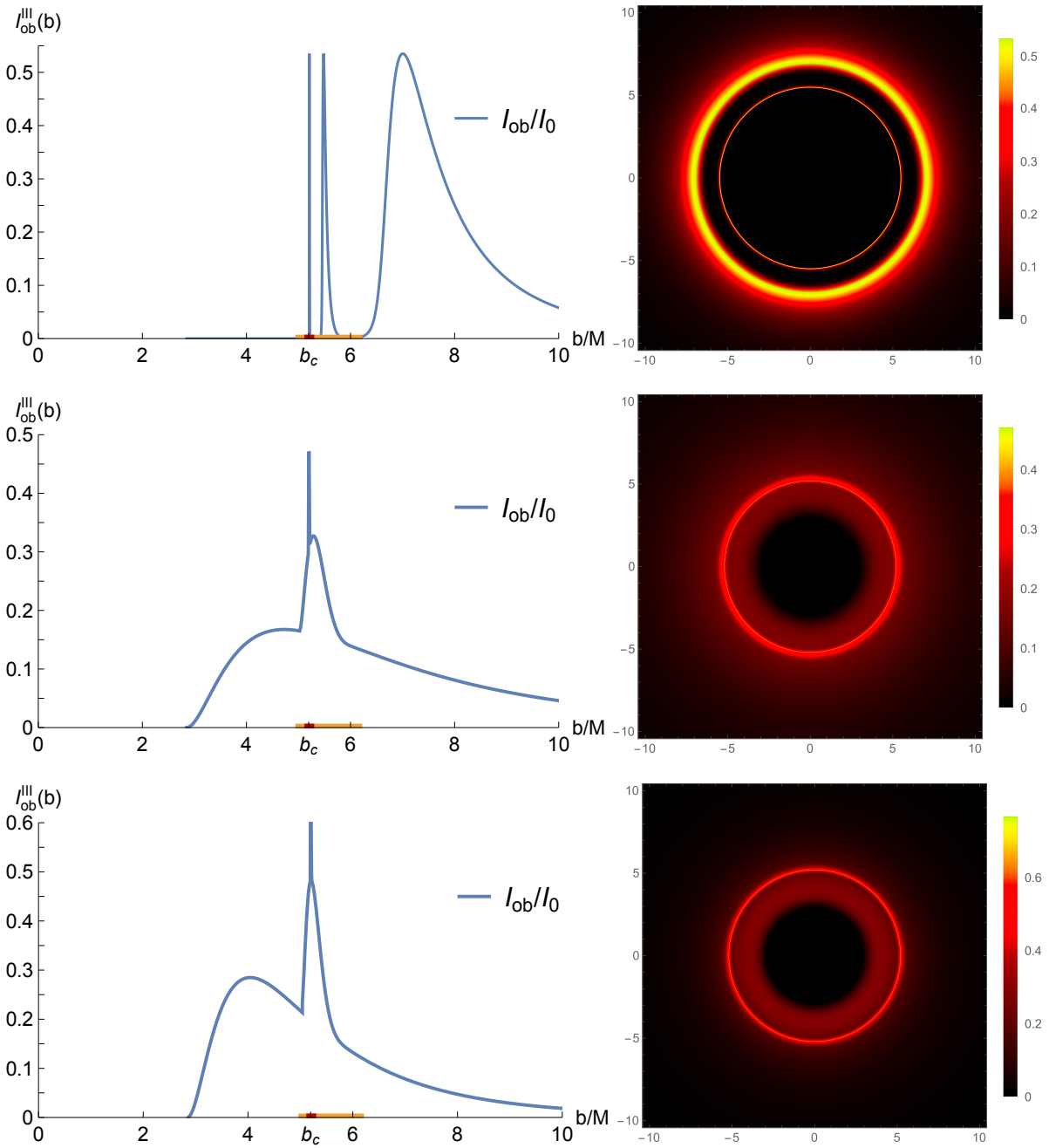

Figure 4.1: Observed emission profile and visual appearance of the Schwarzschild geometry, for three GLM profiles, viewed from a face-on orientation. Each row corresponds to one of the GLM models: GLM3 (top), GLM1 (middle), GLM2 (bottom). Left panels: The observed intensities I_{obs} are normalized to the maximum value I_0 of the emitted intensity; the impact parameter is expressed in units of M. The full range of possible impact parameters of the $n = 1$ and $n = 2$ rings is displayed in the horizontal axis with gold and red colors, respectively. Right panels: Visual appearance of the Schwarzschild geometry in the impact parameter space (in units of M) of an observer located at a distance of $r = 1000M$.

observed emission between the different models illustrates how the photon ring emission is increasingly independent of the choice of profile. The $n = 0$ emission depends strongly on the emission profile, presenting significant differences between all GLM models. In contrast, the shape and location of the $n = 1$ emission is only modestly affected by the choice of profile, whereas the $n = 2$ emission always lies near the critical impact parameter regardless of the GLM model choice. Overall, these images are fairly consistent with the images captured by the EHT, showing a bright radiation ring encircling a darker region. A notable feature of the GLM1 and GLM2 Schwarzschild BH images is that the size of the

central brightness depression does not coincide with the critical curve (i.e. the shadow boundary), which is consistent with the scenario of a thin accretion disk that extends all the way towards the event horizon, as discussed in Section 2.4.

4.2 Lyapunov exponents and extinction ratios

In table 4.1 we present the data on the main geometrical quantities and image features of the alternative space-time geometries considered in Section 3. The space-time models in this table are organized in descending order of their corresponding theoretical Lyapunov exponent γ, which was computed for the $n = 1$ and $n = 2$ rings. Taking the Schwarzschild space-time as a reference, we report twelve space-time geometries for which γ decreases, and four for which it increases.

Table 4.1: The alternative spherically symmetric geometries considered in this work (see section 3.3 for abbreviations and chosen model parameters) organized according to decreasing values of their corresponding theoretical Lyapunov exponent, computed for the $n = 1$ and $n = 2$ rings. The listed quantities include: r_h - horizon radius; r_{ps} - photon sphere radius, b_c - critical impact parameter; the Lyapunov exponent (in bold) and its associated (theoretical) luminosity extinction ratio (I1/I2 [in brackets]); the observable extinction ratio (sub-labels for each GLM emission profile). r_h, r_{ps} and b_c are presented in units of mass M. The row corresponding to the Schwarzschild solution is greyed out, as a reference against which other geometries are compared. The space-times with the suffix (e) denote the geometries supported by effective geodesics (see section 3.3 for corresponding discussion). Digit precision limited to three decimals for theoretical quantities and to two decimals for observational ones.

Space-time	$r_h(M)$	$r_{ps}(M)$	$b_c(M)$	**Lyapunov** $[I_1/I_2]$	$I^{\frac{n=1}{n=2}}_{GLM3}$	$I^{\frac{n=1}{n=2}}_{GLM1}$	$I^{\frac{n=1}{n=2}}_{GLM2}$
LQG	1.708	2.521	4.216	3.372 [29.150]	35.59	31.01	29.53
KS	2.214	3.279	5.559	3.288 [26.809]	30.95	28.24	26.93
ConfSca	2.204	3.274	5.556	3.278 [26.530]	30.66	27.96	26.65
DM	1.671	2.493	4.212	3.268 [26.259]	32.28	27.95	26.56
Schwarzschild	2	3	$3\sqrt{3}$	3.150 [23.352]	27.83	24.74	23.45
SV	2	3	$3\sqrt{3}$	3.107 [22.367]	26.79	23.69	22.41
JNW NS	n.a.	1.453	4.213	3.096 [22.128]	21.02	20.52	19.95
Sen	1.640	2.514	4.558	2.887 [17.946]	22.96	19.27	18.02
GCSV (e)	1.560	2.370	4.217	2.693 [14.782]	19.88	15.73	14.16
EMD	1.421	2.234	4.211	2.665 [14.381]	19.47	15.62	14.43
Bronnikov (e)	1.449	2.253	4.213	2.587 [13.292]	18.34	14.51	13.15
Hayward	1.337	2.652	4.916	2.542 [12.708]	17.45	14.02	12.77
RN	1.343	2.197	4.209	2.527 [12.524]	17.26	13.78	12.61
EH (e)	1.490	2.197	4.212	2.418 [11.229]	18.41	12.20	10.88
Frolov	1.179	2.216	4.283	2.403 [11.066]	15.58	12.41	11.17
Bardeen	1.093	2.301	4.524	2.253 [9.516]	13.27	10.75	9.56
GK	1.158	2.038	4.216	2.100 [8.166]	11.74	9.21	8.21

By inspection of table 4.1, we report that no significant correlation exists between the presented geometrical quantities (i.e. horizon radius, photon sphere radius, critical impact parameter) and γ. It is possible to observe that increasing a geometry's associated parameter (i.e. thereby increasing the deviation from the Schwarzschild space-time) typically tends to increase the space-time compactness (i.e. decrease r_h) and, by extension, results in a smaller shadow radius, though this behaviour is not linear. We additionally note that there are exceptions to this tendency, such as the KS and ConfSca space-times, whose compactness decreases, and the SV space-time which remains unchanged. These results are in agreement with those of Vea, who also commented on the previous trend.

The decrease in the r_h appears to be accompanied by a decrease in the corresponding Lyapunov exponent but this is not always the case. Excluding the JNW naked singularity, for its lack of an event horizon, and the geometries that do not saturate the EHT bounds (i.e. SV, Hayward, Frovlov, Bardeen), due to having their associated parameters theoretically or experimentally constrained, this trend is also contaminated by the geometries supported by effective geodesics (i.e. GCSV, Bronnikov, EH). For the photon sphere radius r_{ps}, the correlation with the Lyapunov exponent is even weaker than the previous one. Once more, we verify that r_{ps} is smaller for more compact geometries and larger for less compact ones, but this behaviour is not linear. The presence and location of the photon sphere is deeply connected with the space-time geometry. The majority of extensions to the Schwarzschild metric have a profound impact in the geodesic trajectories of photons, which generally (but not always) changes the photon sphere radius. This aspect is further complicated when the underlying space-time does not contain an event horizon (i.e. naked singularity) or when the photons travel through effective geodesics (i.e. NED space-times). As a consequence, it is possible to have two distinct geometries with similar compactness and a significantly different r_{ps}. The γ-r_{ps} correlation is not only weakened by the NED space-times but also by the naked singularity's small r_{ps}. Lastly, there is no evidence of a correlation between the critical impact parameter b_c (the shadow's radius in the EHT interpretation) the γ index. This is the quantity that is used to constrain the parameter space of the 16 spherically symmetric space-times. We report that most geometries saturate the lower bound of the EHT constraints, a result which congruent with the research carried out by Vea. Indeed, most geometries tend to decrease the shadow radius, particularly when the corresponding constraints leave a wider margin for deviations with respect to Schwarzschild. Because there are geometries with similar b_c values yet vastly discrepant values of γ, this indicates a lack of connection between the Lyapunov index and the shadow radius.

Among the geometries in the table 4.1, the SV space-time is unique in that it possesses the same compactness, photon sphere radius and shadow radius (i.e. interpreted here via the critical impact parameter), as the Schwarzschild space-time. Such behaviour has been pointed out in past literature, drawing attention to how these space-times are indistinguishable from one another, since they cast the same shadow [85]. The fact that its Lyapunov exponent differs from the Schwarzschild's, as well as the observed extinction ratios, bodes in favour of γ's usefulness as a potential discriminator between different geometries, particularly those that could be potentially shadow degenerate. The following discussion will focus the Lyapunov exponent and its relation with the exponential decay of the luminosity of the photon rings. For this, the results in table 4.1 will be analyzed in tandem with BH images of the alternate geometries, depicted in Figures 4.2 and 4.3 for the GLM3 emission profile, 4.4 for the GLM1 profile, and 4.5 for the GLM2 profile. Similarly, the images in these figures are organized in descending order of γ.

4.3 GLM3 Model

The images and results for the GLM3 model are considered first, as this is more of a toy-model designed to disentangle the photon ring emission of the $n = 1$ and $n = 2$ rings from each other, and from the accretion disk's direct image ($n = 0$). Figure 4.2 showcases the visual appearance of the sixteen alternative geometries when illuminated by the GLM3 emission profile. As expected, the emission from the first and second rings is clearly isolated from the direct emission. Notably, the $n = 1$ ring appears as a bright thin ring inside the larger and wider ring of the direct emission. The $n = 2$ ring appears as a thinner ring that is barely visible for most geometries, becoming easier to see in the geometries with a lower associated Lyapunov index (i.e. the images in the bottom row). Nonetheless, we can already appreciate some of the differences in the visual appearance between the considered space-time

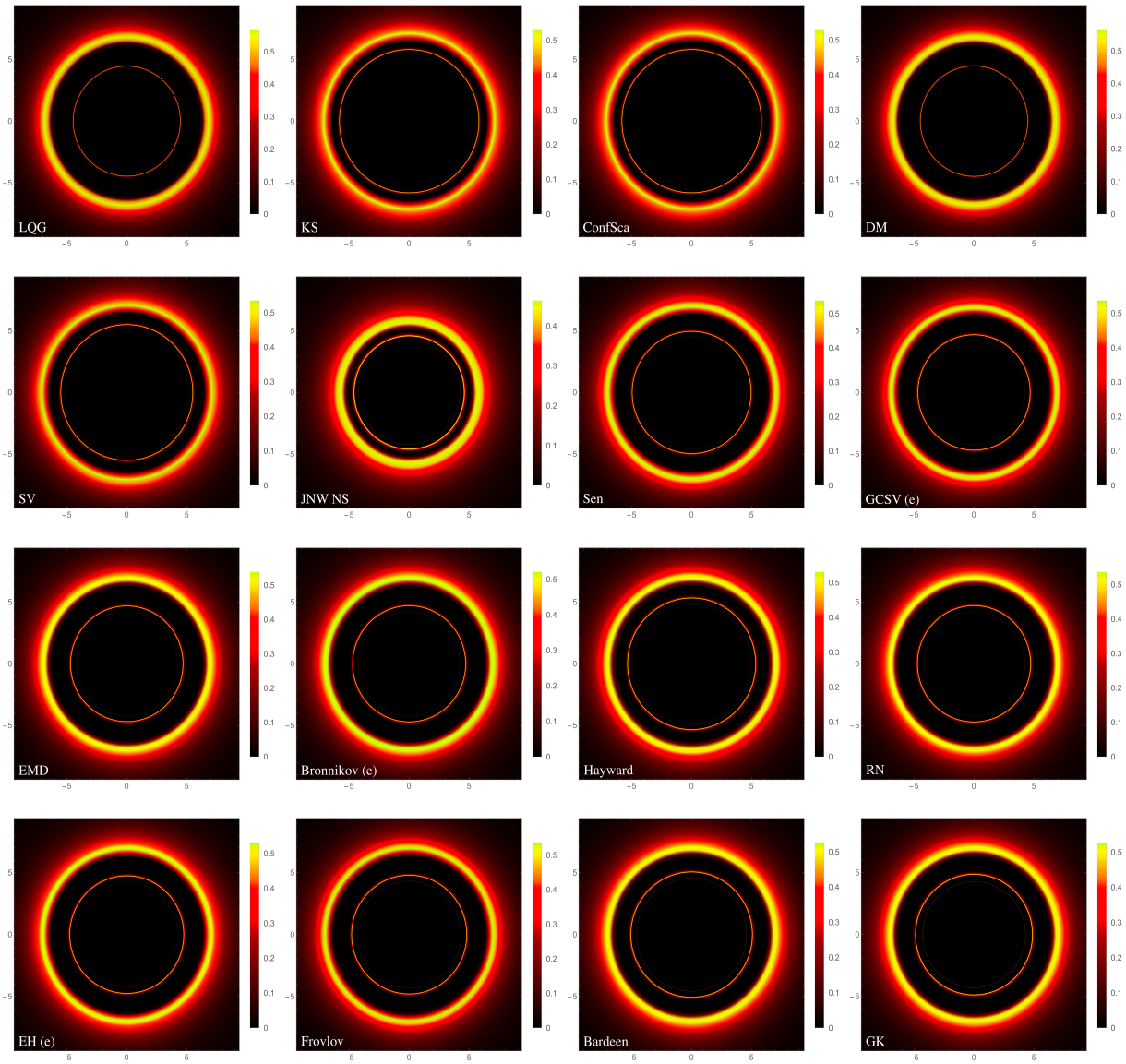

Figure 4.2: Visual appearance of the sixteen alternative spherically symmetric space-times, under the GLM3 emission profile (3.2), in the impact parameter space of an observer located at a distance of $r = 1000M$. The images are identified by the space-time abbreviation in the bottom-left corner (see section 3.3 for abbreviations and chosen model parameters) and ordered according to descending values of the theoretical Lyapunov exponent, listed in table 4.1.

geometries. For example, the location of the subrings is different in each space-time. On the other hand, the location of the inner edge of the direct emission remains largely unaffected by the choice of background geometry, with exception of the JNW naked singularity. Overall, this is behaviour is consistent with the prediction that the photon ring depends less on the accretion disk properties, and more on the gravitational lensing properties. In effect, altering the underlying space-time affects how the photon trajectories will be deflected, manifesting as a unique visual appearance in each case. Indeed, this effect is most notable in the more strongly lensed the light trajectories (i.e. photon ring), which manifests as differences in key photon ring properties, namely their locations in the impact parameter space, their width, luminosity, and the separation between subsequent rings. Note that this should not be confused with changing the accretion disk model. Obviously, the presence of photon rings depends on the existence of an optically thin emission region in the first place. The main point is that under the same illumination conditions each space-time geometry possesses a different appearance. In other

words, when the accretion disk luminosity profile is fixed, the differences that occur due to changing the background geometry become apparent. This effect is present in Figure 4.2 but due to the difficulty in discerning the $n = 2$ ring from the dark background of the image, the analysis of the evolution of such properties is done with the aid of Figure 4.3, which zooms in on the $n = 1$ and $n = 2$ rings. There, it is possible to observe differences in the aforementioned aspects of the photon ring in greater detail.

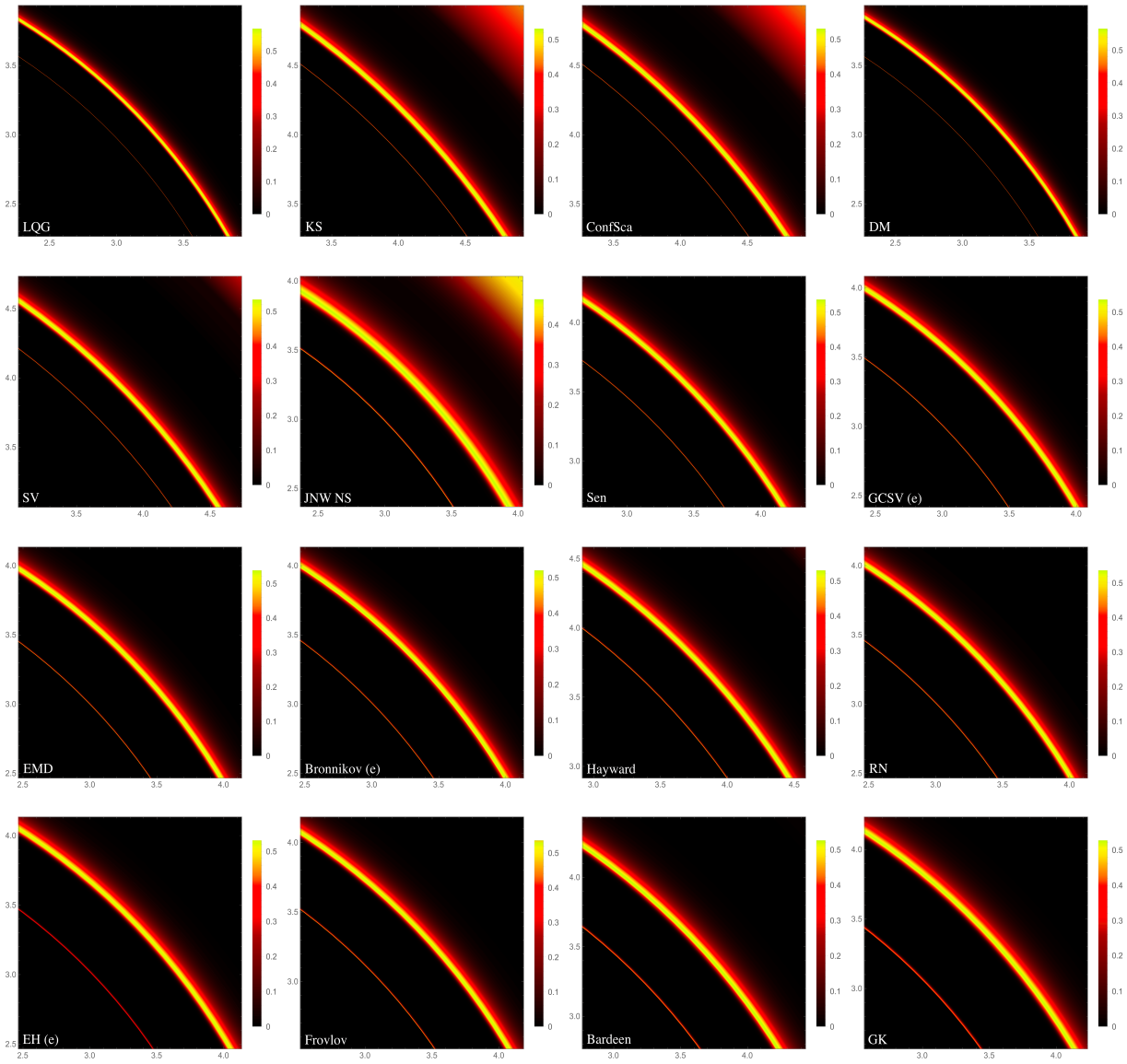

Figure 4.3: Zoomed in images of the $n = 1$ (wider) and $n = 2$ (sharper) rings for the sixteen alternative spherically symmetric space-times, under the GLM3 emission profile (3.2). The images are identified by the space-time abbreviation in the bottom-left corner (see section 3.3 for abbreviations and chosen model parameters) and ordered according to descending values of the theoretical Lyapunov exponent, listed in table 4.1. The zoom-in region, which was chosen to isolate $n = 1$ and $n = 2$ from the direct image. has the same size for all geometries of $1.6M$ by $1.6M$ in the impact parameter space.

Organizing the images according to their corresponding Lyapunov index exposes the connection between the latter and with the aforementioned properties of the rings. From a qualitative analysis of the photon ring appearance between distinct geometries, the most notable difference lies in the ring separation between $n = 1$ and $n = 2$, which tends to increase as γ decreases. We note that the effective NED geometries and the JNW naked singularity, appear to slightly deviate from the trend. The former display a larger ring separation, whereas the latter possesses the $n = 1$ ring with greatest width among our sample. Other properties such as ring location, width and luminosity, the differences are harder

to appreciate under a naked eye. While the location of the $n = 2$ photon ring is easy to determine, since it appears as a well defined sharp feature near the critical curve, the location of the $n = 1$ ring is different in every geometry. On the contrary, the change in width is harder to notice for the $n = 2$ ring, becoming more apparent when comparing the image of the geometry with the highest γ (i.e. LQG) against the geometry with the lowest γ (i.e. GK). The change in the ring luminosity is also barely noticeable, although one can still appreciate differences between the most extreme cases (i.e. LQG and GK). Specifically, in the LQG space-time, the observed extinction ratio is higher which can be seen by the more pronounced decrease in brightness on between $n = 1$ and $n = 2$. Alternatively, in the GK space-time, the observed extinction ratio is lower which manifests as a smaller decrease in brightness on between $n = 1$ and $n = 2$. Indeed, for geometries with larger values of γ, there is a greater difference between the first and second rings' luminosity, as well as a greater demagnification. Because higher γ values correspond to a greater instability of the bound photon orbits (i.e. the light trajectories are more sensitive to radial perturbations), the impact parameter range of the photon ring is smaller, therefore resulting in a decreased width and separation between rings. Their location also tracks the critical curve much more closely. The second ring is brighter than the $n = 1$ ring, but because it is so much sharper, its contribution to the total luminosity is exponentially smaller. Thus, the photon ring of geometries with a higher Lyapunov exponent provides a smaller net contribution to the total observed luminosity. On the opposite end, lower γ values correspond to lesser instability of the bound photon orbits (i.e. the light trajectories are less sensitive to radial perturbations), so the impact parameter range of the photon ring is larger in the observer's screen. This yields an increased width and separation between rings. In such instances, the photon ring is brighter, as there is a smaller relative difference between the first and second rings, thereby contributing more to the total observed luminosity. In essence, for geometries with larger values of γ the exponential behaviour of the photon ring properties is exacerbated relatively to those with smaller values of γ.

The luminosity features are better understood in light of the results in table 4.1. As can be seen in this table, when the alternative geometries are pushed to the extremes of their parameter space constraints, their observed extinction ratio varies approximately by a factor of three. When comparing the extinction ratio between $n = 1$ and $n = 2$ with their theoretically estimated counterpart, the two exhibit a strong correlation with each other, suggesting that a decrease in the theoretical extinction predicted by the Lyapunov exponent translates into a lower extinction ratio between subsequent rings. This correlation is not without exceptions, but more importantly, the theoretical extinction ratio underestimates the GLM3 observed extinction ratios by a significant margin. These results likely stem from the truncated intensity profile of the GLM3 model. As discussed in section 3.1, not only is this model abruptly truncated at the ISCO, but this value taken as the same for every geometry. Though this choice was taken in order to compare all models in equal footing, we note the ISCO is different between models. The γ index is based on the assumption that trajectories will cross regions with similar properties. This is not the case in the GLM3 model, as in these cases the photon ring trajectories complete their respective n half-orbits at a region where there is no emission.

Regardless, these results draw attention to two aspects. First, they show that the properties of the photon rings, in particular the $n = 2$ photon ring, are sensible to a change in the background space-time. This means that different spherically symmetric geometries can be distinguished from each other for a fixed emission model by ways other than their shadow radius, by looking at the lensed features of their optical appearance. In addition, they already hint at the Lyapunov exponent's potential usefulness as a proxy for discriminating between different spherically symmetric BH space-times, including those that could be shadow degenerate. An alternate option would be to explore the scenario of a fixed space-time

geometry and varying the accretion model. In such a case, the direct emission will vary significantly but the properties of the photon rings, particularly those of higher order (i.e. larger values of n), will not. Such an analysis could provide insights into which accretion models the observed extinction ratio differs most (or least) from the theoretical prediction. The special features of the JNW naked singularity also merit further discussion. Its image in Figure 4.3 depicts a clearly wider $n = 1$ ring that is much closer in distance to the accretion disk's direct emission. This effect illustrates well the distinct characteristics of horizonless geometries and raises an important issue. Namely, these objects have special gravitational lensing features in regard to the contribution to the luminosity of its rings, depending on the shape of its effective potential. This is particularly evident when comparing the shape of the JNW NS effective potential against those of the other geometries that possess a horizon, in figure 3.3. Due to this, the assumption on the exponential suppression of the luminosity of successive rings may not apply and therefore, it hinders its comparison with the alternative BH geometries considered here. By comparison with the images of the ConfSca and DM geometries, it may seem that the proximity of the $n = 1$ rings with the direct emission is a shared trait with that of the JNW NS. However, one must consider that these are the two geometries which saturate the upper bounds of the EHT shadow radius. In this sense, since the critical impact parameter is located at a much wider radius and closer to the radius at which the direct emission is truncated, these images are actually in agreement with the expectations for black holes and therefore closer to the other alternative BH geometries than to the JNW NS. This effect is thus more likely due to the choice of radius at which the GLM3 model was truncated. A final comment is made in relation to the size of the CBD and its relation with the BH shadows. In this model, it is clear that the CBD extends well beyond the critical curve, with the $n = 1$ and $n = 2$ emission appearing inside it, approximating the theoretical critical curve in the observer's image plane. As such, the CBD does not coincide with the size of the critical curve and therefore with the size of the shadow. In this regard, it is important to recall the distinction provided in section 2.4 between these two concepts. In essence, this result emphasizes the importance of referring to the shadow simply as the interior of the critical curve, rather than by darkness in the observer's sky. Given that these results illustrate well the variation of the photon ring properties but the accretion disk model supporting them is not the most realistic, the following discussion will be centered around the GLM1 and GLM2 models, which are better aligned with astrophysical expectations of emission (i.e. all the way towards the horizon).

4.4 GLM1/GLM2 Model

The images of the sixteen alternative spherically symmetric geometries, for the GLM1 and GLM2 models, are displayed in Figure 4.4 and Figure 4.5, respectively. Under these emission profiles, the images of various geometries are characterized by the typical central brightness depression, surrounded by a bright ring of radiation. The latter is dominated by the direct emission of the disk. This is quite consistent with what is known from the EHT observations. Among these images, it is also possible to observe that $n = 1$ and $n = 2$ emission overlaps with the direct emission, similarly to the Schwarzschild BH images discussed earlier. The first is harder to distinguish from the direct emission and appears as thick, bright red ring. The second ring is easier to identify, being the thinner and brighter yellow ring that appears in the images. Their presence, superimposed on the direct emission of the disk, results in a small boost to the total luminosity of the bright radiation ring. Such behaviour is well described via the extinction ratio between the photon rings: the higher the extinction ratio, the bigger the difference in luminosity between them. For example, an extinction ratio of ~ 20 between the $n = 1$ and $n = 2$ rings, indicates that the former has a net contribution to the total observed luminosity 20 times greater than the

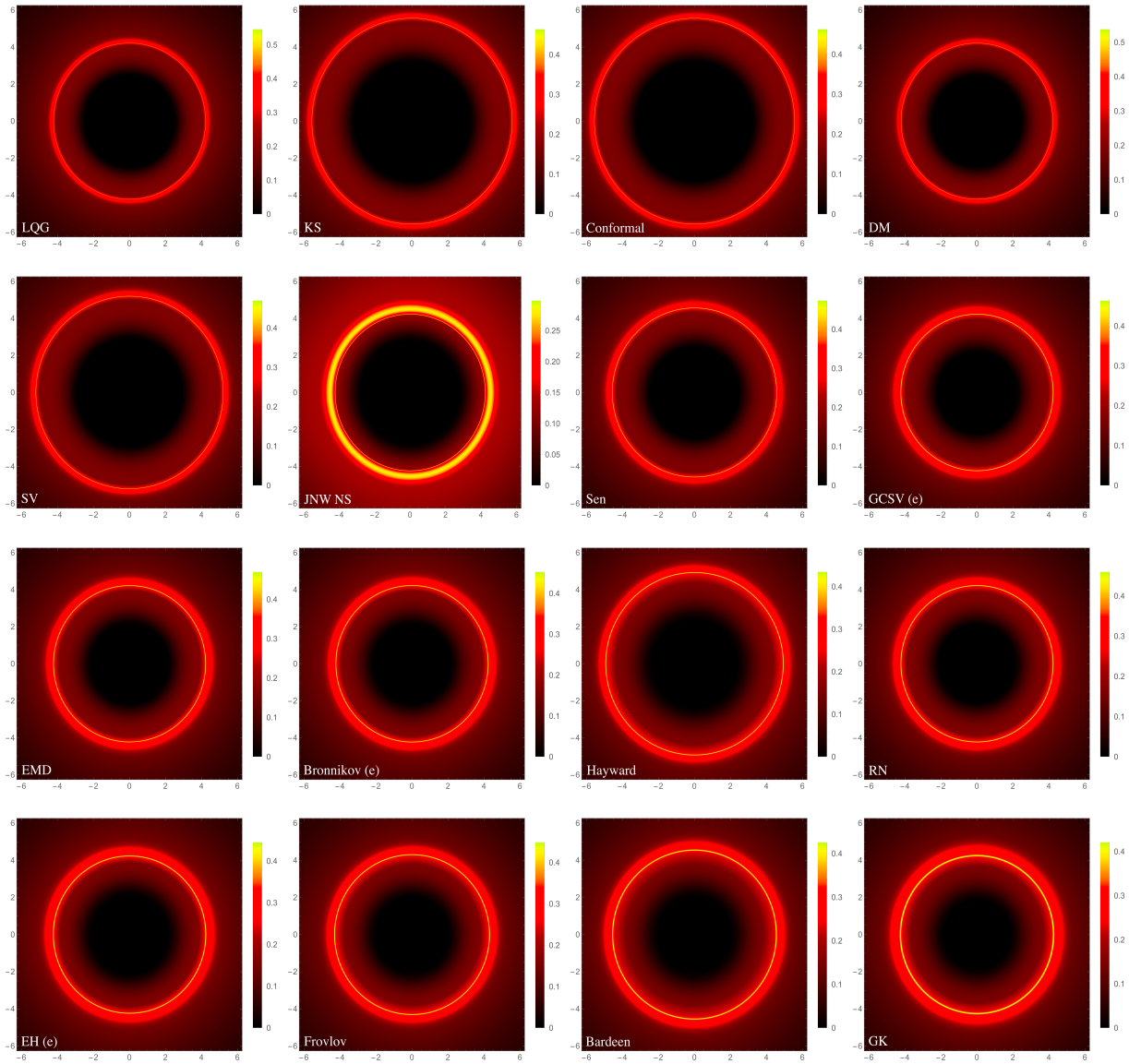

Figure 4.4: Visual appearance, in the impact parameter space, of the sixteen alternative spherically symmetric space-times, under the GLM1 emission profile (3.3), for an observer located at a distance of $r = 1000M$. The images are identified by the space-time abbreviation in the bottom-left corner (see section 3.3 for abbreviations and chosen model parameters) and ordered according to descending values of the theoretical Lyapunov exponent, listed in table 4.1.

latter. With the images of Figures 4.4 and 4.5 ordered according to a decreasing value of their associated Lyapunov exponent, we observe that the total photon ring brightness increases as γ decreases. Notably, the increment in luminosity due to the $n = 2$ ring is much smaller in the top row images, which suggests a higher extinction ratio because there is a greater difference in luminosity between the rings. By contrast, the bottom row images have better defined and wider $n = 2$ rings, which indicates the contribution to the total luminosity is higher. In other words, as the extinction ratio decreases, the relative luminosity between rings decreases, thus the photon ring appears brighter at smaller values of γ. This result is aligned with the expectations discussed in section 2.5 and in previous literature (e.g. [51]).

The extinction ratios reported in the corresponding columns of table 4.1 support the previous qualitative interpretation. Notably, it can be seen that the observed extinction ratios strongly correlate with the theoretical extinction ratio. Similarly to the GLM3 model, when pushed to the extremes of their parameter space constraints, there is a variation in observed extinction ratio by a factor of approximately

4.4 GLM1/GLM2 Model

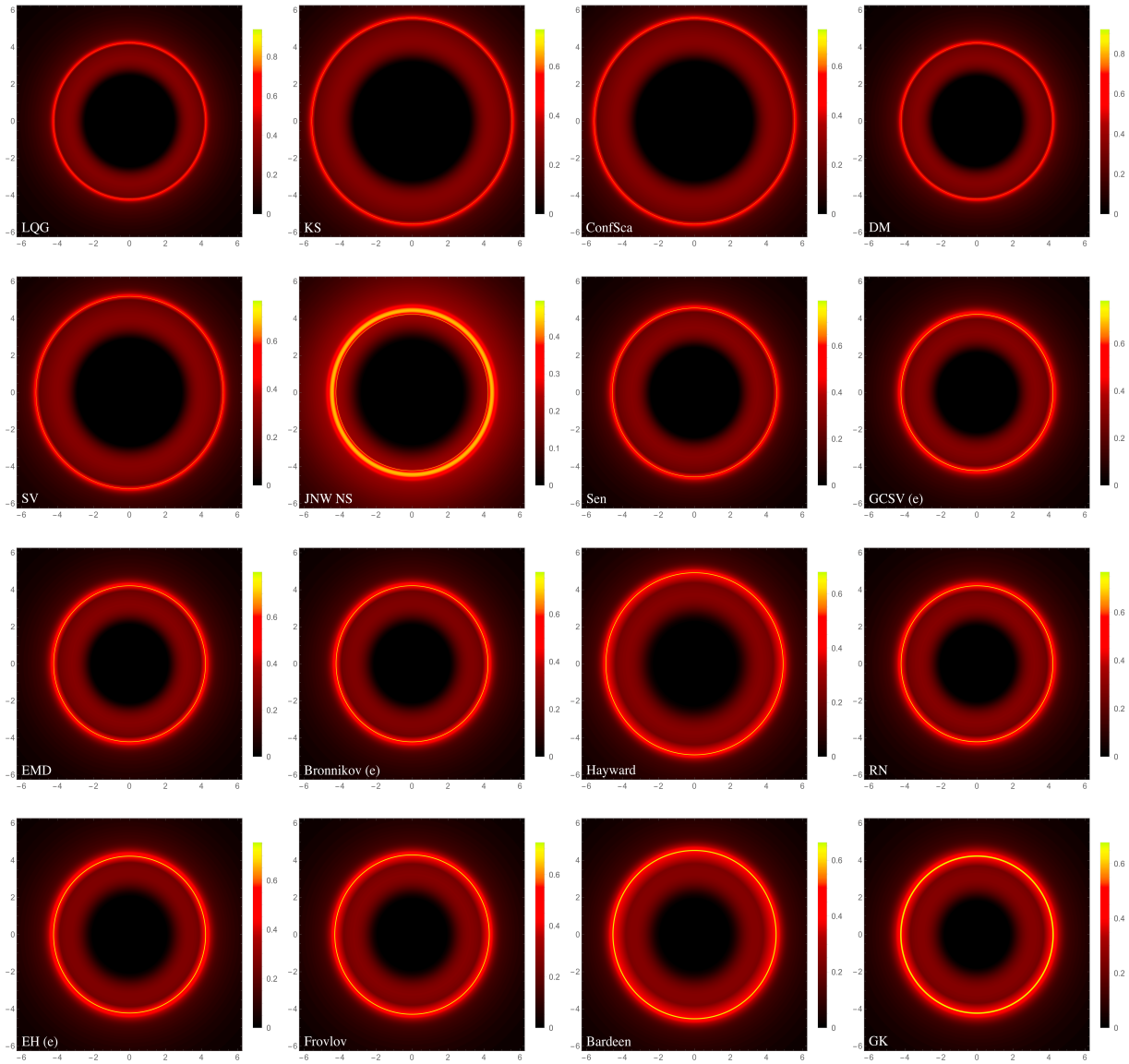

Figure 4.5: Visual appearance, in the impact parameter space, of the sixteen alternative spherically symmetric space-times, under the GLM2 emission profile (3.4), for an observer located at a distance of $r = 1000M$. The images are identified by the space-time abbreviation in the bottom-left corner (see section 3.3 for abbreviations and chosen model parameters) and ordered according to descending values of the theoretical Lyapunov exponent, listed in table 4.1.

three. However, in the GLM1 and GLM2 cases, the observed quantities are much more closely tracked by the Lyapunov index than their counterparts from model GLM3. Focusing on model GLM1 model, the theoretical extinction ratio estimated the observed one with an error $\lesssim 13\%$, excluding the JNW NS space-time (for the reasons mentioned in the previous section). As was already seen in the GLM3 model, the JNW NS is an exceptional case as its appearance stands out from the other geometries'. Not only does the direct emission extend towards larger radii, but the second ring is not stacked on top of the first ring, either in GLM1 or GLM2. Additionally, their relative luminosity also deviates from the trend, with both rings displaying similar, bright yellow features. Nonetheless, disregarding this geometry, the Lyapunov index typically underestimated the observed value. For the model GLM2 model, the theoretical extinction ratio estimated the observed one with an error $\lesssim 4.2\%$, excluding the JNW NS space-time. In this case, the Lyapunov index underestimated the observed extinction ratios for all but the effective geometries, for which it overestimated the observed ratios instead.

The reason why the theoretical prediction of the extinction ratio is closer to the observed ratios from the GLM2 model than GLM1's is likely connected with the shape of each model's emission profile. Comparing the two models as depicted in image 3.1, it is noticeable that their radial intensity profile becomes quite different as we approach the event horizon. Near this region, the GLM1 model has a steeper emission character, whereas the GLM2 model is flatter overall at $r > 1$ (i.e. the emitted intensity is more similar at these radii). Thus, the photons from the $n = 1$ and $n = 2$ rings traverse regions with more similar properties in the GLM2 scenario, which is better aligned with the theoretical assumptions on the Lyapunov exponent. Nonetheless, when the emission extends all the way to the horizon, the deviation between the observed extinction ratios is significantly smaller than for an emission profile that is truncated at the ISCO. But, regardless of the choice of emission profile, the Lyapunov exponent tracks the observed extinction ratios sufficiently well, even when presenting an estimation error. Overall, these results attest the usefulness of the theoretical Lyapunov exponent in discriminating between different geometries. In this sense, it is not a bad guidance in the actual (observable) extinction ratio of the photon ring.

Likewise, the images of Figures 4.4 and 4.5 also follow the patterns discussed for the GLM3 model, concerning the differences in location and width of the $n = 1$ and $n = 2$ rings. In this regard, it is possible to observe that the width of the rings grows larger as the Lyapunov index decreases, which indicates that the impact parameter space for $n = 1$ and $n = 2$ becomes increasingly larger. Once again, this behaviour is congruent with what equation (2.61) is telling. If the Lyapunov index is high, then the scale of instability of the bound orbits is also higher and a small perturbation would grow faster. Alternatively, a small perturbation would grow more slowly if the Lyapunov index had a low value. Because the impact parameter values for $n = 1$, and even more so for $n = 2$, are very susceptible to small deviations from the critical value b_c, the geometries with a high Lyapunov exponent would therefore be more sensitive to small deviations (i.e. have a smaller impact parameter space for these rings) and the opposite would be true for geometries with a low Lyapunov exponent. Note that the ring separation is obviously not discussed, as the emission of different rings is stacked on top of each other.

Furthermore, these images provide an excellent view of the CBD and allow its comparison with the concept of black hole shadow. Like the GLM1 and GLM2 images of the Schwarzschild BH, the size of the CBD is smaller than the inferred EHT shadow's size in all space-times presented here. This result is congruent with others in the literature, where the surrounding accretion disk is geometrically thick (or thin), but not fully spherical [71]. Instead, the size of the CBD is coincident with the "inner shadow", which is tied to the lensed appearance of the event horizon [89]. Regardless, they illustrate an important point: images with similar shadow sizes can still have drastically distinct visual appearances, contained within the features of the $n = 1$ and $n = 2$ rings. Even in the cases when the shadow's boundary is assumed to be degenerate between different geometries, their corresponding first and second rings can be potentially used to unveil the background space-time geometry (in a thin-disk context), making them attractive targets for future VLBI observations. In other words, they provide an additional test to the Kerr (Schwarzschild) hypothesis.

Chapter 5

Conclusion

In the present thesis, we have analysed the role of photon rings as tests for spherically symmetric geometries when surrounded by thin accretion disks, by generating images of a select pool of geometries extracted from the work of Vea [81] and studying the features of the first and second photon rings, and their connection with Lyapunov exponents of unstable bound orbits. We began our efforts by refining the constraints derived in Vea to the parameter space of each alternative geometry. This was achieved via the shadow radius of Sgr A* that was inferred by the EHT collaboration (in [80]). Such a quantity was obtained by appealing to the correlation between the measured diameter of the bright emission ring and the predicted diameter of Sgr A*'s shadow, adjusted by a calibration factor to account for various observational and theoretical biases. We then utilized these constraints to generate the images of 16 alternative geometries when surrounded by a geometrically and optically thin accretion disk. The properties of the disk were simulated using the GLM semi-analytical emission profiles. Finally, we sought to identify any correlation between the computed Lyapunov exponents of nearly-bound orbits and the observed extinction rates between the $n = 1$ and $n = 2$ subrings.

Our results demonstrate that, when the shadow radius bounds are saturated, the selected geometries present significant differences in their compactness and in the radius of their photon sphere. In particular, they deviate significantly in the observed extinction rates between their $n = 1$ and $n = 2$ rings. The latter can be observed in the visual appearances of the photon rings within each GLM emission profile, both when separated from the direct $n = 0$ emission (GLM3) and when stacked over it (GLM1 and GLM2). Furthermore, the observed extinction rates exhibit a strong correlation with the theoretical prediction by the Lyapunov exponent, having an estimation error $\lesssim 4.2\%$ in the GLM2 model and $\lesssim 13\%$ the GLM1 model. Despite the small deviations, such a behaviour suggests that under a fixed emission profile it may be feasible to discriminate between these alternative geometries, based the optical appearance of their photon ring. Most notably, when the shadow is degenerate between different geometries, the brightness features of the photon ring provide a probe of the underlying space-time geometry.

We emphasize that such claims remain valid within the domain of the conditions considered in our work. In this sense, there are several limitations that merit further discussion, in addition to the previously discussed caveats concerning Sgr A*'s shadow inference, pertaining the accretion disk modelling and the considered geometries. Starting with the weakest thread in our work, the accretion disk modelling is subject to several assumptions upon its geometrical, optical and emission properties. With regards to the geometry, we consider an infinitesimally thin accretion disks. This is in direct contrast with the assumptions on the shadow inference which admit a geometrically thick accretion structure around Sgr A*. Our assumption of a geometrically thin geometry is motivated by its ability to reproduce the stacked photon ring signatures, which are also found in thick disk geometries. While such signatures

are favoured by time-averaged GRMHD simulations of the geometrically thick accretion surrounding M87* [71], and the semi-analytic GLM models find excellent agreement with them as well [82], the infinitesimally thin disk geometry is still a non-physical scenario, as accretion disks are expected to have non-negligible thickness. Geometrical thickness adds another complexity layer which, depending on the matter distribution of the disk, may cause the extinction ratios between the $n = 1$ and the $n = 2$ rings to be altered in a significant way. Other potential considerations for disk geometries could include, for example, the study of jet-based emission structures arising in simulations of magnetohydrodynamic accretion environments [229, 230].

Our analysis also explicitly assumes the emission is axisymmetrical. The recent detection of hot flares orbiting near Sgr A* suggest the presence of strong inhomogeneities in the accretion flow [231–233]. Such features can contribute with increased flux variability and alter the accretion disk emission profiles which, depending on the variability time-scale (i.e. close to the time-scale of a photon orbit), can significantly alter the extinction ratios between the first and second rings. We note that the GLM models fit a large range of simulated time-averaged observational appearances of M87* [82], where the differences due to disk variability are smoothed out by averaging out observations over a sufficiently long period of time. This is a greater challenge for Sgr A*, as the observational efforts are expected to be significantly affected by scattering processes occurring in the ionized interstellar medium [234]. We also assume that disk emission is optically thin, in the accretion disk's frame (i.e. the emitter's frame). In reality, accretion disks possess complex emission profiles that span the electromagnetic spectrum, that are not expected to be optically thin at all frequencies. Moreover, the EHT collaboration operates at a constant 230 GHz frequency (i.e. in the observer's frame) [80], representing the opposite scenario we consider here. At such an observation frequency, opacity tends to suppress the interferometric signal of the $n = 2$ rings, though the latter signal is expected to reappear at higher frequencies, such as the planned 345 GHz of future upgrades of VLBI [71, 235]. Another caveat pertains the GLM models in particular, as these are analytical approximations to GRMHD simulations which assume a Kerr geometry. There is no reason to expect that such approximations would fit equally well any non-Kerr alternatives with the exact same intensity profile, as the astrophysical properties of the accretion disk are entangled with those of the background geometry. Not only can the relevant geometrical features for the generation of images (e.g. horizon, photon sphere radius) vary significantly between geometries, but their internal parameters may act upon the disks [236–240], such that no geometry is expected to have the exact same intensity profile. These difficulties could be circumvented by studying the extinction ratio between higher order rings, as the $n = 1$ ring is still quite sensitive to the astrophysical properties of the accretion disk. However, given that even the $n = 3$ ring is expected to be observable (at minimum) with space-based interferometry at the L2 point [70], such an effort remains far out of our current technological reach. Alternatively, one could rely on universal polarization patterns encoded within the photon ring [241] or by monitoring photon ring auto-correlations (i.e. the two-point correlation function of intensity fluctuations on the photon ring) over sufficiently long time-scales [178, 242, 243].

The inclusion of rotation and inclination are another important aspect to consider as it is expected to moderately modify the extinction rate numbers. For spinning space-time geometries, the axial symmetry causes the photon sphere region to generalize to a photon shell of variably thickness [48] where the unstable orbits become spherical (i.e. no longer confined to a plane passing through the center of the space-time) [137]. This contributes with two more quantities towards the characterization of the photon ring, accounting for the rotation and time-delay of the demagnified images of the disk [48], which have a non-negligible impact in the theoretical luminosity. As for inclination, one should also expect significant deviations in the features of the associated rings, especially the $n = 1$ ring, since the shape of the critical

curve also depends on it [52, 82, 179].

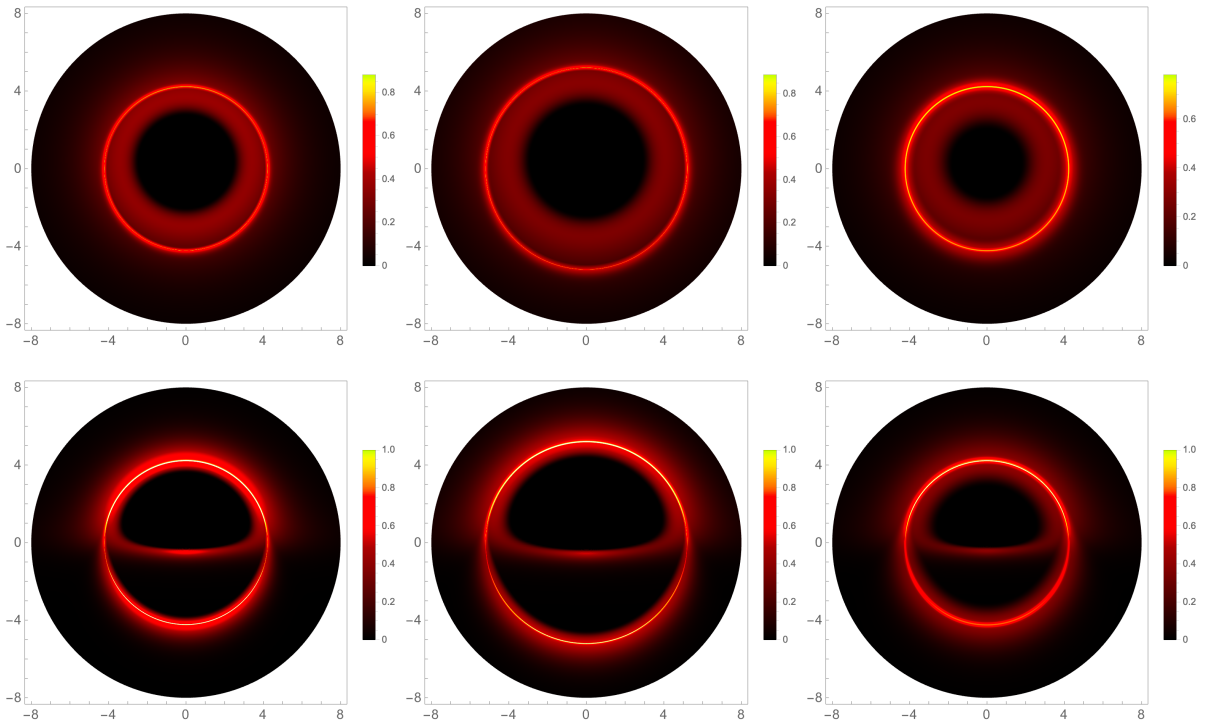

Figure 5.1: Inclined images at 17° (top) and 80° (bottom) degrees of inclination for LQG (left), Schwarzschild (middle) and GK (right) for the GLM2 model.

Figure 5.1 depicts the inclined images of a Schwarzschild black hole and the two alternative black hole geometries on the extreme ends of their Lyapunov index, that we considered in this work, namely, LQG and GK, for the GLM2 emission profile. The top row displays the geometries at the M87* inclination angle $\theta_0 = 17°$, and the bottom row shows their appearance at a nearly edge-on angle of $\theta_0 = 80°$. As one can see from these images, there are apparent visual differences in each model, with respect to the shape and brightness of the photon ring, that are augmented by the inclination angle. Combining rotation together with spin would cause the emission to break the axial symmetry and render the problem of studying the first and second subrings much more complicated than the simplified analysis made here (e.g. the reader is referred to the analysis of [52] on this problem). This problem would be further exacerbated in scenarios with misaligned (tilted) accretion structures, which are consistent with low luminosity active galaxy nuclei [36, 37, 39]. In such scenarios, the misalignment between the accretion disk's and the black hole's respective angular momentum vector would break the axisymmetric nature of the accretion flow, with several consequences in the accretion morphology, emission profiles and flux variability [37, 169].

In conclusion, photon rings are prominent features of black hole images that contain valuable information of the underlying space-time geometry. Here, we have contributed to this effort by comparing the (simulated) observational appearance of multiple alternative spherically symmetric geometries. The research conducted in this work can be further upgraded, either via improvements to the accretion disk modelling, the inclusion of space-time rotation and observer inclination, or both. This is a crucial step if one hopes to disentangle the contribution from the background geometries from the astrophysical phenomena of the accretion disk. Only then, can we harness the full potential of photon rings as reliable probes of the underlying space-time, tests of GR and new gravitational physics [244], and in this way delve deeper into the mysterious nature of black holes.

Bibliography

[1] L. F. D. da Silva, F. S. Lobo, G. J. Olmo, and D. Rubiera-Garcia, "Photon rings as tests for alternative spherically symmetric geometries with thin accretion disks," *Physical Review D*, vol. 108, no. 8, p. 084055, 2023.

[2] E. L. Junior, J. T. S. Junior, F. S. Lobo, M. E. Rodrigues, L. F. D. da Silva, and H. A. Vieira, "Observations on the massive particle surface method," *arXiv preprint arXiv:2401.01821*, 2024.

[3] E. L. Junior, J. T. S. Junior, F. S. Lobo, M. E. Rodrigues, D. Rubiera-Garcia, L. F. D. da Silva, and H. A. Vieira, "Gravitational lensing of a schwarzschild-like black hole in kalb-ramond gravity," *arXiv preprint arXiv:2405.03284*, 2024.

[4] E. L. Junior, J. T. S. Junior, F. S. Lobo, M. E. Rodrigues, D. Rubiera-Garcia, L. F. D. da Silva, and H. A. Vieira, "Spontaneous lorentz symmetry-breaking constraints in kalb-ramond gravity," *arXiv preprint arXiv:2405.03291*, 2024.

[5] V. Frolov and I. Novikov, *Black Hole Physics: Basic Concepts and New Developments*, vol. 96. Springer Science & Business Media, 1998.

[6] P. Schneider, J. Ehlers, and E. Falco, *Gravitational Lenses*. Astronomy and Astrophysics Library, Springer, 1 ed., 1992.

[7] C. Montgomery, W. Orchiston, and I. Whittingham, "Michell, Laplace and the origin of the black hole concept," *Journal of Astronomical History and Heritage*, vol. 12, pp. 90–96, 2009.

[8] K. Thorne, *Black Holes & Time Warps: Einstein's Outrageous Legacy (Commonwealth Fund Book Program)*. WW Norton & Company, 1995.

[9] S. Schaffer, "John Michell and black holes," *Journal for the History of Astronomy, Vol. 10, P. 42, 1979*, vol. 10, p. 42, 1979.

[10] A. Einstein, "Sitzungsberichte der Preussischen Akademie der Wissenschaften zu Berlin 1915," p. 844, 1915.

[11] K. Schwarzschild, "Über das gravitationsfeld eines massenpunktes nach der einsteinschen theorie," *Sitzungsberichte der königlich preussischen Akademie der Wissenschaften*, pp. 189–196, 1916.

[12] S. Chandrasekhar, "The maximum mass of ideal white dwarfs," *Astrophysical Journal, vol. 74, p. 81*, vol. 74, p. 81, 1931.

[13] J. Chadwick, "The existence of a neutron," *Proceedings of the Royal Society of London. Series A, Containing Papers of a Mathematical and Physical Character*, vol. 136, no. 830, pp. 692–708, 1932.

[14] W. Baade and F. Zwicky, "Remarks on super-novae and cosmic rays," *Physical Review*, vol. 46, no. 1, p. 76, 1934.

[15] J. R. Oppenheimer and G. M. Volkoff, "On massive neutron cores," *Physical Review*, vol. 55, no. 4, p. 374, 1939.

[16] J. R. Oppenheimer and H. Snyder, "On continued gravitational contraction," *Physical Review*, vol. 56, no. 5, p. 455, 1939.

[17] R. M. Wald, *General relativity*. University of Chicago press, 2010.

[18] S. W. Hawking and G. F. Ellis, *The large scale structure of space-time*. Cambridge university press, 2023.

[19] D. Hilbert, "Die Grundlagen der Physik.(Zweite Mitteilung)," *Nachrichten von der Gesellschaft der Wissenschaften zu Göttingen, Mathematisch-Physikalische Klasse*, vol. 1917, pp. 53–76, 1917.

[20] Y. Hagihara, "Theory of the relativistic trajectories in a gravitational field of Schwarzschild," *Japanese journal of astronomy and geophysics*, vol. 8, p. 67, 1930.

[21] C. G. Darwin, "The Gravity Field of a Particle," *Proceedings of the Royal Society of London. Series A. Mathematical and Physical Sciences*, vol. 249, no. 1257, pp. 180–194, 1959.

[22] J. Bardeen, "Timelike and null geodesics in the Kerr metric," *Black holes*, vol. 215, 1973.

[23] R. P. Kerr, "Gravitational field of a spinning mass as an example of algebraically special metrics," *Physical review letters*, vol. 11, no. 5, p. 237, 1963.

[24] R. H. Boyer and R. W. Lindquist, "Maximal analytic extension of the Kerr metric," *Journal of mathematical physics*, vol. 8, no. 2, pp. 265–281, 1967.

[25] C. Cunningham and J. Bardeen, "The optical appearance of a star orbiting an extreme Kerr black hole," *Astrophysical Journal, Vol. 183, pp. 237-264 (1973)*, vol. 183, pp. 237–264, 1973.

[26] L. Palmer, M. Pryce, and W. Unruh, "Simulation of starlight lensed by a camera orbiting a Schwarzschild black hole," 1978.

[27] J. Luminet, "Image of a spherical black hole with thin accretion disk," *Astronomy and Astrophysics*, vol. 75, pp. 228–235, 1979.

[28] O. James, E. von Tunzelmann, P. Franklin, and K. S. Thorne, "Gravitational lensing by spinning black holes in astrophysics, and in the movie Interstellar," *Classical and Quantum Gravity*, vol. 32, no. 6, p. 065001, 2015.

[29] J.-P. Luminet, "An illustrated history of black hole imaging: Personal recollections (1972-2002)," *arXiv preprint arXiv:1902.11196*, 2019.

[30] T. Müller and D. Weiskopf, "Revolving around a black hole." (2010, February 24). URL: `https://www.youtube.com/watch?v=9dK8wdNi4QI`.

[31] H. Falcke, F. Melia, and E. Agol, "Viewing the shadow of the black hole at the galactic center," *The Astrophysical Journal*, vol. 528, no. 1, p. L13, 1999.

[32] R. Azulay, A.-K. Baczko, D. Ball, M. Baloković, J. Barrett, D. Bintley, L. Blackburn, W. Boland, K. L. Bouman, G. C. Bower, *et al.*, "First M87 Event Horizon Telescope results. I. The shadow of the supermassive black hole," *The Astrophysical Journal Letters*, vol. 875, no. L1, p. 17, 2019.

[33] K. Akiyama, A. Alberdi, W. Alef, J. C. Algaba, R. Anantua, K. Asada, R. Azulay, U. Bach, A.-K. Baczko, D. Ball, *et al.*, "First Sagittarius A* Event Horizon Telescope results. I. The shadow of the supermassive black hole in the center of the Milky Way," *The Astrophysical Journal Letters*, vol. 930, no. 2, p. L12, 2022.

[34] R. Takahashi, "Shapes and positions of black hole shadows in accretion disks and spin parameters of black holes," *The Astrophysical Journal*, vol. 611, no. 2, p. 996, 2004.

[35] A. E. Broderick and A. Loeb, "Imaging bright-spots in the accretion flow near the black hole horizon of Sgr A," *Monthly Notices of the Royal Astronomical Society*, vol. 363, no. 2, pp. 353–362, 2005.

[36] P. C. Fragile, O. M. Blaes, P. Anninos, and J. D. Salmonson, "Global general relativistic magnetohydrodynamic simulation of a tilted black hole accretion disk," *The Astrophysical Journal*, vol. 668, no. 1, p. 417, 2007.

[37] C. J. White, J. Dexter, O. Blaes, and E. Quataert, "The effects of tilt on the images of black hole accretion flows," *The Astrophysical Journal*, vol. 894, no. 1, p. 14, 2020.

[38] R. Narayan, M. D. Johnson, and C. F. Gammie, "The Shadow of a Spherically Accreting Black Hole," *The Astrophysical Journal Letters*, vol. 885, no. 2, p. L33, 2019.

[39] K. Chatterjee, Z. Younsi, M. Liska, A. Tchekhovskoy, S. B. Markoff, D. Yoon, D. van Eijnatten, C. Hesp, A. Ingram, and M. Van Der Klis, "Observational signatures of disc and jet misalignment in images of accreting black holes," *Monthly Notices of the Royal Astronomical Society*, vol. 499, no. 1, pp. 362–378, 2020.

[40] T. Bronzwaer, J. Davelaar, Z. Younsi, M. Mościbrodzka, H. Olivares, Y. Mizuno, J. Vos, and H. Falcke, "Visibility of black hole shadows in low-luminosity AGN," *Monthly Notices of the Royal Astronomical Society*, vol. 501, no. 4, pp. 4722–4747, 2021.

[41] C.-M. Claudel, K. S. Virbhadra, and G. F. Ellis, "The geometry of photon surfaces," *Journal of Mathematical Physics*, vol. 42, no. 2, pp. 818–838, 2001.

[42] S. V. Iyer and A. O. Petters, "Light's bending angle due to black holes: from the photon sphere to infinity," *General Relativity and Gravitation*, vol. 39, pp. 1563–1582, 2007.

[43] V. Bozza, "Gravitational lensing by black holes," *General Relativity and Gravitation*, vol. 42, pp. 2269–2300, 2010.

[44] V. Perlick, O. Y. Tsupko, and G. S. Bisnovatyi-Kogan, "Influence of a plasma on the shadow of a spherically symmetric black hole," *Physical Review D*, vol. 92, no. 10, p. 104031, 2015.

[45] F. Atamurotov, B. Ahmedov, and A. Abdujabbarov, "Optical properties of black holes in the presence of a plasma: The shadow," *Physical Review D*, vol. 92, no. 8, p. 084005, 2015.

[46] V. Perlick, O. Y. Tsupko, and G. S. Bisnovatyi-Kogan, "Black hole shadow in an expanding universe with a cosmological constant," *Physical Review D*, vol. 97, no. 10, p. 104062, 2018.

[47] S. E. Gralla, D. E. Holz, and R. M. Wald, "Black hole shadows, photon rings, and lensing rings," *Physical Review D*, vol. 100, no. 2, p. 024018, 2019.

[48] S. E. Gralla and A. Lupsasca, "Lensing by Kerr black holes," *Physical Review D*, vol. 101, no. 4, p. 044031, 2020.

[49] V. Cardoso, F. Duque, and A. Foschi, "Light ring and the appearance of matter accreted by black holes," *Physical Review D*, vol. 103, no. 10, p. 104044, 2021.

[50] O. Y. Tsupko, "Shape of higher-order images of equatorial emission rings around a Schwarzschild black hole: Analytical description with polar curves," *Physical Review D*, vol. 106, no. 6, p. 064033, 2022.

[51] M. Wielgus, "Photon rings of spherically symmetric black holes and robust tests of non-Kerr metrics," *Physical Review D*, vol. 104, no. 12, p. 124058, 2021.

[52] H. Paugnat, A. Lupsasca, F. H. Vincent, and M. Wielgus, "Photon ring test of the Kerr hypothesis: Variation in the ring shape," *Astronomy &; Astrophysics*, vol. 668, p. A11, 2022.

[53] G. S. Bisnovatyi-Kogan and O. Y. Tsupko, "Analytical study of higher-order ring images of the accretion disk around a black hole," *Physical Review D*, vol. 105, no. 6, p. 064040, 2022.

[54] A. Abdujabbarov, M. Amir, B. Ahmedov, and S. G. Ghosh, "Shadow of rotating regular black holes," *Physical Review D*, vol. 93, no. 10, p. 104004, 2016.

[55] K.-J. He, S. Guo, S.-C. Tan, and G.-P. Li, "Shadow images and observed luminosity of the Bardeen black hole surrounded by different accretions," *Chinese Physics C*, vol. 46, no. 8, p. 085106, 2022.

[56] J. Peng, M. Guo, and X.-H. Feng, "Influence of quantum correction on black hole shadows, photon rings, and lensing rings," *Chinese Physics C*, vol. 45, no. 8, p. 085103, 2021.

[57] S. Guo, G.-R. Li, and E.-W. Liang, "Influence of accretion flow and magnetic charge on the observed shadows and rings of the Hayward black hole," *Physical Review D*, vol. 105, no. 2, p. 023024, 2022.

[58] G. J. Olmo, J. L. Rosa, D. Rubiera-Garcia, and D. S.-C. Gómez, "Shadows and photon rings of regular black holes and geonic horizonless compact objects," *Classical and Quantum Gravity*, vol. 40, no. 17, p. 174002, 2023.

[59] R. Shaikh and P. S. Joshi, "Can we distinguish black holes from naked singularities by the images of their accretion disks?," *Journal of Cosmology and Astroparticle Physics*, vol. 2019, no. 10, p. 064, 2019.

[60] R. Shaikh, P. Kocherlakota, R. Narayan, and P. S. Joshi, "Shadows of spherically symmetric black holes and naked singularities," *Monthly Notices of the Royal Astronomical Society*, vol. 482, no. 1, pp. 52–64, 2019.

[61] G. Gyulchev, P. Nedkova, T. Vetsov, and S. Yazadjiev, "Image of the Janis-Newman-Winicour naked singularity with a thin accretion disk," *Physical Review D*, vol. 100, no. 2, p. 024055, 2019.

[62] T. Ohgami and N. Sakai, "Wormhole shadows," *Physical Review D*, vol. 91, no. 12, p. 124020, 2015.

[63] M. Guerrero, G. J. Olmo, D. Rubiera-Garcia, and D. S.-C. Gómez, "Shadows and optical appearance of black bounces illuminated by a thin accretion disk," *Journal of Cosmology and Astroparticle Physics*, vol. 2021, no. 08, p. 036, 2021.

[64] M. Guerrero, G. J. Olmo, D. Rubiera-Garcia, and D. S.-C. Gómez, "Light ring images of double photon spheres in black hole and wormhole spacetimes," *Physical Review D*, vol. 105, no. 8, p. 084057, 2022.

[65] J. L. Rosa, P. Garcia, F. H. Vincent, and V. Cardoso, "Observational signatures of hot spots orbiting horizonless objects," *Physical Review D*, vol. 106, no. 4, p. 044031, 2022.

[66] J. L. Rosa and D. Rubiera-Garcia, "Shadows of boson and proca stars with thin accretion disks," *Physical Review D*, vol. 106, no. 8, p. 084004, 2022.

[67] J. L. Rosa, C. F. B. Macedo, and D. Rubiera-Garcia, "Imaging compact boson stars with hot spots and thin accretion disks," , vol. 108, no. 4, p. 044021, 2023.

[68] J. L. Rosa, D. S. Cordeiro, C. F. Macedo, and F. S. Lobo, "Observational imprints of gravastars from accretion disks and hot-spots," *arXiv preprint arXiv:2401.07766*, 2024.

[69] C. A. Herdeiro, A. M. Pombo, E. Radu, P. V. Cunha, and N. Sanchis-Gual, "The imitation game: Proca stars that can mimic the Schwarzschild shadow," *Journal of Cosmology and Astroparticle Physics*, vol. 2021, no. 04, p. 051, 2021.

[70] M. D. Johnson, A. Lupsasca, A. Strominger, G. N. Wong, S. Hadar, D. Kapec, R. Narayan, A. Chael, C. F. Gammie, P. Galison, D. C. M. Palumbo, S. S. Doeleman, L. Blackburn, M. Wielgus, D. W. Pesce, J. R. Farah, and J. M. Moran, "Universal interferometric signatures of a black hole's photon ring," *Science Advances*, vol. 6, no. 12, 2020.

[71] F. Vincent, S. Gralla, A. Lupsasca, and M. Wielgus, "Images and photon ring signatures of thick disks around black holes," *Astronomy & Astrophysics*, vol. 667, p. A170, 2022.

[72] W. Israel, "Event horizons in static vacuum space-times," *Physical review*, vol. 164, no. 5, p. 1776, 1967.

[73] B. Carter, "Axisymmetric black hole has only two degrees of freedom," *Physical Review Letters*, vol. 26, no. 6, p. 331, 1971.

[74] S. W. Hawking, "Black holes in general relativity," *Communications in Mathematical Physics*, vol. 25, pp. 152–166, 1972.

[75] D. C. Robinson, "Uniqueness of the Kerr black hole," *Physical Review Letters*, vol. 34, no. 14, p. 905, 1975.

[76] C. A. Herdeiro and E. Radu, "Asymptotically flat black holes with scalar hair: a review," *International Journal of Modern Physics D*, vol. 24, no. 09, p. 1542014, 2015.

[77] C. A. Herdeiro, "Black holes: on the universality of the Kerr hypothesis," in *Modified and Quantum Gravity: From Theory to Experimental Searches on All Scales*, pp. 315–331, Springer, 2023.

[78] C. Bambi, A. Cárdenas-Avendaño, T. Dauser, J. A. García, and S. Nampalliwar, "Testing the Kerr black hole hypothesis using X-ray reflection spectroscopy," *The Astrophysical Journal*, vol. 842, no. 2, p. 76, 2017.

[79] V. Cardoso and P. Pani, "Testing the nature of dark compact objects: A status report," *Living Reviews in Relativity*, vol. 22, pp. 1–104, 2019.

[80] K. Akiyama, A. Alberdi, W. Alef, J. C. Algaba, R. Anantua, K. Asada, R. Azulay, U. Bach, A.-K. Baczko, D. Ball, *et al.*, "First Sagittarius A* event horizon telescope results. VI. Testing the black hole metric," *The Astrophysical Journal Letters*, vol. 930, no. 2, p. L17, 2022.

[81] S. Vagnozzi, R. Roy, Y. D. Tsai, L. Visinelli, M. Afrin, A. Allahyari, P. Bambhaniya, D. Dey, S. G. Ghosh, P. S. Joshi, *et al.*, "Horizon-scale tests of gravity theories and fundamental physics from the Event Horizon Telescope image of Sagittarius A," *Classical and Quantum Gravity*, vol. 40, no. 16, 2023.

[82] S. E. Gralla, A. Lupsasca, and D. P. Marrone, "The shape of the black hole photon ring: A precise test of strong-field general relativity," *Physical Review D*, vol. 102, no. 12, p. 124004, 2020.

[83] T. Bronzwaer and H. Falcke, "The nature of black hole shadows," *The Astrophysical Journal*, vol. 920, no. 2, p. 155, 2021.

[84] A. E. Broderick, P. Tiede, D. W. Pesce, and R. Gold, "Measuring spin from relative photon-ring sizes," *The Astrophysical Journal*, vol. 927, no. 1, p. 6, 2022.

[85] H. C. L. Junior, L. C. Crispino, P. V. Cunha, and C. A. Herdeiro, "Can different black holes cast the same shadow?," *Physical Review D*, vol. 103, no. 8, p. 084040, 2021.

[86] A. Eichhorn, A. Held, and P.-V. Johannsen, "Universal signatures of singularity-resolving physics in photon rings of black holes and horizonless objects," *Journal of Cosmology and Astroparticle Physics*, vol. 2023, no. 01, p. 043, 2023.

[87] V. Perlick and O. Y. Tsupko, "Calculating black hole shadows: review of analytical studies," *Physics Reports*, vol. 947, pp. 1–39, 2022.

[88] D. Psaltis, "Testing general relativity with the Event Horizon Telescope," *General Relativity and Gravitation*, vol. 51, no. 10, p. 137, 2019.

[89] A. Chael, M. D. Johnson, and A. Lupsasca, "Observing the inner shadow of a black hole: a direct view of the event horizon," *The Astrophysical Journal*, vol. 918, no. 1, p. 6, 2021.

[90] V. Cardoso, A. S. Miranda, E. Berti, H. Witek, and V. T. Zanchin, "Geodesic stability, Lyapunov exponents, and quasinormal modes," *Physical Review D*, vol. 79, no. 6, p. 064016, 2009.

[91] S. Staelens, D. R. Mayerson, F. Bacchini, B. Ripperda, and L. Küchler, "Black hole photon rings beyond general relativity," *Physical Review D*, vol. 107, no. 12, p. 124026, 2023.

[92] S. M. Carroll, *Spacetime and Geometry: An Introduction to General Relativity*. Addison-Wesley, 2004.

[93] C. W. Misner, K. S. Thorn, and J. A. Wheeler, *Gravitation*. Physics Series, W. H. Freeman, 1973.

[94] S. Chandrasekhar, *The mathematical theory of black holes*, vol. 69. Oxford university press, 1998.

[95] E. Poisson and C. M. Will, *Gravity: Newtonian, post-newtonian, relativistic*. Cambridge University Press, 2014.

[96] F. S. Lobo, M. E. Rodrigues, M. V. d. S. Silva, A. Simpson, and M. Visser, "Novel black-bounce spacetimes: Wormholes, regularity, energy conditions, and causal structure," *Physical Review D*, vol. 103, no. 8, 2021.

[97] H. G. Ellis, "Ether flow through a drainhole: A particle model in general relativity," *Journal of Mathematical Physics*, vol. 14, no. 1, pp. 104–118, 1973.

[98] P. Boonserm and M. Visser, "Buchdahl-like transformations for perfect fluid spheres," *International Journal of Modern Physics D*, vol. 17, no. 01, pp. 135–163, 2008.

[99] L. Modesto, "Semiclassical Loop Quantum Black Hole," *International Journal of Theoretical Physics*, vol. 49, no. 8, pp. 1649–1683, 2010.

[100] A. Simpson and M. Visser, "Black-bounce to traversable wormhole," *Journal of Cosmology and Astroparticle Physics*, vol. 2019, no. 02, pp. 042–042, 2019.

[101] H. A. Buchdahl, "General relativistic fluid spheres," *Physical Review*, vol. 116, no. 4, p. 1027, 1959.

[102] H. Buchdahl, "Isotropic coordinates and Schwarzschild metric," *International journal of theoretical physics*, vol. 24, pp. 731–739, 1985.

[103] V. Bozza, "Gravitational lensing in the strong field limit," *Physical Review D*, vol. 66, no. 10, 2002.

[104] M. Born and L. Infeld, "Foundations of the new field theory," *Proceedings of the Royal Society of London. Series A, Containing Papers of a Mathematical and Physical Character*, vol. 144, no. 852, pp. 425–451, 1934.

[105] E. Fradkin and A. A. Tseytlin, "Non-linear electrodynamics from quantized strings," *Physics Letters B*, vol. 163, no. 1-4, pp. 123–130, 1985.

[106] R. Metsaev, M. Rahmanov, and A. A. Tseytlin, "The Born-Infeld action as the effective action in the open superstring theory," *Physics Letters B*, vol. 193, no. 2-3, pp. 207–212, 1987.

[107] A. Dobado, A. Gómez-Nicola, A. L. Maroto, and J. R. Peláez, *Effective lagrangians for the standard model*. Springer Science & Business Media, 2012.

[108] V. De Lorenci, R. Klippert, M. Novello, and J. Salim, "Nonlinear electrodynamics and FRW cosmology," *Physical Review D*, vol. 65, no. 6, p. 063501, 2002.

[109] R. M. Joseph and A. Taflove, "FDTD Maxwell's equations models for nonlinear electrodynamics and optics," *IEEE Transactions on Antennas and Propagation*, vol. 45, no. 3, pp. 364–374, 1997.

[110] S. Kruglov, "Nonlinear electrodynamics with birefringence," *Physics Letters A*, vol. 379, no. 7, pp. 623–625, 2015.

[111] M. Lax and D. Nelson, "Linear and nonlinear electrodynamics in elastic anisotropic dielectrics," *Physical Review B*, vol. 4, no. 10, p. 3694, 1971.

[112] E. Ayón-Beato and A. García, "Regular Black Hole in General Relativity Coupled to Nonlinear Electrodynamics," *Physical Review Letters*, vol. 80, no. 23, p. 5056–5059, 1998.

[113] K. A. Bronnikov, "Regular magnetic black holes and monopoles from nonlinear electrodynamics," *Physical Review D*, vol. 63, no. 4, p. 044005, 2001.

[114] H. Yajima and T. Tamaki, "Black hole solutions in Euler-Heisenberg theory," *Physical Review D*, vol. 63, no. 6, 2001.

[115] A. Burinskii and S. R. Hildebrandt, "New type of regular black holes and particlelike solutions from nonlinear electrodynamics," *Physical Review D*, vol. 65, no. 10, 2002.

[116] Z.-Y. Fan and X. Wang, "Construction of regular black holes in general relativity," *Physical Review D*, vol. 94, no. 12, p. 124027, 2016.

[117] K. Bronnikov, "Nonlinear electrodynamics, regular black holes and wormholes," *International Journal of Modern Physics D*, vol. 27, no. 06, p. 1841005, 2018.

[118] M. E. Rodrigues and M. V. d. S. Silva, "Bardeen regular black hole with an electric source," *Journal of Cosmology and Astroparticle Physics*, vol. 2018, no. 06, p. 025, 2018.

[119] K. A. Bronnikov and R. K. Walia, "Field sources for Simpson-Visser spacetimes," *Physical Review D*, vol. 105, no. 4, 2022.

[120] D. Rasheed, "Non-linear electrodynamics: zeroth and first laws of black hole mechanics," *arXiv preprint hep-th/9702087*, 1997.

[121] S. Gunasekaran, D. Kubizňák, and R. B. Mann, "Extended phase space thermodynamics for charged and rotating black holes and Born-Infeld vacuum polarization," *Journal of High Energy Physics*, vol. 2012, no. 11, 2012.

[122] L. Balart and S. Fernando, "A Smarr formula for charged black holes in nonlinear electrodynamics," *Modern Physics Letters A*, vol. 32, no. 39, p. 1750219, 2017.

[123] Q. Gan, G. Guo, P. Wang, and H. Wu, "Strong cosmic censorship for a scalar field in a Born-Infeld–de Sitter black hole," *Physical Review D*, vol. 100, no. 12, p. 124009, 2019.

[124] P. Wang, H. Wu, and H. Yang, "Scalarized Einstein-Born-Infeld black holes," *Physical Review D*, vol. 103, no. 10, p. 104012, 2021.

[125] M. Novello, V. De Lorenci, J. Salim, and R. Klippert, "Geometrical aspects of light propagation in nonlinear electrodynamics," *Physical Review D*, vol. 61, no. 4, p. 045001, 2000.

[126] V. De Lorenci, R. Klippert, M. Novello, and J. Salim, "Light propagation in non-linear electrodynamics," *Physics Letters B*, vol. 482, no. 1-3, pp. 134–140, 2000.

[127] G. Shore, "'faster than light'photons in gravitational fields—causality, anomalies and horizons," *Nuclear Physics B*, vol. 460, no. 2, pp. 379–394, 1996.

[128] W. Dittrich and H. Gies, "Light propagation in nontrivial QED vacua," *Physical Review D*, vol. 58, no. 2, p. 025004, 1998.

[129] J. Plebański, "Lectures on non-linear electrodynamics," 1970.

[130] B. Zwiebach, *A first course in string theory*. Cambridge university press, 2^{nd} *ed.*, 2009.

[131] D. P. Sorokin, "Introductory Notes on Non-linear Electrodynamics and its Applications," *Fortschritte der Physik*, vol. 70, no. 7–8, 2022.

[132] J. D. Jackson, *Classical electrodynamics*. American Association of Physics Teachers, 1999.

[133] A. Habibina and H. Ramadhan, "Geodesic of nonlinear electrodynamics and stable photon orbits," *Physical Review D*, vol. 101, no. 12, p. 124036, 2020.

[134] M. A. de Paula, H. C. L. Junior, P. V. Cunha, and L. C. Crispino, "Electrically charged regular black holes in nonlinear electrodynamics: Light rings, shadows, and gravitational lensing," *Physical Review D*, vol. 108, no. 8, p. 084029, 2023.

[135] S. Wen, W. Hong, and J. Tao, "Observational appearances of magnetically charged black holes in Born–Infeld electrodynamics," *The European Physical Journal C*, vol. 83, no. 4, p. 277, 2023.

[136] P. V. Cunha and C. A. Herdeiro, "Shadows and strong gravitational lensing: a brief review," *General Relativity and Gravitation*, vol. 50, pp. 1–27, 2018.

[137] E. Teo, "Spherical orbits around a Kerr black hole," *General Relativity and Gravitation*, vol. 53, no. 1, p. 10, 2021.

[138] K. S. Virbhadra and G. F. R. Ellis, "Schwarzschild black hole lensing," *Physical Review D*, vol. 62, no. 8, 2000.

[139] V. Cardoso, L. C. Crispino, C. F. Macedo, H. Okawa, and P. Pani, "Light rings as observational evidence for event horizons: long-lived modes, ergoregions and nonlinear instabilities of ultracompact objects," *Physical Review D*, vol. 90, no. 4, p. 044069, 2014.

[140] G. Khanna and R. H. Price, "Black hole ringing, quasinormal modes, and light rings," *Physical Review D*, vol. 95, no. 8, p. 081501, 2017.

[141] C. S. Reynolds, "Observing black holes spin," *Nature Astronomy*, vol. 3, no. 1, pp. 41–47, 2019.

[142] P. V. Cunha, E. Berti, and C. A. Herdeiro, "Light-ring stability for ultracompact objects," *Physical review letters*, vol. 119, no. 25, p. 251102, 2017.

[143] P. V. Cunha and C. A. Herdeiro, "Stationary black holes and light rings," *Physical Review Letters*, vol. 124, no. 18, p. 181101, 2020.

[144] R. Ghosh and S. Sarkar, "Light rings of stationary spacetimes," *Physical Review D*, vol. 104, no. 4, p. 044019, 2021.

[145] X. Ye and S.-W. Wei, "Distinct topological configurations of equatorial timelike circular orbit for spherically symmetric (hairy) black holes," *Journal of Cosmology and Astroparticle Physics*, vol. 2023, no. 07, p. 049, 2023.

[146] C.-K. Qiao, "Curvatures, photon spheres, and black hole shadows," *Physical Review D*, vol. 106, no. 8, p. 084060, 2022.

[147] M. Cvetič, G. Gibbons, and C. Pope, "Photon spheres and sonic horizons in black holes from supergravity and other theories," *Physical Review D*, vol. 94, no. 10, 2016.

[148] M. Guerrero, G. J. Olmo, D. Rubiera-Garcia, and D. S.-C. Gómez, "Multiring images of thin accretion disk of a regular naked compact object," *Physical Review D*, vol. 106, no. 4, p. 044070, 2022.

[149] Event Horizon Telescope collaboration, "Astronomers Capture First Image of a Black Hole." (2019, April 1). URL: `https://eventhorizontelescope.org/press-release-april-10-2019-astronomers-capture-first-image-black-hole`.

[150] S. E. Gralla, "Can the EHT M87 results be used to test general relativity?," *Physical Review D*, vol. 103, no. 2, p. 024023, 2021.

[151] Merriam-Webster, "Shadow," in *Merriam-Webster.com dictionary*. URL: `https://www.merriam-webster.com/dictionary/shadow`. (Accessed 4 May 2023).

[152] N. Sakai, H. Saida, and T. Tamaki, "Gravastar shadows," *Physical Review D*, vol. 90, no. 10, p. 104013, 2014.

[153] M. Wielgus, J. Horák, F. Vincent, and M. Abramowicz, "Reflection-asymmetric wormholes and their double shadows," *Physical Review D*, vol. 102, no. 8, p. 084044, 2020.

[154] D. Dey, R. Shaikh, and P. S. Joshi, "Perihelion precession and shadows near black holes and naked singularities," *Physical Review D*, vol. 102, no. 4, p. 044042, 2020.

[155] A. B. Joshi, D. Dey, P. S. Joshi, and P. Bambhaniya, "Shadow of a naked singularity without photon sphere," *Physical Review D*, vol. 102, no. 2, p. 024022, 2020.

[156] N. Tsukamoto, "Gravitational lensing in the Simpson-Visser black-bounce spacetime in a strong deflection limit," *Physical Review D*, vol. 103, no. 2, p. 024033, 2021.

[157] S. Chen, J. Jing, W.-L. Qian, and B. Wang, "Black hole images: A Review," *arXiv preprint arXiv:2301.00113*, 2022.

[158] C. Bambi and K. Freese, "Apparent shape of super-spinning black holes," *Physical Review D*, vol. 79, no. 4, p. 043002, 2009.

[159] P. V. Cunha, C. A. Herdeiro, E. Radu, and H. F. Runarsson, "Shadows of Kerr black holes with and without scalar hair," *International Journal of Modern Physics D*, vol. 25, no. 09, p. 1641021, 2016.

[160] M. Wang, S. Chen, and J. Jing, "Shadows of Bonnor black dihole by chaotic lensing," *Physical Review D*, vol. 97, no. 6, p. 064029, 2018.

[161] M. Okyay and A. Övgün, "Nonlinear electrodynamics effects on the black hole shadow, deflection angle, quasinormal modes and greybody factors," *Journal of Cosmology and Astroparticle Physics*, vol. 2022, no. 01, p. 009, 2022.

[162] A. Uniyal, R. C. Pantig, and A. Övgün, "Probing a non-linear electrodynamics black hole with thin accretion disk, shadow, and deflection angle with M87* and Sgr A* from EHT," *Physics of the Dark Universe*, vol. 40, p. 101178, 2023.

[163] J. Synge, "The escape of photons from gravitationally intense stars," *Monthly Notices of the Royal Astronomical Society*, vol. 131, no. 3, pp. 463–466, 1966.

[164] P. J. Young, "Capture of particles from plunge orbits by a black hole," *Physical Review D*, vol. 14, no. 12, p. 3281, 1976.

[165] O. Y. Tsupko, "Analytical calculation of black hole spin using deformation of the shadow," *Physical Review D*, vol. 95, no. 10, p. 104058, 2017.

[166] R. M. Green, *Spherical astronomy*. Cambridge University Press, 1985.

[167] K. Akiyama, A. Alberdi, W. Alef, J. C. Algaba, R. Anantua, K. Asada, R. Azulay, U. Bach, A.-K. Baczko, D. Ball, *et al.*, "First Sagittarius A* Event Horizon Telescope results. II. EHT and multiwavelength observations, data processing, and calibration," *The Astrophysical Journal Letters*, vol. 930, no. 2, p. L13, 2022.

[168] Z. Younsi, D. Psaltis, and F. Özel, "Black Hole Images as Tests of General Relativity: Effects of Spacetime Geometry," *The Astrophysical Journal*, vol. 942, no. 1, p. 47, 2023.

[169] K. Akiyama, A. Alberdi, W. Alef, J. C. Algaba, R. Anantua, K. Asada, R. Azulay, U. Bach, A.-K. Baczko, D. Ball, *et al.*, "First Sagittarius A* Event Horizon Telescope Results. V. Testing Astrophysical Models of the Galactic Center Black Hole," *The Astrophysical Journal Letters*, vol. 930, no. 2, p. L16, 2022.

[170] A. M. Ghez, S. Salim, N. Weinberg, J. Lu, T. Do, J. Dunn, K. Matthews, M. Morris, S. Yelda, E. Becklin, *et al.*, "Measuring distance and properties of the Milky Way's central supermassive black hole with stellar orbits," *The Astrophysical Journal*, vol. 689, no. 2, p. 1044, 2008.

[171] R. Abuter, A. Amorim, M. Bauböck, J. Berger, H. Bonnet, W. Brandner, Y. Clénet, V. C. Du Foresto, P. De Zeeuw, J. Dexter, *et al.*, "A geometric distance measurement to the Galactic center black hole with 0.3% uncertainty," *Astronomy & Astrophysics*, vol. 625, p. L10, 2019.

[172] R. Abuter, N. Aimar, A. Amorim, J. Ball, M. Bauböck, J. Berger, H. Bonnet, G. Bourdarot, W. Brandner, V. Cardoso, *et al.*, "Mass distribution in the Galactic Center based on interferometric astrometry of multiple stellar orbits," *Astronomy & Astrophysics*, vol. 657, p. L12, 2022.

[173] M. Afrin, S. Vagnozzi, and S. G. Ghosh, "Tests of loop quantum gravity from the event horizon telescope results of Sgr A," *The Astrophysical Journal*, vol. 944, no. 2, p. 149, 2023.

[174] R. K. Walia, S. G. Ghosh, and S. D. Maharaj, "Testing rotating regular metrics with EHT results of Sgr A," *The Astrophysical Journal*, vol. 939, no. 2, p. 77, 2022.

[175] F.-G. Xie, R. Narayan, and F. Yuan, "Observational Constraints on Direct Electron Heating in the Hot Accretion Flows in Sgr A* and M87," *The Astrophysical Journal*, vol. 942, no. 1, p. 20, 2022.

[176] F. Yuan, H. Wang, and H. Yang, "The Accretion flow in M87 is really MAD," *The Astrophysical Journal*, vol. 924, no. 2, p. 124, 2022.

[177] R. Emami, R. Anantua, A. A. Chael, and A. Loeb, "Positron Effects on Polarized Images and Spectra from Jet and Accretion Flow Models of M87* and Sgr A*," *The Astrophysical Journal*, vol. 923, no. 2, p. 272, 2021.

[178] S. Hadar, M. D. Johnson, A. Lupsasca, and G. N. Wong, "Photon ring autocorrelations," *Physical Review D*, vol. 103, no. 10, p. 104038, 2021.

[179] A. Cárdenas-Avendaño and A. Lupsasca, "Prediction for the interferometric shape of the first black hole photon ring," *Physical Review D*, vol. 108, no. 6, p. 064043, 2023.

[180] K. Beckwith and C. Done, "Extreme gravitational lensing near rotating black holes," *Monthly Notices of the Royal Astronomical Society*, vol. 359, no. 4, pp. 1217–1228, 2005.

[181] F. Vincent, M. Wielgus, M. Abramowicz, E. Gourgoulhon, J.-P. Lasota, T. Paumard, and G. Perrin, "Geometric modeling of M87* as a Kerr black hole or a non-Kerr compact object," *Astronomy & Astrophysics*, vol. 646, p. A37, 2021.

[182] T. Johannsen, "Photon rings around Kerr and Kerr-like black holes," *The Astrophysical Journal*, vol. 777, no. 2, p. 170, 2013.

[183] G. B. Rybicki and A. P. Lightman, *Radiative processes in astrophysics*. John Wiley & Sons, 2004.

[184] N. Tsukamoto, "Retrolensing by two photon spheres of a black-bounce spacetime," *Physical Review D*, vol. 105, no. 8, p. 084036, 2022.

[185] N. J. Cornish and J. Levin, "Lyapunov timescales and black hole binaries," *Classical and Quantum Gravity*, vol. 20, no. 9, p. 1649, 2003.

[186] S. Hadar, D. Kapec, A. Lupsasca, and A. Strominger, "Holography of the photon ring," *Classical and Quantum Gravity*, vol. 39, no. 21, p. 215001, 2022.

[187] A. Deich, N. Yunes, and C. Gammie, "Lyapunov Exponents to Test General Relativity," *arXiv preprint arXiv:2308.07232*, 2023.

[188] C. F. Macedo, J. L. Rosa, and D. Rubiera-Garcia, "Optical appearance of black holes surrounded by a dark matter halo," *arXiv preprint arXiv:2402.13047*, 2024.

[189] B. Raffaelli, "Hidden conformal symmetry on the black hole photon sphere," *Journal of High Energy Physics*, vol. 2022, no. 3, pp. 1–22, 2022.

[190] C. Bambi, "Can the supermassive objects at the centers of galaxies be traversable wormholes? The first test of strong gravity for mm/sub-mm very long baseline interferometry facilities," *Physical Review D*, vol. 87, no. 10, p. 107501, 2013.

[191] X.-X. Zeng, H.-Q. Zhang, and H. Zhang, "Shadows and photon spheres with spherical accretions in the four-dimensional Gauss-Bonnet black hole," *The European Physical Journal C*, vol. 80, pp. 1–11, 2020.

[192] G. J. Olmo, D. Rubiera-Garcia, and D. S.-C. Gómez, "New light rings from multiple critical curves as observational signatures of black hole mimickers," *Physics Letters B*, vol. 829, p. 137045, 2022.

[193] R. W. Lindquist, "Relativistic transport theory," *Annals of Physics*, vol. 37, no. 3, pp. 487–518, 1966.

[194] C. Bambi, *Black holes: a laboratory for testing strong gravity*, vol. 10. Springer, 2017.

[195] H. Reissner, "Über die eigengravitation des elektrischen feldes nach der einsteinschen theorie," *Annalen der Physik*, vol. 355, no. 9, pp. 106–120, 1916.

[196] G. Nordström, "On the energy of the gravitation field in einstein's theory," *Koninklijke Nederlandse Akademie van Wetenschappen Proceedings Series B Physical Sciences*, vol. 20, pp. 1238–1245, 1918.

[197] M. Heusler, *Black hole uniqueness theorems*. Cambridge lecture notes in physics 6, Cambridge University Press, 1996.

[198] A. Allahyari, M. Khodadi, S. Vagnozzi, and D. F. Mota, "Magnetically Charged black holes from non-linear electrodynamics and the Event Horizon Telescope," *Journal of Cosmology and Astroparticle Physics*, vol. 2020, no. 2, pp. 003–003, 2020.

[199] J. M. Bardeen, "Non-singular general-relativistic gravitational collapse," in *Proceedings, 5th International Conference on Gravitation and the Theory of Relativity, Tbilisi, USSR,*, p. 174, 1968.

[200] S. Ansoldi, "Spherical black holes with regular center: a review of existing models including a recent realization with gaussian sources," 2008.

[201] E. Ayón-Beato and A. Garcıa, "The Bardeen model as a nonlinear magnetic monopole," *Physics Letters B*, vol. 493, no. 1–2, pp. 149–152, 2000.

[202] S. A. Hayward, "Formation and Evaporation of Nonsingular Black Holes," *Physical Review Letters*, vol. 96, no. 3, 2006.

[203] S. I. Kruglov, "Remarks on nonsingular models of Hayward and magnetized black hole with rational nonlinear electrodynamics," *Gravitation and Cosmology*, vol. 27, no. 1, pp. 78–84, 2021.

[204] V. P. Frolov, "Notes on nonsingular models of black holes," *Physical Review D*, vol. 94, no. 10, p. 104056, 2016.

[205] A. Simpson and M. Visser, "Regular Black Holes with Asymptotically Minkowski Cores," *Universe*, vol. 6, no. 1, p. 8, 2019.

[206] R. Kumar and S. G. Ghosh, "Photon ring structure of rotating regular black holes and no-horizon spacetimes," *Classical and Quantum Gravity*, vol. 38, no. 8, p. 085010, 2021.

[207] S. G. Ghosh, "A nonsingular rotating black hole," *The European Physical Journal C*, vol. 75, no. 11, p. 532, 2015.

[208] H. Culetu, "On a Regular Charged black Hole with a Nonlinear Electric Source," *International Journal of Theoretical Physics*, vol. 54, no. 8, pp. 2855–2863, 2015.

[209] S. G. Ghosh and R. K. Walia, "Rotating black holes in general relativity coupled to nonlinear electrodynamics," *Annals of Physics*, vol. 434, p. 168619, 2021.

[210] T. Damour, G. Gibbons, and C. Gundlach, "Dark matter, time-varying G, and a dilaton field," *Physical review letters*, vol. 64, no. 2, p. 123, 1990.

[211] D. Kazakov and S. Solodukhin, "On quantum deformation of the Schwarzschild solution," *Nuclear Physics B*, vol. 429, no. 1, pp. 153–176, 1994.

[212] G. W. Gibbons and K.-i. Maeda, "Black holes and membranes in higher-dimensional theories with dilaton fields," *Nuclear Physics B*, vol. 298, no. 4, pp. 741–775, 1988.

[213] A. Sen, "Rotating charged black hole solution in heterotic string theory," *Physical Review Letters*, vol. 69, no. 7, p. 1006, 1992.

[214] M. Kalb and P. Ramond, "Classical direct interstring action," *Physical Review D*, vol. 9, no. 8, p. 2273, 1974.

[215] A. Tripathi, B. Zhou, A. B. Abdikamalov, D. Ayzenberg, and C. Bambi, "Constraints on Einstein-Maxwell dilaton-axion gravity from X-ray reflection spectroscopy," *Journal of Cosmology and Astroparticle Physics*, vol. 2021, no. 07, p. 002, 2021.

[216] M. S. Morris and K. S. Thorne, "Wormholes in spacetime and their use for interstellar travel: A tool for teaching general relativity," *American Journal of Physics*, vol. 56, no. 5, pp. 395–412, 1988.

[217] S. Riaz, S. Shashank, R. Roy, A. B. Abdikamalov, D. Ayzenberg, C. Bambi, Z. Zhang, and M. Zhou, "Testing regular black holes with X-ray and GW data," *Journal of Cosmology and Astroparticle Physics*, vol. 2022, no. 10, p. 040, 2022.

[218] K. A. Bronnikov and R. K. Walia, "Field sources for Simpson-Visser spacetimes," *Physical Review D*, vol. 105, no. 4, p. 044039, 2022.

[219] E. Bianchi, "The length operator in loop quantum gravity," *Nuclear physics B*, vol. 807, no. 3, pp. 591–624, 2009.

[220] C. Liu, T. Zhu, Q. Wu, K. Jusufi, M. Jamil, M. Azreg-Aïnou, and A. Wang, "Shadow and quasinormal modes of a rotating loop quantum black hole," *Physical Review D*, vol. 101, no. 8, 2020.

[221] M. Astorino, "C metric with a conformally coupled scalar field in a magnetic universe," *Physical Review D*, vol. 88, no. 10, p. 104027, 2013.

[222] A. Chowdhury and N. Banerjee, "Quasinormal modes of a charged spherical black hole with scalar hair for scalar and Dirac perturbations," *The European Physical Journal C*, vol. 78, no. 7, 2018.

[223] M.-H. Li and K.-C. Yang, "Galactic dark matter in the phantom field," *Physical Review D*, vol. 86, no. 12, 2012.

[224] P. Salucci, "The distribution of dark matter in galaxies," *The Astronomy and Astrophysics Review*, vol. 27, pp. 1–60, 2019.

[225] P. R. Brady, I. G. Moss, and R. C. Myers, "Cosmic censorship: as strong as ever," *Physical Review Letters*, vol. 80, no. 16, p. 3432, 1998.

[226] A. I. Janis, E. T. Newman, and J. Winicour, "Reality of the Schwarzschild singularity," *Physical Review Letters*, vol. 20, no. 16, p. 878, 1968.

[227] R. Arnowitt, S. Deser, and C. W. Misner, "Dynamical structure and definition of energy in general relativity," *Physical Review*, vol. 116, no. 5, p. 1322, 1959.

[228] R. Arnowitt, S. Deser, and C. W. Misner, "Republication of: The dynamics of general relativity," *General Relativity and Gravitation*, vol. 40, no. 9, pp. 1997–2027, 2008.

[229] M. Mościbrodzka, H. Falcke, H. Shiokawa, and C. F. Gammie, "Observational appearance of inefficient accretion flows and jets in 3d grmhd simulations: Application to sagittarius a," *Astronomy & Astrophysics*, vol. 570, p. A7, 2014.

[230] M. Mościbrodzka, H. Falcke, and H. Shiokawa, "General relativistic magnetohydrodynamical simulations of the jet in m 87," *Astronomy & Astrophysics*, vol. 586, p. A38, 2016.

[231] R. Abuter, A. Amorim, M. Bauböck, J. Berger, H. Bonnet, W. Brandner, Y. Clénet, V. C. Du Foresto, P. De Zeeuw, C. Deen, *et al.*, "Detection of orbital motions near the last stable circular orbit of the massive black hole sgra," *Astronomy & Astrophysics*, vol. 618, p. L10, 2018.

[232] G. Witzel, G. Martinez, S. Willner, E. Becklin, H. Boyce, T. Do, A. Eckart, G. Fazio, A. Ghez, M. Gurwell, *et al.*, "Rapid variability of sgr a* across the electromagnetic spectrum," *The Astrophysical Journal*, vol. 917, no. 2, p. 73, 2021.

[233] J. M. Michail, M. Wardle, F. Yusef-Zadeh, and D. Kunneriath, "Multiwavelength observations of sgr a*. i. 2019 july 18," *The Astrophysical Journal*, vol. 923, no. 1, p. 54, 2021.

[234] Z. Zhu, M. D. Johnson, and R. Narayan, "Testing general relativity with the black hole shadow size and asymmetry of sagittarius a*: Limitations from interstellar scattering," *The Astrophysical Journal*, vol. 870, no. 1, p. 6, 2018.

[235] P. Tiede, M. D. Johnson, D. W. Pesce, D. C. Palumbo, D. O. Chang, and P. Galison, "Measuring photon rings with the ngeht," *Galaxies*, vol. 10, no. 6, p. 111, 2022.

[236] J. de Freitas Pacheco, "Relativistic accretion into a reissner-nordström black hole revisited," *Journal of Thermodynamics*, vol. 2012, 2012.

[237] D. Pugliese, H. Quevedo, and R. Ruffini, "Motion of charged test particles in reissner-nordström spacetime," *Physical Review D*, vol. 83, no. 10, p. 104052, 2011.

[238] P. S. Joshi, D. Malafarina, and R. Narayan, "Distinguishing black holes from naked singularities through their accretion disc properties," *Classical and Quantum Gravity*, vol. 31, no. 1, p. 015002, 2013.

[239] A. Ditta, G. Mustafa, G. Abbas, F. Atamurotov, and K. Jusufi, "Constraining study of circular orbits and accretion disk around nonlinear electrodynamics black hole," *Journal of Cosmology and Astroparticle Physics*, vol. 2023, no. 08, p. 002, 2023.

[240] Y. Kurmanov, K. Boshkayev, T. Konysbayev, O. Luongo, N. Saiyp, A. Urazalina, G. Ikhsan, and G. Suliyeva, "Accretion disks properties around regular black hole solutions obtained from nonlinear electrodynamics," *arXiv preprint arXiv:2404.15437*, 2024.

[241] E. Himwich, M. D. Johnson, A. Lupsasca, and A. Strominger, "Universal polarimetric signatures of the black hole photon ring," *Physical Review D*, vol. 101, no. 8, p. 084020, 2020.

[242] P. M. Chesler, L. Blackburn, S. S. Doeleman, M. D. Johnson, J. M. Moran, R. Narayan, and M. Wielgus, "Light echos and coherent autocorrelations in a black hole spacetime," *Classical and Quantum Gravity*, vol. 38, no. 12, p. 125006, 2021.

[243] G. N. Wong, "Black hole glimmer signatures of mass, spin, and inclination," *The Astrophysical Journal*, vol. 909, no. 2, p. 217, 2021.

[244] M. D. Johnson, K. Akiyama, L. Blackburn, K. L. Bouman, A. E. Broderick, V. Cardoso, R. P. Fender, C. M. Fromm, P. Galison, J. L. Gómez, *et al.*, "Key science goals for the next-generation Event Horizon Telescope," *Galaxies*, vol. 11, no. 3, p. 61, 2023.